

UC Davis

UC Davis Electronic Theses and Dissertations

Title

Utilization of In-situ Electron Microscopy in Controlling of Oxidation and Reduction Behaviors in Nanoscale Metals and Ceramics

Permalink

<https://escholarship.org/uc/item/58q4h8dk>

Author

Qu, Boyi

Publication Date

2022

Supplemental Material

<https://escholarship.org/uc/item/58q4h8dk#supplemental>

Peer reviewed|Thesis/dissertation

Utilization of In-situ Electron Microscopy in Controlling of Oxidation and Reduction
Behaviors in Nanoscale Metals and Ceramics

By

BOYI QU
DISSERTATION

Submitted in partial satisfaction of the requirements for the degree of

DOCTOR OF PHILOSOPHY

in

Materials Science and Engineering

in the

OFFICE OF GRADUATE STUDIES

of the

UNIVERSITY OF CALIFORNIA

DAVIS

Approved:

Klaus van Benthem, Chair

Jeremy K. Mason

Douglas L. Medlin

Committee in Charge

2022

*Dedicated to my parents,
who made me who I am today.*

Table of Contents

Acknowledgements	vii
List of Publications	viii
List of Figures and Tables.....	ix
Abstract.....	xiii
Chapter 1: Introduction	1
References:.....	5
Chapter 2: Experimental methods and techniques.....	9
2.1 Sample preparation	9
2.1.1 Nanoparticle dropcasting	9
2.1.2 Other sample preparation methods	9
2.2 Electron microscopy	10
2.2.1 Environmental scanning electron microscopy (ESEM).....	10
2.2.2 Transmission Electron Microscopy (TEM)	13
2.2.3 Scanning transmission electron microscopy (STEM).....	18
2.2.4 Electron Energy loss Spectroscopy (EELS).....	20
2.2.5. Energy Dispersive X-ray Spectroscopy (EDXS)	24
2.3 Image analysis.....	26
2.4 References.....	29
Chapter 3 Stabilization of metal(II)oxides on the nanoscale	32

Impact Statement	32
3.1 Introduction.....	32
3.2 Materials & Methods	34
3.3 Results & Discussion	35
3.4 References.....	44
Chapter 4: In situ anisotropic NiO nanostructure growth at high temperature and under water vapor	47
4.1 Introduction.....	47
4.2 Experimental Details.....	50
4.2.1 Specimen Preparation	50
4.2.2 ESEM heating	52
4.2.3 TEM Characterization.....	54
4.3 Results.....	55
4.3.1 ESEM heating	55
4.3.2 TEM characterization.....	62
4.4 Discussion.....	66
4.5 Conclusions:.....	71
4.6 References:.....	72
Chapter 5: In-situ anisotropic growth of nickel oxide nanostructures through layer-by-layer metal oxidation	76

References:.....	87
Chapter 6 Defect redistribution along grain boundaries in SrTiO₃ by externally applied electric fields	91
6.1 Introduction.....	92
6.2 Experimental Techniques	93
6.3 Results:.....	98
6.4 Discussion:.....	106
6.5 Conclusions:.....	110
6.6 References:.....	111
Chapter 7: Tip guided growth of nickel nanostructure with the application of electric current.....	115
7.1 Introduction.....	115
7.2 Methods	116
7.2.1. Fabrication of nickel micropillars and sample preparation.....	116
7.2.2. Current-activated growth of nickel nanostructures	120
7.3 Results:.....	121
7.3.1 SEM and electrical measurements:	121
7.3.2 Finite element modeling	127
7.4 Discussion.....	130
7.4.1. Dielectric breakdown of nickel oxide layer	130

7.4.2. Sintering of particle agglomerates	131
7.4.2. Tip guided growth mechanism of nickel nanostructure.....	133
7.5. Conclusion	135
7.6 References:.....	136
Chapter 8: Conclusions and future work	138
8.1 Conclusions.....	138
8.1.1 Stabilization of FeO wustite phase at the nanoscale	138
8.1.2 Anisotropic growth of NiO nanostructures at high temperatures	139
8.1.3 Electric field effect on defect redistribution along SrTiO ₃ grain boundaries.....	140
8.1.4 Tip-guided growth of nickel nanostructures with the application of electric current	140
8.2 Future Work.....	141
8.2.1 Controlled anisotropic nickel oxide growth.....	141
8.2.2 In-situ controlled tip-guided growth of nickel nanostructures.....	141
8.2.3 In-situ electric field application during annealing of SrTiO ₃ bicrystals	143
8.3 References.....	143
Appendix: Supplemental materials	144

Acknowledgements

I have been extremely fortunate to have all the people who have supported me through my five-year PhD journey at UC Davis. I am thankful for every one of them.

My advisor, Dr. Klaus van Benthem, who has always been so supportive, understanding and encouraging. I would not have been able to accomplish the work in this dissertation without all the guidance, help and opportunities I have received from him over the past few years of PhD research. I truly appreciate it.

My committee members, Dr. Jeremy Mason and Dr. Douglas Medlin, to whom I'm really grateful for all the guidance and discussions on my research project. Dr. Andrew Thron, who helped me tremendously in electron microscopy and starting graduate school. All my lab-mates, colleagues and collaborators who taught me scientific knowledge, answered my questions, listened to my practice talks, and who I worked together on projects with.

My friends, Christine, Dayane, Mingwei, Bing and Bill, with whom I have been so lucky to experience all the ups and downs in graduate school. For all the hard work in Kemper Hall and great times spent in restaurants, parks, and campgrounds. I'm always inspired by them.

My parents, without whom I would not have been here in the first place. For all their love, support, encouragement, long talks, and life advice. Literally everything.

Finally, my husband, Brian, who has always believed in me and been supportive of my decisions. For always having my back and reminding me of the good things during tough times. For teaching me the programming skills and tricks that eventually made my data collection possible and saved me who knows how long in processing the hundreds of images I acquired.

List of Publications

- Qu B, Bonifacio CS, Majidi H, van Benthem K. Stabilization of metal(II)oxides on the nanoscale. *Materials Research Letters*. 2020;8(1):41–47.
<https://doi.org/10.1080/21663831.2019.1684395>
- Qu B, van Benthem K. In situ anisotropic NiO nanostructure growth at high temperature and under water vapor. *Journal of the American Ceramic Society*. 2022;105(4):2454–2464. <https://doi.org/10.1111/jace.18260>
- Qu B, van Benthem K. In-situ anisotropic growth of nickel oxide nanostructures through layer-by-layer metal oxidation. *Scripta Materialia*. 2022;214:114660.
<https://doi.org/10.1016/j.scriptamat.2022.114660>

List of Figures and Tables

Figure 1.1 Experimental setup of current activated Ni nanostructure growth.....	3
Figure 2.1 ESEM chamber view with and without heat shield and GSED	11
Figure 2.2 Auxiliary gas inlet and water reservoir on Quattro ESEM.....	12
Figure 2.3 TEM optics under diffraction and imaging mode	14
Figure 2.4 Schematic of aberration corrected STEM	19
Figure 2.5 Energy diagram of a metal atom and density of states	21
Figure 2.6 EELS powerlaw background.....	23
Figure 2.7 PCA scree plot and spectra of O K edge in SrTiO ₃ before and after PCA analysis...	24
Figure 2.8 Interaction volume of the electron beam in SEM.....	26
Figure 2.9 Illustration of nanostructure measurement methods by ImageJ	27
Figure 3.1 Experimental setup of in-situ heating experiments and HAADF images of the iron oxide particles and nanochains	35
Figure 3.2 Background-stripped Fe L _{2,3} edges acquired from isolated particles and individual nanochains after annealing to the indicated temperatures.	36
Figure 3.3 L ₃ /L ₂ white line intensity ratios as a function of temperature for individual nanoparticle and nanochains	38
Figure 3.4 SAED pattern and BF TEM image of γ -Fe ₂ O ₃ nanochains before annealing	39
Figure 3.5 Rotationally average reciprocal lattice spacings extracted from SAED patterns recorded between 25°C and 900°C.....	41
Figure 4.1 Experimental setup for Ni particles on Si substrate and TEM grid.....	51

Figure 4.2 SEM images and EDXS maps of Ni nanoparticles before and after ESEM heating in water vaopr.....	56
Figure 4.3 ESEM images recorded from Ni nanoparticles before and after ESEM heating under different gaseous atmospheres.....	56
Figure 4.4 ESEM images recorded from Ni nanoparticles before and after ESEM heating under different water vapor pressures.....	58
Figure 4.5 Growth rate for nanostructures as a function of water vapor pressure.....	59
Figure 4.6 ESEM images of two different Ni nanoparticles pre-annealed in vacuum before and after ESEM heating in water vapor.....	60
Figure 4.7 EDXS spectra recorded after ESEM heating from Ni particle.....	62
Figure 4.8 HAADF images and SAED pattern of high aspect ratio nanostructures.....	63
Figure 4.9 EDXS spectra of nanorods	64
Figure 4.10 TEM and HRTEM images of Ni particle after 5 min of ESEM heating.....	65
Figure 4.11 Sketches of high aspect ratio NiO growth and particle elongation.	70
Figure 5.1 SEM image of Ni particles after ESEM heating; STEM BF images of nanostructures; EDXS spectra recorded from metal nanoparticles on the nanostructures.....	79
Figure 5.2 HRTEM micrographs stills from in-situ video recorded during heating.....	81
Figure 5.3 HRTEM micrograph stills from in-situ video recorded during heating showing step movement.....	82
Figure 5.4 2D model of NiO nanostructure growth mechanism and 3D representation of the shrinking Ni particle supported by the NiO surface.	83
Figure 6.1 Experimental setup of electric field application to the SrTiO ₃ bicrystal	95
Figure 6.2 SE maps of grain boundary area after annealing at different field strengths	98

Figure 6.3 HAADF-STEM images of grain boundary core structures after annealing at 50 V/mm recorded from close to the positive and the negative electrode.	99
Figure 6.4 HAADF-STEM and BF TEM image of the grain boundary core recorded close to the positive and negative electrode after field annealing at nominally 150 V/mm	100
Figure 6.5 Ti L _{2,3} and O K edges recorded after annealing at 50 V/mm from the grain boundary core and adjacent SrTiO ₃ half crystals close to the negative and the positive electrode.	102
Figure 6.6 Ti L _{2,3} and O K edges recorded near the positive electrode after annealing at 150 V/mm from the grain boundary and adjacent SrTiO ₃ half crystals	103
Figure 6.7 Ti 2p XPS doublet for reference and experiential samples	104
Figure 6.8 Fractional intensities of the Ti(III) and Ti(II) signatures as a function of relative distance recorded after annealing at 50 V/mm and 150 V/mm	105
Figure 6.9 SEM image of the FIB lamella extracted from areas without strong topography contrast near the 150 V/mm negative electrode side	108
Figure 7.1 Current versus time plot for the full duration of the in situ TEM experiment and the obtained Ni nanostructure after growth	115
Figure 7.2 Ni micropillar fabrication process.	118
Figure 7.3 SEM images of the obtained Ni micropillars.	119
Figure 7.4 Schematic of experimental setup and sample.....	120
Figure 7.5 SEM images of the Ni nanoparticle and micropillar configuration before and after nanoindenter contact	122
Figure 7.6 I-V and I-t curves of initial experiments	123
Figure 7.7 Plots of instant measured current versus applied voltage after hard dielectric breakdown took place.	124

Figure 7.8 Plot of measured current versus time over a series of measurements	125
Figure 7.9 Plot of measured current and indenter tip relative position versus time	126
Figure 7.10 SEM images of the Ni nanoparticle and micropillar configuration before nanoindenter contact and after growth experiment.....	127
Figure 7.11 Finite element modeling 3D model and results	129
Figure S1. I HAADF images of iron oxide nanoparticles and nanochains at different temperatures.....	144
Figure S2. SEM micrographs extracted from the video recorded of nanostructure growth process	145
Table 1. Reference data for L_3/L_2 intensity ratios assigned to specific iron oxides. The listed data were obtained with identical methods utilized in this study.	38
Table 2: Annealing conditions for each sample group before in-situ ESEM heating.....	51
Table 3. Results for EDXS quantitative analysis for pre-annealed nickel particles before and after ESEM heating.....	61

Abstract

The redox behaviors of nanoscale metal and ceramic materials are affected by various parameters and are important in determining certain properties of the material. This dissertation reports the controlling of oxidation and reduction behaviors in some example metal and ceramic materials at the nanoscale by varying material dimensions, gaseous environments, surface energy densities and application of electric fields and currents.

It was suggested in previous studies that iron oxide FeO is thermodynamically unstable under 1000 K with dimensions smaller than 100 nm. In this study, in-situ heating experiments to gradually reduce Fe₂O₃ nanoparticles under 50 nm and nanochains were conducted in a transmission electron microscope. Electron energy loss spectroscopy and selected area electron diffraction both confirmed previous predictions and also revealed the stabilization of FeO phase in nanochains above a critical length. It provides direct evidence that metal (II) oxide with dimensions (particle size) below 100 nm can be stabilized by assembling particles in 1D nanochains.

In the case of nickel nanoparticle oxidation, anisotropic growth of nickel oxide nanostructures was observed during in-situ heating of the particles at 800 °C under water vapor atmospheres in an environmental scanning electron microscope. The NiO stoichiometry was confirmed by both energy dispersive X-ray spectroscopy and selected area electron diffraction. Annealing of the nickel particles under different oxygen partial pressures prior to ESEM heating showed that anisotropic NiO growth only takes place at specific locations where local surface energy density is high enough. The results suggested that the oxide growth can be prevented by manipulation of the surface energy by annealing under low oxygen partial pressures.

One directional growth of single crystalline nickel oxide nanostructures during nickel particle oxidation is also reported at 650 °C and 4×10^{-4} Pa oxygen partial pressure in a transmission electron microscope. In-situ high resolution TEM revealed the layer-by-layer growth of nickel oxide at the Ni/NiO interface while the nickel particle was being consumed. Ledge movement and disconnection migration was observed at the interface that resembled a terrace-ledge-kink growth mechanism. The study demonstrates the applicability of TLK crystal growth mechanism at buried reactive heterophase interfaces.

The role of electric current on one directional nickel nanostructure growth in an SEM is also reported in the study. A positive DC bias was applied to a tungsten carbide nanoindenter tip and electric current flow was established by contacting the tip to a nickel particle sitting on a nickel micropillar. Dielectric breakdown of the nickel oxide surface layer was observed prior to nanostructure growth. Nanostructure growth was achieved upon the retraction of the indenter tip. It was demonstrated by both theoretical calculations and finite element modeling that growth was caused by the combination of electromigration and Joule heating.

For ceramic materials, the study reports electric field effects on the (100) twist grain boundary core structure of SrTiO₃ bicrystals. Nominal field strengths of 50 V/mm and 150 V/mm were applied to the bicrystal in the direction that's parallel to the grain boundary during high temperature annealing after the formation of the grain boundary. High angle angular dark field imaging displayed different grain boundary structure near the positive and negative electrode side. Electron energy loss spectroscopy and X-ray photoelectron spectroscopy both showed higher oxygen vacancy concentrations, i.e. more local reduction near the negative electrode side. The defect redistribution is caused by the migration of oxygen vacancies to the negative electrode side driven by the external electric field.

Chapter 1: Introduction

Nanoscale metal and ceramic materials have attracted much attention due to their unique physical and chemical properties. For instance, nanoscale transition metal oxides are excellent candidates for energy storage¹⁻³, photocatalysis⁴⁻⁷ and solar cells^{8,9}. Perovskite oxide ceramic materials, for which strontium titanate (SrTiO_3) serves as a model material, are competitive candidates for photocatalytic and supercapacitor applications¹⁰.

The redox behaviors of nanoscale metals and ceramics are affected by many different parameters such as materials dimensions (particle size, aspect ratio, etc), gaseous environments (e.g., oxygen partial pressure, types of oxidants, etc), local surface energy densities (crystallography), and applied electric fields or electric currents during processing. In many applications and conditions, oxidation and reduction of the nanomaterials may not be desired or even fully understood. It is therefore critical to understand how the aforementioned parameters and conditions control the redox behavior of materials with the ultimate goal of tailoring and maintaining specific materials properties. This dissertation reports different examples of the influence of dimensionality, gaseous environments, applied electric fields and currents on redox behaviors.

The first example is the particle size influence on transition metal oxide phase stability. Nanoparticles have a much higher surface to volume ratio compared to traditional bulk materials, which causes surface thermodynamics to play a dominant role¹¹. With decreasing particle size, the average binding energy per atom increases due to higher number surface atoms with unsatisfied bonds. Phase stability at the nanoscale has been discussed for various materials in the literature¹²⁻¹⁵. Navrotsky and co-workers have predicted that iron oxide FeO wüstite

nanoparticles with size below 100 nm are thermodynamically unstable below 1000 K and that FeO nanoparticles with size below 16 nm are not stable up to the melting point temperature¹⁴. In bulk, this temperature is around 850 K¹⁶. Exploring an avenue to stabilize FeO phase at the nanoscale may enable its application in nano-magnetic and catalyst technologies.

The second example is the role gaseous environments and local surface energy densities play for nickel oxide growth during nickel particle oxidation at high temperatures. Studies of nickel oxidation behavior at the nanoscale have been reported in many aspects, including the oxidation kinetics and activation energy^{17, 18}, formation of NiO-Ni core-shell structures due to Kirkendall effect¹⁹, and oxide nucleation and growth in nickel alloy thin films in different atmospheres²⁰⁻²⁴. However, there have been only a limited number of studies on the anisotropic growth of one-dimensional oxide nanostructures from metal nanoparticles. Anisotropic nickel oxide nanorod growth from nickel and nickel alloy nanoparticles was reported by Koga and coworkers^{25, 26}. The study discovered that nanorod growth takes place under rapid oxidation conditions in O₂ and proposed that growth is maintained by fast oxygen diffusion in nickel particle subsurface area to the Ni/NiO interface. This dissertation provides critical information for a better understanding under what conditions growth can be initiated, and what mechanisms facilitate the growth process. The experimental results inform about how experimental parameters can be adjusted to circumvent undesired nanostructure growth, or successfully accomplish desired growth.

The third example is the partial reduction of grain boundaries in SrTiO₃ due to an applied electric field. Application of an electric field during sintering has been reported to affect the sintering behavior of ceramic materials. During flash sintering of yttrium-stabilized zirconia, electrode effect on microstructure development caused enhanced grain growth near the

cathode²⁷. Electric field induced defect re-distribution of oxygen vacancies was reported for SrTiO₃ by Rheinheimer and coworkers^{28, 29}. Hughes and coworkers have also documented alterations in SrTiO₃ grain boundary core structures due to an applied electric field across the boundary plane^{30, 31}. The formation and re-distribution of oxygen vacancies leads to local reduction of the material. It is expected that a variation of interfacial oxygen vacancy concentration can influence the electric behavior of the material. As a result, understanding how an electric field affects the oxygen vacancy concentration at the interface provides guidance on the parameters chosen for engineering the materials for anticipated performance.

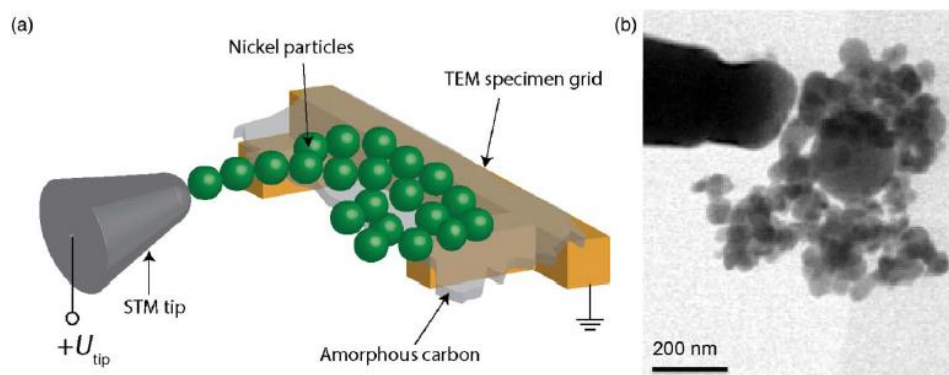


Figure 1.1 (a) Sketch of the experimental setup (b) STEM bright field image of the STM tip in contact with the nickel particle agglomerate. Reproduced from Reference³²

Rufner and coworkers³² reported the growth of one-dimensional nickel nanostructures from nickel particle agglomerates using a tungsten tip with an applied positive bias leading to direct current flow. The experimental setup is displayed in Figure 1.1. Electric current was measured during growth while no external heating was applied. The tungsten tip position remained fixed during the growth process and nanostructure growth effectively pushed the original nickel agglomerate in the opposite direction. Electromigration was proposed to be one

likely growth mechanism. The driving force for mass transport for electromigration is electron wind force, where the electrons bombard onto the metal atoms which move in the direction of electron flow^{33–35}. Joule heating also occurs due to relatively high current densities and causes temperature increase and formation of temperature gradient as a result of the presence of significant heat sinks. However, the experimental evidence documented in the study is limited to clearly identify the growth mechanisms. Additionally, the stationary tip limits control over nanostructure growth. The work presented in this dissertation employs a moving tip with more control of nanostructure growth rate, direction and shape. Finite element modeling was utilized to provide an estimation on the temperature distribution, which aided in the determination of the growth mechanisms.

The outline of the remaining chapters of the dissertation is summarized below. Chapter 2 includes a comprehensive description of the experimental techniques and data processing methods. Chapter 3 focuses on the effect of materials dimension (particle size) on metal oxide phase stability. In-situ heating of Fe₂O₃ nanoparticles was carried out in a reducing environment in a transmission electron microscope and the phase transition during the reduction reaction was identified by both selected area diffraction (SAD) and electron energy loss spectroscopy (EELS). The study confirms that FeO wüstite phase is unstable under 100 nm and reports that stabilization of the phase at the nanoscale can be achieved by assembling nanoparticles into 1D nanochains. Chapter 4 explores how gaseous environments and local surface energy densities affect metal oxide nanostructure growth from metal nanoparticle oxidation. The study reports anisotropic growth of NiO nanostructures from nickel nanoparticles in the presence of water vapor at high temperatures. In-situ environmental scanning electron microscopy (ESEM) imaging, Energy dispersive X-ray spectroscopy (EDXS) and transmission electron microscopy

(TEM) were used in the study. Growth mechanisms are proposed for both particle elongation growth mode and high aspect ratio growth mode. Chapter 5 provides atomic scale experimental evidence and a mechanistic discussion on the layer-by-layer nickel oxide growth through nickel oxidation. Chapter 6 focuses on how an externally applied electric field impacts the grain boundary core structures of 42° (100) twist grain boundary in SrTiO₃. The study reports defect redistribution along the bicrystal grain boundary when an external electric field is applied. Variation in local reduction is reflected by the oxygen vacancy concentration. Chapter 7 reports the tip-guided growth of nickel nanostructure with the application of an electric current. Dielectric breakdown of the nickel oxide film is documented prior to nanostructure growth. The effects of Joule heating and electromigration are discussed. Chapter 8 presents the conclusions of this dissertation and discusses potential future work that can be conducted to continue the studies reported in this dissertation.

References:

1. Tomczyk P, Mordarski G, Obł^okowski J. Kinetics of the oxygen electrode reaction in molten Li + Na carbonate eutectic: Part 5. Linear voltammetric and chronoamperometric data for the reduction processes at NiO monocrystalline electrodes. *J Electroanal Chem.* 1993;353(1):177–193. [https://doi.org/10.1016/0022-0728\(93\)80295-S](https://doi.org/10.1016/0022-0728(93)80295-S)
2. Wu X, Yao S. Flexible electrode materials based on WO₃ nanotube bundles for high performance energy storage devices. *Nano Energy.* 2017;42:143–150. <https://doi.org/10.1016/j.nanoen.2017.10.058>
3. Dhas SD, Maldar PS, Patil MD, *et al.* Synthesis of NiO nanoparticles for supercapacitor application as an efficient electrode material. *Vacuum.* 2020;181:109646. <https://doi.org/10.1016/j.vacuum.2020.109646>
4. Lee K, Lee NH, Shin SH, Lee HG, Kim SJ. Hydrothermal synthesis and photocatalytic characterizations of transition metals doped nano TiO₂ sols. *Mater Sci Eng B.* 2006;129(1):109–115. <https://doi.org/10.1016/j.mseb.2005.12.032>
5. Hu C-C, Teng H. Structural features of p-type semiconducting NiO as a co-catalyst for photocatalytic water splitting. *J Catal.* 2010;272(1):1–8. <https://doi.org/10.1016/j.jcat.2010.03.020>

6. Daghbir R, Drogui P, Robert D. Modified TiO₂ For Environmental Photocatalytic Applications: A Review. *Ind Eng Chem Res.* 2013;52(10):3581–3599. <https://doi.org/10.1021/ie303468t>
7. Shekofteh-Gohari M, Habibi-Yangjeh A, Abitorabi M, Rouhi A. Magnetically separable nanocomposites based on ZnO and their applications in photocatalytic processes: A review. *Crit Rev Environ Sci Technol.* 2018;48(10–12):806–857. <https://doi.org/10.1080/10643389.2018.1487227>
8. Hu L, Peng J, Wang W, *et al.* Sequential Deposition of CH₃NH₃PbI₃ on Planar NiO Film for Efficient Planar Perovskite Solar Cells. *ACS Photonics.* 2014;1(7):547–553. <https://doi.org/10.1021/ph5000067>
9. Chen W, Wu Y, Fan J, *et al.* Understanding the Doping Effect on NiO: Toward High-Performance Inverted Perovskite Solar Cells. *Adv Energy Mater.* 2018;8(19):1703519. <https://doi.org/10.1002/aenm.201703519>
10. Deshmukh VV, Ravikumar CR, Kumar MRA, *et al.* Structure, morphology and electrochemical properties of SrTiO₃ perovskite: Photocatalytic and supercapacitor applications. *Environ Chem Ecotoxicol.* 2021;3:241–248. <https://doi.org/10.1016/j.enceco.2021.07.001>
11. Roduner E. Size matters: why nanomaterials are different. *Chem Soc Rev.* 2006;35(7):583–592. <https://doi.org/10.1039/B502142C>
12. McHale JM, Auroux A, Perrotta AJ, Navrotsky A. Surface Energies and Thermodynamic Phase Stability in Nanocrystalline Aluminas. *Science.* 1997;277(5327):788–791. <https://doi.org/10.1126/science.277.5327.788>
13. Navrotsky A, Mazeina L, Majzlan J. Size-Driven Structural and Thermodynamic Complexity in Iron Oxides. *Science.* 2008;319(5870):1635–1638. <https://doi.org/10.1126/science.1148614>
14. Navrotsky A, Ma C, Lilova K, Birkner N. Nanophase transition metal oxides show large thermodynamically driven shifts in oxidation-reduction equilibria. *Science.* 2010;330(6001):199–201. <https://doi.org/10.1126/science.1195875>
15. Bajaj S, Haverty MG, Arróyave R, Frsc WAGI, Shankar S. Phase stability in nanoscale material systems: extension from bulk phase diagrams. *Nanoscale.* 2015;7(21):9868–9877. <https://doi.org/10.1039/C5NR01535A>
16. Robie RA, Hemingway BS. Thermodynamic properties of minerals and related substances at 298.15 K and 1 bar (10⁵ pascals) pressure and at higher temperatures. U.S. G.P.O. ; For sale by U.S. Geological Survey, Information Services,; 1995 <https://doi.org/10.3133/b2131>
17. Song P, Wen D, X. Guo Z, Korakianitis T. Oxidation investigation of nickel nanoparticles. *Phys Chem Chem Phys.* 2008;10(33):5057–5065. <https://doi.org/10.1039/B800672E>

18. Karmhag R, Tesfamichael T, Wäckelgård E, Niklasson GA, Nygren M. Oxidation Kinetics of Nickel Particles: Comparison Between Free Particles and Particles in an Oxide Matrix. *Sol Energy*. 2000;68(4):329–333. [https://doi.org/10.1016/S0038-092X\(00\)00025-6](https://doi.org/10.1016/S0038-092X(00)00025-6)
19. Railsback JG, Johnston-Peck AC, Wang J, Tracy JB. Size-Dependent Nanoscale Kirkendall Effect During the Oxidation of Nickel Nanoparticles. *ACS Nano*. 2010;4(4):1913–1920. <https://doi.org/10.1021/nn901736y>
20. Unutulmazsoy Y, Merkle R, Fischer D, Mannhart J, Maier J. The oxidation kinetics of thin nickel films between 250 and 500 °C. *Phys Chem Chem Phys*. 2017;19(13):9045–9052. <https://doi.org/10.1039/C7CP00476A>
21. Luo L, Zou L, Schreiber DK, *et al.* In situ atomic scale visualization of surface kinetics driven dynamics of oxide growth on a Ni–Cr surface. *Chem Commun*. 2016;52(16):3300–3303. <https://doi.org/10.1039/C5CC09165A>
22. Wang S, Dong Z, Zhang L, Tsiakaras P, Shen PK, Luo L. Atomic Scale Mechanisms of Multimode Oxide Growth on Nickel–Chromium Alloy: Direct In Situ Observation of the Initial Oxide Nucleation and Growth. *ACS Appl Mater Interfaces*. 2021;13(1):1903–1913. <https://doi.org/10.1021/acsami.0c18158>
23. Luo L, Su M, Yan P, *et al.* Atomic origins of water-vapour-promoted alloy oxidation. *Nat Mater*. 2018;17(6):514–518. <https://doi.org/10.1038/s41563-018-0078-5>
24. Luo L, Li L, Schreiber DK, *et al.* Deciphering atomistic mechanisms of the gas-solid interfacial reaction during alloy oxidation. *Sci Adv*. 2020;6(17):eaay8491. <https://doi.org/10.1126/sciadv.aay8491>
25. Koga K, Hirasawa M. Anisotropic growth of NiO nanorods from Ni nanoparticles by rapid thermal oxidation. *Nanotechnology*. 2013;24(37):375602. <https://doi.org/10.1088/0957-4484/24/37/375602>
26. Koga K, Hirasawa M. Gas-phase generation of noble metal-tipped NiO nanorods by rapid thermal oxidation. *Mater Res Express*. 2014;1(4):045021. <https://doi.org/10.1088/2053-1591/1/4/045021>
27. Qin W, Majidi H, Yun J, van Benthem K. Electrode Effects on Microstructure Formation During FLASH Sintering of Yttrium-Stabilized Zirconia. *J Am Ceram Soc*. 2016;99(7):2253–2259. <https://doi.org/10.1111/jace.14234>
28. Rheinheimer W, Füllung M, Hoffmann MJ. Grain growth in weak electric fields in strontium titanate: Grain growth acceleration by defect redistribution. *J Eur Ceram Soc*. 2016;36(11):2773–2780. <https://doi.org/10.1016/j.jeurceramsoc.2016.04.033>
29. Rheinheimer W, Parras JP, Preusker J-H, De Souza RA, Hoffmann MJ. Grain growth in strontium titanate in electric fields: The impact of space-charge on the grain-boundary mobility. *J Am Ceram Soc*. 2019;102(6):3779–3790. <https://doi.org/10.1111/jace.16217>

30. Hughes LA, Benthem K van. Effects of electrostatic field strength on grain-boundary core structures in SrTiO₃. *J Am Ceram Soc.* 2019;102(8):4502–4510. <https://doi.org/10.1111/jace.16344>
31. Hughes LA, Marple M, van Benthem K. Electrostatic fields control grain boundary structure in SrTiO₃. *Appl Phys Lett.* 2018;113(4):041604. <https://doi.org/10.1063/1.5039646>
32. Rufner JF, Bonifacio CS, Holland TB, Mukherjee AK, Castro RHR, Benthem K van. Local Current-Activated Growth of Individual Nanostructures with High Aspect Ratios. *Mater Res Lett.* 2014;2(1):10–15. <https://doi.org/10.1080/21663831.2013.855272>
33. Ho PS, Kwok T. Electromigration in metals. *Rep Prog Phys.* 1989;52(3):301–348. <https://doi.org/10.1088/0034-4885/52/3/002>
34. Dekker JP, Lodder A. Calculated electromigration wind force in face-centered-cubic and body-centered-cubic metals. *J Appl Phys.* 1998;84(4):1958–1962. <https://doi.org/10.1063/1.368327>
35. Lodder A, Dekker JP. The electromigration force in metallic bulk. *AIP Conf Proc.* 1998;418(1):315–328. <https://doi.org/10.1063/1.54652>

Chapter 2: Experimental methods and techniques

2.1 Sample preparation

In this work, different types of samples are used for different studies including nanoparticles, ceramic bicrystals and metal micropillars. Sample preparation is crucial for electron microscopy characterization as it directly influences the characterization results. Specifically for transmission electron microscopy, sample size needs to be small enough to fit onto a TEM grid that is 3 mm in diameter. Sample thickness needs to achieve electron transparency (under 100 nm) for electrons to transmit through and get desired information.

2.1.1 Nanoparticle dropcasting

Nickel nanoparticles with nominal diameters of 20 nm (US Research Nanomaterials, Inc.) and 300 nm (SkySpring Nanomaterials, Inc.) were used in this work. As-received nanoparticle powder agglomerates were broken apart by a mortar and pestle. Afterwards, small amounts of powder were transferred into a glass vial and isopropanol was added to suspend particles. The suspension was sonicated for approximately 15 – 30 minutes. The nanoparticle suspension was then drop cast onto either a silicon substrate covered with a thermally grown SiO₂ thin film, or onto a high temperature resistant TEM grid made of SiC or Si with SiO₂ film support. Iron oxide nanoparticles follow the same drop casting procedure described for nickel nanoparticles above.

2.1.2 Other sample preparation methods

Nickel micropillars are fabricated by photolithography and utilized for the nanostructure growth experiments. A detailed description of the fabrication process is documented in Chapter 7.

Different from the nanoparticles with diameter smaller than 100 nm that are already electron transparent, bulk samples such as SrTiO₃ bicrystals required sectioning and thinning to produce a small enough sample that can fit onto a TEM specimen holder and has a sample thickness that achieves electron transparency. In this study, SrTiO₃ bicrystal cross section samples were prepared by focused ion beam (FIB) milling using a ThermoFisher Scios dual-beam focused ion beam instrument. The main preparation steps include: (1) section the TEM lamella from the grain boundary area by trench milling using Ga⁺ ion beam; (2) weld the lamella onto a lift-out manipulator; (3) transfer the lamella with the manipulator onto a FIB half grid and weld it in place by electron beam-assisted deposition of tungsten; (4) thin the sample to electron transparency using Ga⁺ with lower beam voltage and current. Once the lamella reached a thickness of roughly 200 nm, additional Ar⁺ ion milling with a Fischione Nanomill was employed to reach a specimen thickness around 50 nm, and to minimize any surface damage caused by Ga⁺ beam irradiation.¹⁻³.

2.2 Electron microscopy

2.2.1 Environmental scanning electron microscopy (ESEM)

Conventional scanning electron microscopes operate at a base pressure of approximately 10⁻⁴-10⁻³ Pa. The relatively high vacuum level makes it challenging to image non-conductive samples due to lack of charge dissipation path and wet samples due to sample drying. Low vacuum imaging provides a solution by supplying gas into the specimen chamber.

Environmental scanning electron microscopy (ESEM) utilizes even higher pressure than low vacuum imaging and the operating base pressure can reach up to 3000 Pa⁴ depending on the gas utilized. The book by Stokes⁴ contains detailed description of the principals of ESEM. Multiple

types of gases can be used for ESEM imaging such as water vapor, nitrogen, carbon dioxide, air etc. Image quality can be degraded due to electron diffuse scattering by the gas molecules. Water vapor is the most commonly used gas for ESEM imaging. In ESEM, higher partial pressure of water vapor in the chamber suppresses water evaporation from the sample thus retaining wet samples closer to its original form during imaging. Figure 2.1 (a) shows the electron signal amplification effect present in ESEM. Danilatos⁵ proposed that the secondary electrons (SE) and backscattered electrons (BSE) interact with the gas molecules present in the chamber and generate more secondary electrons (gaseous SE) from the ionization of the gas molecules. The gas molecules become conductive after ionization, creating a charge dissipation pathway.

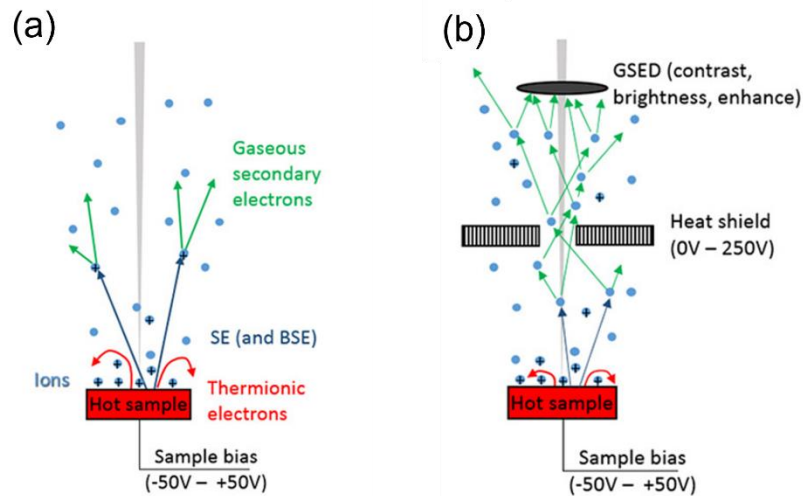


Figure 2.1 ESEM chamber view (a) without heat shield and GSED (b) with heat shield and GSED¹. Green arrows represent the trajectory of GSEs, blue arrows represent the trajectory of BSEs and SEs. Blue spheres represent gas molecules and blue spheres with plus signs represent ionized gas molecules.

¹ Adapted from *Materials Characterization*, **151**, Podor R, Bouala GIN, Ravoux J, Lautru J, Clavier N, Working with the ESEM at high temperature, 15–26, Copyright (2019), with permission from Elsevier.

Though ESEM is not required for imaging nickel nanoparticles, the controlled gaseous atmosphere makes it an excellent tool to investigate nickel particle oxidation behavior under different atmospheres and pressures. In this study, ESEM heating was performed with a ThermoFisher Quattro Environmental Scanning Electron Microscope (ThermoFisher Scientific, Hillsboro, OR). Gas supply to the specimen chamber can come from microscope internal water reservoir for water vapor or outside gas sources connected to the auxiliary gas inlet for other gases, shown in Figure 2.2(a). Water vapor is created by heating up the glass beaker with distilled water, i.e. water reservoir, to 30°C to 40°C (c.f. Figure 2.2(b)). The pressure inside the water glass beaker is kept at a lower level than atmosphere so water vapor can be generated at lower temperatures. Various gases were utilized in this study, including dry N₂, dry air and water vapor. Detailed description of the gas origins can be found in Chapter 4. Purging is enabled for all ESEM heating experiments where the chamber is first pumped to a base pressure about 50-55 Pa followed by flowing in the desired gases to the target pressure of 250 – 400 Pa.

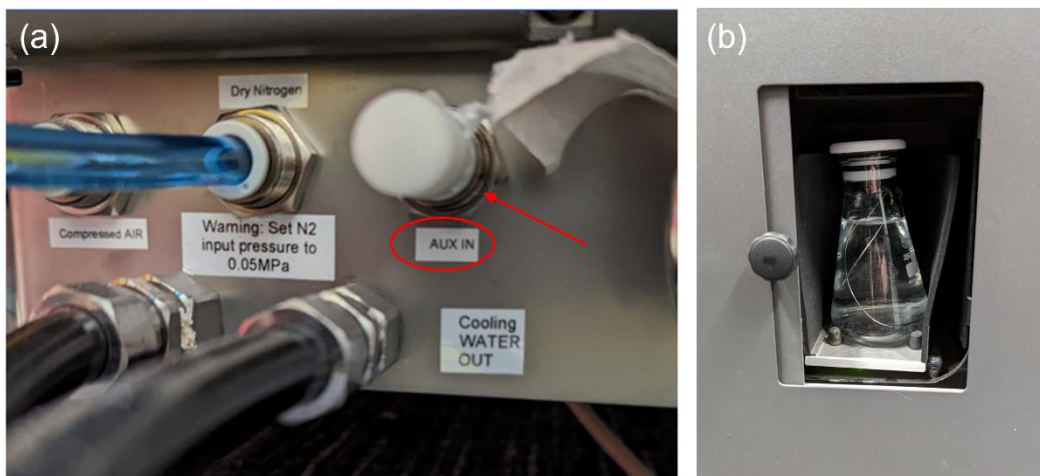


Figure 2.2 (a) Auxiliary gas inlet (b) water reservoir on ThermoFisher Quattro Environmental Scanning Electron Microscope

In this work, ESEM mode is used when a heating stage with temperatures up to 800 °C is in operation. When the heating stage is in operation, a high temperature gaseous secondary electron (GSE) hook detector is installed directly onto the microscope pole piece. The detector consists of a cap containing the cone with aperture and a printed board adaptor with a wire on one end that clips onto the cap. A heat shield is inserted right below the GSE detector. Different biases can be applied to the sample stage and the heat shield to improve signal detection and thus image quality. Figure 2.1 (b) shows a sketch of the instrument with the heat shield and GSE detector inserted. A positive bias up to 220 V can be applied to the heat shield to attract more electrons to the detector. In this work, heat shield biases ranging between 200 V and 220 V were employed. A sample bias from -50 to +50 V can be applied to the sample stage depending on the temperature. A negative bias of around -20 V is first applied to the stage when the temperature is below 500 °C. At this stage, negative stage biasing repels the electrons to the detector direction for more collection. When the temperature reaches 500 °C, stage bias is adjusted to around +10 V. More thermal electron emission takes place at this stage, which contributes increasing noise levels in the detected signals. By applying a small positive bias to the sample stage, only low energy thermal electrons are attracted to the sample stage and reduce their collection by the GSE detector⁶.

2.2.2 Transmission Electron Microscopy (TEM)

Transmission electron microscopy (TEM) and Scanning transmission electron microscopy (STEM) are both utilized in this work for materials characterization. TEM bright field (BF) imaging, selected area electron diffraction (SAED) and high-resolution TEM (HRTEM) are all performed in TEM mode in which the sample is illuminated by a parallel

electron beam. The electrons interact with the sample material as the electron beam transmit through. For an incident beam, the electrons can be scattered elastically without losing any energy or inelastically while losing part of their kinetic energy. For thin samples, elastic scattering is usually coherent and occurs at low angles ($1-10^\circ$). In the case of higher angle elastic scattering ($>10^\circ$), the scattering event becomes increasingly incoherent. Inelastic scattering, on the other hand, is usually incoherent and has much lower scattering angles ($<1^\circ$)⁷.

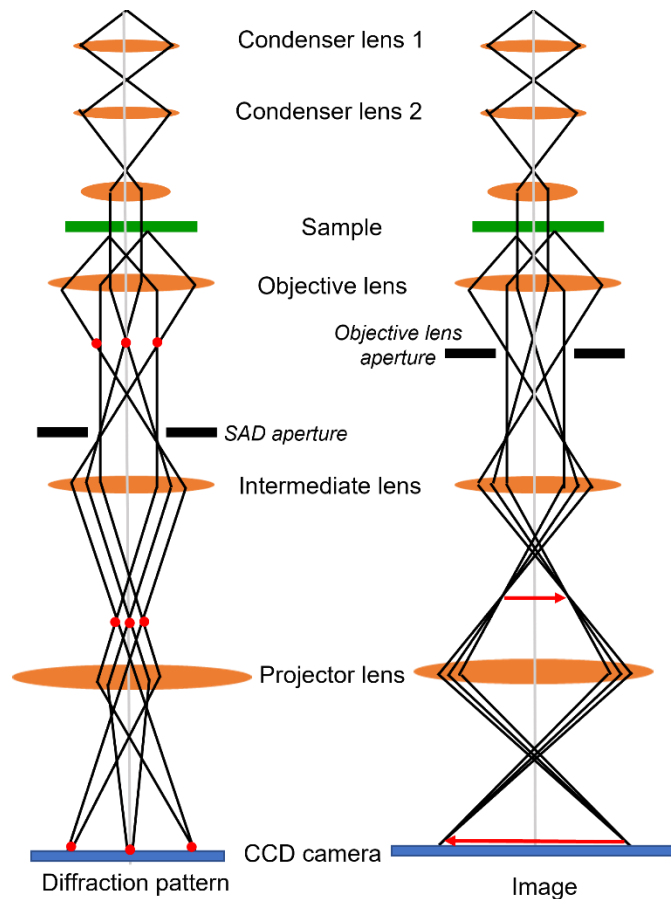


Figure 2.3 Transmission electron microscope optics under diffraction mode (left) and imaging mode (right)

TEM can be operated in two basic modes: imaging mode and diffraction mode, shown in Figure 2.3. BF images are formed by selecting only the direct beam using the objective aperture

on the back focal plane. Image formation is attributed to mass-thickness and diffraction contrast. In this work, bright field imaging is mainly used for observing the shape of the nanoparticles at relatively low magnification. Diffraction patterns are obtained from electrons scattered by the crystallographic planes in the material. The area of interest is selected by the SAD aperture on the image plane. In this work, SAED is used to identify the phase development of nanoparticle oxidation or reduction. Diffraction pattern indexing is an important technique in identifying crystallographic information of the material. Concentric diffraction rings are obtained for polycrystalline and nanoparticle samples. Each individual grain or nanoparticle possesses a different orientation and the diffraction spots from the same family of $\{hkl\}$ plane form a diffraction ring.

For a specific diffraction ring, the ring radius $r_{(hkl)}$ is equal to the distance between any diffraction spot on the ring to the central beam. $r_{(hkl)}^*$ is the corresponding value in reciprocal space. The relationship between the lattice spacing of the $\{hkl\}$ planes $d_{(hkl)}$ and the ring radius is expressed in equation (2.1). λ is the electron beam wave length and L is the camera length.

$$d_{(hkl)} = \frac{\lambda L}{r_{(hkl)}} = \frac{1}{r_{(hkl)}^*} \quad (2.1)$$

By measuring the diffraction ring radius, a d-spacing can be obtained. Ratios of the first few diffraction rings radii gives the inverse ratio of the corresponding lattice plane spacings. The material crystal structure such as face-centered cubic (FCC) or body-centered cubic (BCC) can then be deduced from this ratio. With the diffraction selection rule incorporated for the crystal structure determined, (hkl) values can be assigned to the diffraction rings. Material identification is lastly accomplished by matching the d-spacings to standard values.

HRTEM images are formed by selecting the direct beam and multiple diffracted beams with the objective aperture. Image contrast comes from the interference between the diffracted electron wave and the direct transmitted electron wave. HRTEM is also referred to as phase contrast imaging. The periodic dark and bright fringes in the image appear for destructive and constructive interference, respectively. This technique therefore provides information on lattice plane spacing and crystallographic orientation. However, it is important to note that the fringes observed in an HRTEM image represent wave interference patterns and not direct images of lattice planes. Depending on experimental parameters, including sample thickness and objective lens focus, HRTEM contrast can change.

The resolution of TEM is theoretically dependent on the wavelength of the incident electrons, which is determined by the accelerating voltage of the electron beam. However, due to the imperfections in the optical system, spherical aberration is present⁸. As a consequence, a point in the sample will transform into a disk after going through the lenses, which greatly degrades the theoretical resolution of the TEM.

The following relationship represents the transformation from points in the sample to disks in the image:

$$g(\mathbf{r}) = f(\mathbf{r}) \otimes h(\mathbf{r}-\mathbf{r}') \quad (2.2)$$

$g(\mathbf{r})$ is a function that describes the image and $f(\mathbf{r})$ is the function that describes the sample. $h(\mathbf{r}-\mathbf{r}')$ is a point-spread function that describes how the sample function is transformed by the lens.

After taking the Fourier transforms of the functions the relationship becomes:

$$G(\mathbf{u}) = H(\mathbf{u}) F(\mathbf{u}) \quad (2.3)$$

$G(\mathbf{u})$ is the Fourier transform of $g(\mathbf{r})$, $H(\mathbf{u})$ is the Fourier transform of h , also known as the contrast transfer function (CTF), and $F(\mathbf{u})$ is the Fourier transform of $f(\mathbf{r})$. $H(\mathbf{u})$ can be expressed as the product of the terms $A(\mathbf{u})$, which is the aperture function that is determined by the aperture size, $E(\mathbf{u})$ is the envelope function that describes the attenuation of the electron beam. $B(\mathbf{u})$ is the aberration function that can be expressed by the following equation:

$$B(\mathbf{u}) = \exp(i\chi(\mathbf{u})) \quad (2.4)$$

$\chi(\mathbf{u})$ is the phase function that describes the phase change of the electron wave function due to lens aberrations, and can be expressed as:

$$\chi(\mathbf{u}) = \pi\Delta f\lambda u^2 + \frac{1}{2}\pi C_s\lambda^3 u^4 \text{ (+ chromatic aberration term+ higher order terms)} \quad (2.5)$$

Δf represents the defocus value and C_s represents the spherical aberration coefficient. In a non-corrected system, spherical aberration dominates the resolution limit. When an aberration corrector is used to correct for the spherical aberration, higher order terms become dominate in resolution limit. In STEM imaging, there are no strong lenses after the sample, thus chromatic aberration is not the dominating factor that limits resolution. The JEOL JEM 2100AC STEM is equipped with CEOS hexapole corrector that corrects up to the third order spherical aberration (C_3). The spatial resolution is then limited by the fifth order spherical aberration (C_5). Higher order aberration coefficients can be neglected since the spherical aberration coefficient dominates the resolution limit that can be controlled.

For TEM imaging, Scherzer⁹ reported that balancing the spherical aberration effect against a certain defocus value can optimize the CTF and this defocus value is referred to as “Scherzer defocus”, denoted by Δf_{Sch} :

$$\Delta f_{\text{Sch}} = -1.2(C_s\lambda)^{1/2} \quad (2.6)$$

For the JEOL JEM 2100AC TEM, the information limit is 0.1 nm and point to point resolution at Scherzer defocus is specified to be 0.19 nm. The lattice and point resolution for the Hitachi HF-9500 ETEM are 0.1 nm and 0.18 nm, respectively. At an ideal and well-aligned imaging condition, the spacing between the two objects of interest need to be greater than the resolution limit to be resolved. For this work, HRTEM is used to identify interplanar spacings of the nickel nanoparticles and nanostructures and deduct the material phase and crystallographic orientation. The interplanar spacings for Ni and NiO {222} planes are both greater than 0.1 nm. Therefore, the microscopes utilized in the study are theoretically capable of resolving the first five (hkl) plane interplanar spacings for both Ni and NiO. However, multiple factors such as lens and aperture misalignment, image fluctuation due to heating and imaging vacuum level can all affect the real image resolution obtained.

2.2.3 Scanning transmission electron microscopy (STEM)

In STEM mode, the coherent electron beam is focused to a converged spot and scanned across the area of interest on the sample. The transmitted and scattered electrons are collected by various detectors below the sample, sketched in Figure 2.4.

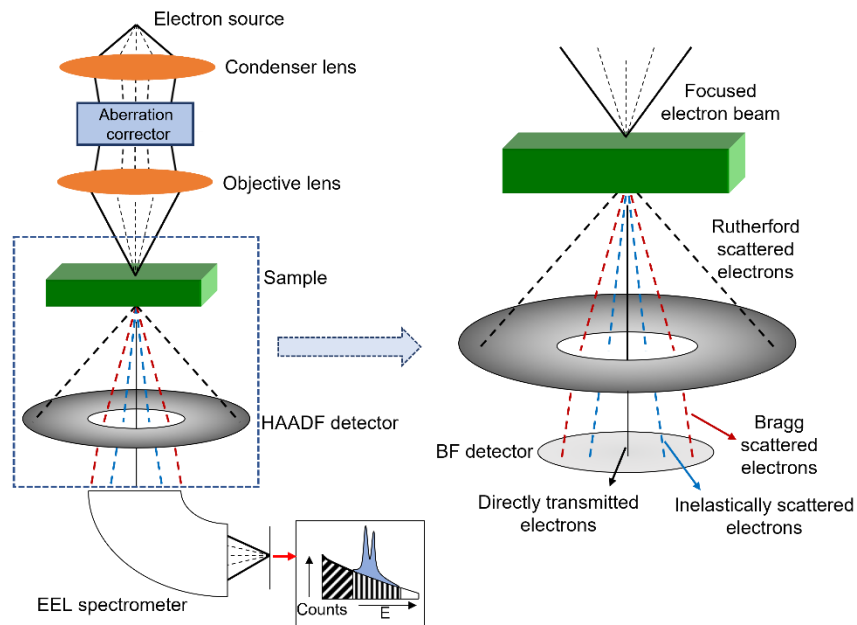


Figure 2.4 Left: Aberration corrected scanning transmission electron microscope optic schematic. A post column electron energy loss spectrometer is present. Right: Enlarged view of the regions enclosed in the box on the left, displaying different types of electrons collected by the HAADF and BF detector

STEM bright field (BF) detector is located on the optical axis and can be reached by the transmitted beam of each scanned spot. It collects direct beam electrons as well as elastically scattered electrons that have very low scattering semi-angles (< 10 mrad). Annular dark field (ADF) detector is a round detector with a hole in the center that surrounds the BF detector. It collects elastically scattered electrons that have scattering semi-angles of 10-50 mrad. High angle annular dark field (HAADF) detector is similar to the ADF but collecting electrons that are scattered at even higher angles (>50 mrad). Rutherford scattering effect is dominant at high scattering angles rather than Bragg scattering¹⁰, thus the scattering event is directly affected by the atomic number (Z). Elements with higher atomic number scatter more electrons to the high angle due to stronger Coulomb interactions between the incident electrons and the nucleus.

Hence more electrons are collected at the detector giving brighter contrast¹¹. HAADF imaging is often referred to as *Z*-contrast imaging.

HAADF imaging is utilized in this work for atomic resolution imaging of the grain boundary area of SrTiO₃. Samples are tilted to <100> or <110> zone axis direction. Lighter elements such as oxygen atoms are difficult to image in *Z*-contrast mode due to insufficient scattering.

Following the theorem of reciprocity, TEM and STEM are electron optically equivalent. And therefore can be described by the same image formation theory⁸.

2.2.4 Electron Energy loss Spectroscopy (EELS)

In STEM mode, incident electrons passing through the sample can be elastically scattered with no energy loss, or inelastically scattered and lose some of their kinetic energy. The change in electron kinetic energy, i.e. energy loss, is denoted as ΔE . Several types of inelastic interactions with materials can cause energy loss at different levels, such as phonon excitations ($\Delta E \sim 0.02$ eV), inter- and intra-band transitions ($\Delta E \sim 2 - 20$ eV), plasmon excitations ($\Delta E \sim 5 - 30$ eV) and inner-shell ionizations ($\Delta E > 50$ eV). Electron energy loss spectroscopy (EELS) is a technique that analyzes the energy distribution of the inelastically scattered electrons and provides information on the materials' electronic structures and local chemical compositions. To collect an EELS spectrum, inelastically scattered electrons are collected post sample and dispersed using a magnetic prism. In the energy-dispersive plane of the spectrometer electrons are spatially separated according to their energy loss. A CCD camera is used to monitor the energy dispersive plane. The resulting electron energy-loss spectrum exhibits electron intensity (I) versus energy loss (ΔE).

The studies in this work focus on the electron energy loss near-edge fine structure (ELNES) in the high energy loss region of the EELS spectrum. Core shell electrons in an atom are ones that are closely bound to the nucleus, such as K, L and M shells. The energy level of these electrons are usually several hundred electron volts (eV) below the Fermi level (E_F) at ground state. When the interaction between the incident electrons and core shell electrons occurs, the core shell electrons are excited to unoccupied states above the Fermi level. The probability of the core shell electrons' excitation to each unoccupied state is determined by the energy distribution of these empty states, i.e. density of states (DOS)¹². Figure 2.5 shows a schematic of both the atomic energy diagram and the DOS of occupied and unoccupied states.

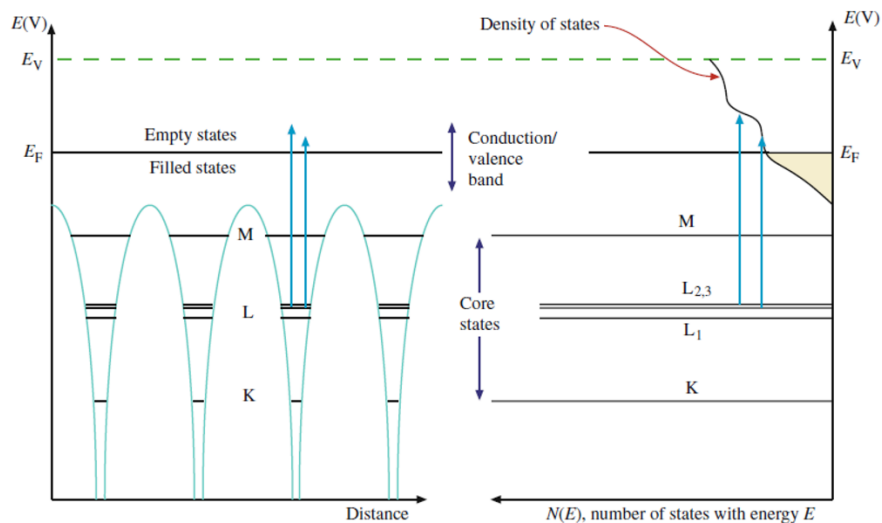


Figure 2.5 Energy diagram of a metal atom (left) and density of states for both occupied (below E_F) and unoccupied (above E_F) states (right). Blue arrows represent the excitation of core shell electrons to the empty states above Fermi level E_F . Reprinted by permission from Springer Nature: Springer, *Fine Structure and Finer Details. In: Transmission Electron Microscopy* by Williams, D.B., Carter, C.B., © 2009 Springer Science+Business Media, LLC.

In the one-electron picture, i.e., the interaction of one electron inside an effective potential, EELS measures the energy-loss function, which is proportional to the double

differential cross-section¹³. Within the Born approximation Bethe has formulated the double differential cross-section as¹⁴:

$$\frac{d^2\sigma}{dEd\Omega} \propto \sum_{i,j} |\langle f | \exp(i\vec{q}\vec{r}) | i \rangle|^2 \delta(E_f - E_i - \Delta E) \quad (2.7)$$

The transition matrix element $\langle f | \exp(i\vec{q}\vec{r}) | i \rangle$ describes the excitation from the initial state (i) to the final state (f), with energies of E_i and E_f , respectively. ΔE represents the energy loss during inelastic scattering. $\sum_{i,j} \delta(E_f - E_i - \Delta E)$ represents the densities of states. Therefore, ELNES shapes in the EELS spectra reflect the site- and symmetry-projected density of unoccupied states, which is affected by the atomic bonding environment.

The ionization edges from the as-acquired EELS spectra contain background signal that originates from plural inelastic scattering events, tails of the preceding ionization edge, valence electron scattering, etc. Though the source of background signal is complex, background can usually be subtracted using a power law fitting model¹⁵:

$$I = A\Delta E^{-r} \quad (2.8)$$

I represents the intensity acquired at specific energy loss ΔE , ΔE is energy loss, and A and r are constants. A fitting window δ is chosen before the edge onset where the power fitting parameters are obtained, shown in Figure 2.6. Then the background intensity is extrapolated and subtracted from the as-acquired edge intensity. In the study reported in Chapter 6, background subtraction of the ionization edges was completed by the power law curve fitting model provided by the DigitalMicrograph software (Gatan Microscopy Suite software). Specifically, the fitting window selected was 420 – 445 eV for Ti L_{2,3} edge and 500 – 525 eV for O K edge.

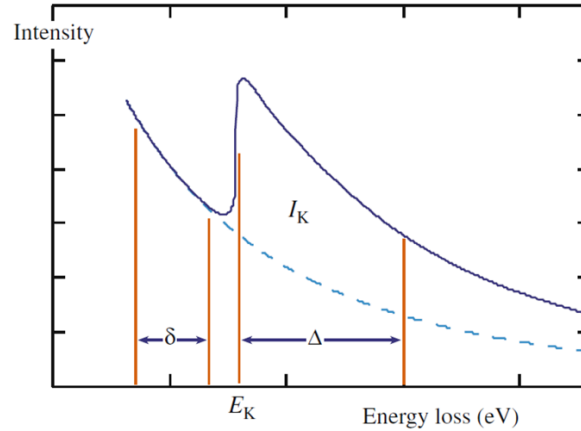


Figure 2.6 Example ionization edge (purple line) and power-law background (blue dashed line). The fitting window is denoted by δ and the extrapolation window is denoted as Δ . Reprinted by permission from Springer Nature: Springer, *High Energy-Loss Spectra and Images*. In: *Transmission Electron Microscopy* by Williams, D.B., Carter, C.B., © 2009 Springer Science+Business Media, LLC

Principal component analysis (PCA) was applied to the EELS spectrum images for noise reduction. Principal component analysis is commonly used in image and spectrum denoising in electron microscopy applications^{17–21}. In this study, denoising with PCA starts with decomposing the dataset matrix \mathbf{D} using the singular value decomposition algorithm (SVD) as $\mathbf{D} = \mathbf{TP}^T$. \mathbf{T} is the score matrix reflecting contributions of the components and \mathbf{P} is the loading matrix that describes the principal components. A PCA scree plot is generated that reflects the significance of each component. Figure 2.7 (a) shows the PCA scree plot of a background subtracted O K edge spectrum image obtained from bulk SrTiO₃. The first 6 components are considered principal components that contain significant information of the dataset as their proportion variances are the highest; the rest of the components are then considered contributions of noise. Denoising of the spectrum image is accomplished by reconstructing the dataset utilizing solely

the principal components obtained from the preceding analysis. Figure 2.7 (b) shows the same O K edge spectrum before and after PCA analysis. Desired denoising result is achieved.

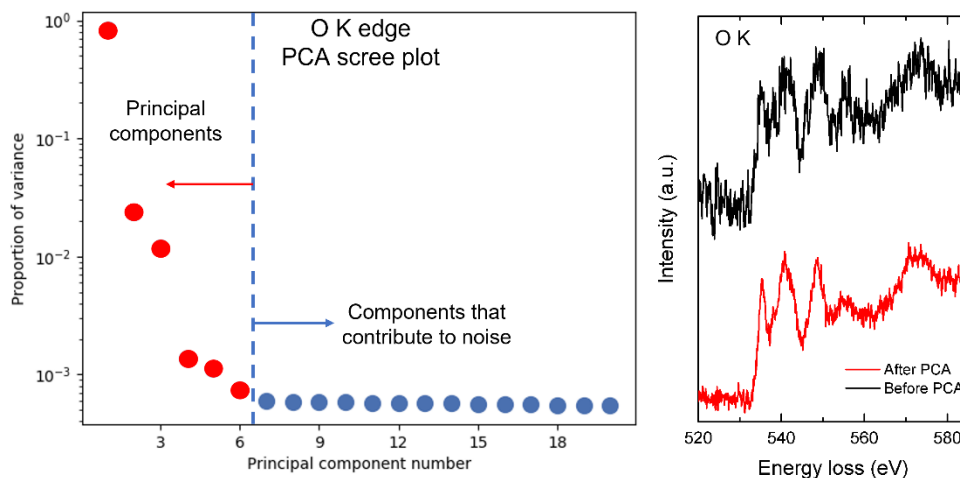


Figure 2.7 (a) PCA scree plot of a background subtracted O K edge spectrum image. Red spheres represent the principal components selected for data reconstruction. Blue spheres represent components that contribute to noise. (b) O K edge spectrum before and after PCA analysis with the six principal components selected in (a)

2.2.5. Energy Dispersive X-ray Spectroscopy (EDXS)

Energy dispersive X-ray spectroscopy is a characterization technique used to analyze the chemical composition of a material. When the electron beam interacts with the sample material, some incident electrons with high enough kinetic energy can excite a core shell electron, for example, K shell, leaving a hole behind. The existence of such holes in the inner shell makes the current state higher-energy and unstable. Electron transitions then take place where an outer shell electron fills hole created in the inner shell, for example from L-shell to K-shell or from M-shell to K-shell. X-ray photons are generated during each transition. Since the energies of the atomic core shells are well-defined for each element, the generated X-ray energies are characteristic for each element and each type of transition. EDXS measures the characteristic X-rays and sample

chemical information can be deduced from the acquired spectrum by identifying the energy positions of each peak.

The interaction volume of the incident electron beam needs to be considered when analyzing an EDXS spectrum. The actual range of production varies with beam accelerating voltage and sample material. For instance, range of Cu K X-ray production for a 15 kV of beam accelerating voltage is approximately $1.7\ \mu\text{m}$ for Si matrix²². In the studies of this work, nanoparticles with nominal diameter of 300 nm are used. The interaction volume of the electron beam exceeds the size of the particle. Hence, the EDXS spectrum acquired must contain X-rays generated underneath the particle of interest, see Figure 2.8. In order to eliminate the X-rays obtained from the background, another scan right next to the particle of interest is obtained with the same acquisition parameters. By subtracting the signal obtained without the particles from the previous scan, background signal can then be separated out. A detailed description can be found in the Methods section of Chapter 4.

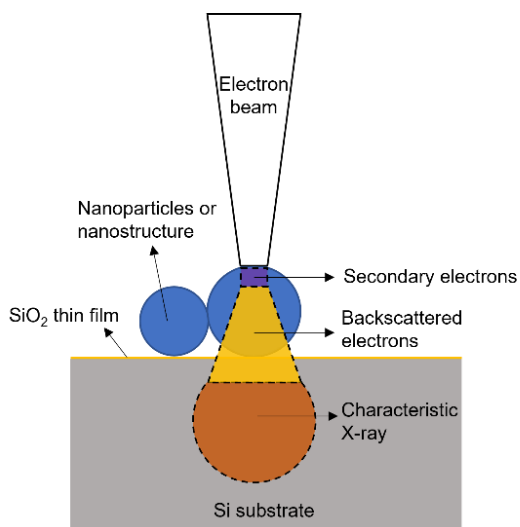


Figure 2.8 Interaction volume of the electron beam when scanning across a nanoparticle of nominal diameter of 300 nm sitting on top of a Si substrate. Colors regions show source regions for different types of signals such as SE, BSE and characteristic X-ray.

2.3 Image analysis

ImageJ software²³ was used to measure growth rates of NiO nanostructures in Chapter 4. Approximately 50 -100 images were extracted from the in-situ videos of each nanostructure growth process for relative length measurements. Measuring each individual image by hand is time-consuming and may introduce inconsistencies for the identification of reference points. Two measurement methods are developed in ImageJ program depending on the growth mode to systematically and efficiently measure the nanostructure length development during growth.

The group of consecutive images obtained from the in-situ video used for measurements were imported as a stack in the ImageJ software. Images were smoothed using the default smoothing filter in ImageJ where it replaces each pixel with the average of its 3 x 3 neighbors. Binary images with minimal noise can then be generated. Further de-speckling of the images was sometimes needed to fill in scattered white pixels on the particles. Figure 2.9 (b) shows an example of the generated binary image and the original ESEM image shown in Figure 2.9 (a). The TurboReg²⁴ plug-in for ImageJ was employed for in-plane alignment of all images in the stack. Two methods are developed depending on the growth mode to systematically measure the nanostructure length development during growth.

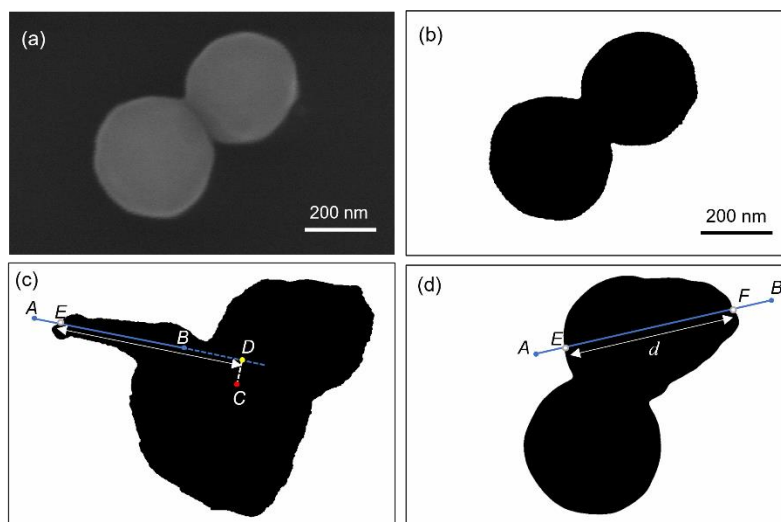


Figure 2.9 (a) ESEM image of nickel nanoparticle (b) Post process image of the same particle shown in (a). (c) Illustration of center of mass measurement method (d) Illustration of particle elongation measurement method

(a) Center of mass

In the high aspect ratio growth mode, nanostructure grows on the particle surface. However, particles usually go through morphology changes over the growth period (e.g., from round particles to a heart shape shown in Figure 2.9 (c)) which makes it challenging to set a consistent reference point for structure length measurement. Therefore, in this method, instead of measuring the nanostructures directly, a defined reference length in the nanostructure growth direction is measured to improve consistency, as shown in Figure 2.9 (c). It applies to particle agglomerates that have significant change in shape but minimal shift in center of mass. Figure 2.9 (c) shows a schematic of the measurement process. A straight line AB (solid blue) is created in nanostructure growth direction, which will be applied to all images in the stack. It is referred to as the growth reference line. The coordinates of the starting and end point, A and B are then

recorded. The rest of the measurement steps are described below. These steps are carried out for each individual image in the stack:

1. Center of mass C (red dot) is measured and its coordinates are recorded.
2. A line perpendicular to the growth reference line and passes through the center of mass is created (white dashed line).
3. The intersection point D (yellow dot) of the growth reference line and the perpendicular is defined as the reference point.
4. Intensity profile of the growth reference line from D to A is plotted. The point where intensity drops from 256 to 0 is the edge of the nanostructure.
5. Distance between the reference point D and the edge of the nanostructure E (gray dot) is then measured.

(b) Particle elongation

In this method, the entire particle length is measured along the elongation direction. It applies to particles that are elongated in one direction, as shown in Figure 2.9 (d). A straight line AB (solid blue) is created in the nanostructure elongation direction, which will be applied to all images in the stack. The rest of the measurement steps are carried out for each individual image and are described as follows:

1. Intensity profile of AB is plotted. The points where intensity increases from 0 to 256 and drops from 256 to 0 are the two edges of the particle.
2. Distance between the two edges (gray dots) is then measured.

2.4 References

1. McCaffrey JP, Phaneuf MW, Madsen LD. Surface damage formation during ion-beam thinning of samples for transmission electron microscopy. *Ultramicroscopy*. 2001;87(3):97–104. [https://doi.org/10.1016/S0304-3991\(00\)00096-6](https://doi.org/10.1016/S0304-3991(00)00096-6)
2. Kato NI. Reducing focused ion beam damage to transmission electron microscopy samples. *Journal of Electron Microscopy*. 2004;53(5):451–458. <https://doi.org/10.1093/jmicro/dfh080>
3. Schaffer M, Schaffer B, Ramasse Q. Sample preparation for atomic-resolution STEM at low voltages by FIB. *Ultramicroscopy*. 2012;114:62–71. <https://doi.org/10.1016/j.ultramic.2012.01.005>
4. Stokes DJ, Chen J, Neijssen WAJ, Baken E, Uncovsky M. High pressure imaging in the environmental scanning electron microscope (ESEM). In: Luysberg M, Tillmann K, Weirich T, eds. *EMC 2008 14th European Microscopy Congress 1–5 September 2008, Aachen, Germany*. Berlin, Heidelberg: Springer; 2008:627–628. https://doi.org/10.1007/978-3-540-85156-1_314
5. Danilatos GD. Introduction to the ESEM instrument. *Microscopy Research and Technique*. 1993;25(5–6):354–361. <https://doi.org/10.1002/jemt.1070250503>
6. Podor R, Bouala GIN, Ravoux J, Lautru J, Clavier N. Working with the ESEM at high temperature. *Materials Characterization*. 2019;151:15–26. <https://doi.org/10.1016/j.matchar.2019.02.036>
7. Williams DB, Carter CB. Scattering and Diffraction. In: Williams DB, Carter CB, eds. *Transmission Electron Microscopy: A Textbook for Materials Science*. Boston, MA: Springer US; 2009:23–38. https://doi.org/10.1007/978-0-387-76501-3_2
8. Scherzer O. Über einige Fehler von Elektronenlinsen. *Z Physik*. 1936;101(9):593–603. <https://doi.org/10.1007/BF01349606>
9. Scherzer O. The Theoretical Resolution Limit of the Electron Microscope. *Journal of Applied Physics*. 1949;20(1):20–29. <https://doi.org/10.1063/1.1698233>
10. Jesson DE, Pennycook SJ. Incoherent imaging of crystals using thermally scattered electrons. *Proceedings of the Royal Society of London Series A: Mathematical and Physical Sciences*. 1995;449(1936):273–293. <https://doi.org/10.1098/rspa.1995.0044>
11. Nellist PD, Pennycook SJ. The principles and interpretation of annular dark-field Z-contrast imaging. In: Hawkes PW, ed. *Advances in Imaging and Electron Physics*. Vol. 113. Elsevier; 2000:147–203. [https://doi.org/10.1016/S1076-5670\(00\)80013-0](https://doi.org/10.1016/S1076-5670(00)80013-0)

12. Williams DB, Carter CB. Fine Structure and Finer Details. In: Williams DB, Carter CB, eds. *Transmission Electron Microscopy: A Textbook for Materials Science*. Boston, MA: Springer US; 2009:741–760. https://doi.org/10.1007/978-0-387-76501-3_40
13. Platzman PM, Wolff PA, Seitz F, Turnbull D, Ehrenreich H. Solid State Physics: Advances in Research and Applications. Waves and interactions in solid state plasmas. Supplement 13. Academic Press; 1973
14. Bethe H. Zur Theorie des Durchgangs schneller Korpuskularstrahlen durch Materie. *Annalen der Physik*. 1930;397(3):325–400. <https://doi.org/10.1002/andp.19303970303>
15. Egerton RF. An Introduction to EELS. In: Egerton RF, ed. *Electron Energy-Loss Spectroscopy in the Electron Microscope*. Boston, MA: Springer US; 2011:1–28. https://doi.org/10.1007/978-1-4419-9583-4_1
16. Williams DB, Carter CB. High Energy-Loss Spectra and Images. In: Williams DB, Carter CB, eds. *Transmission Electron Microscopy: A Textbook for Materials Science*. Boston, MA: Springer US; 2009:715–739. https://doi.org/10.1007/978-0-387-76501-3_39
17. Bacchelli S, Papi S. Image denoising using principal component analysis in the wavelet domain. *Journal of Computational and Applied Mathematics*. 2006;189(1):606–621. <https://doi.org/10.1016/j.cam.2005.04.030>
18. Titchmarsh JM, Dumbill S. Multivariate Statistical Analysis of Feg-Stem Edx Spectra. *Journal of Microscopy*. 1996;184(3):195–207. <https://doi.org/10.1046/j.1365-2818.1996.1400698.x>
19. Anderson IM, Bentley J. Multivariate Statistical Analysis of Spectrum Lines and Images. *Microscopy and Microanalysis*. 1997;3(S2):931–932. <https://doi.org/10.1017/S1431927600011545>
20. Titchmarsh JM. EDX spectrum modelling and multivariate analysis of sub-nanometer segregation. *Micron*. 1999;30(2):159–171. [https://doi.org/10.1016/S0968-4328\(99\)00020-7](https://doi.org/10.1016/S0968-4328(99)00020-7)
21. Parish CM, Brewer LN. Multivariate statistics applications in phase analysis of STEM-EDS spectrum images. *Ultramicroscopy*. 2010;110(2):134–143. <https://doi.org/10.1016/j.ultramic.2009.10.011>
22. Goldstein JI, Newbury DE, Michael JR, Ritchie NWM, Scott JHJ, Joy DC. X-Rays. In: Goldstein JI, Newbury DE, Michael JR, Ritchie NWM, Scott JHJ, Joy DC, eds. *Scanning Electron Microscopy and X-Ray Microanalysis*. New York, NY: Springer; 2018:39–63. https://doi.org/10.1007/978-1-4939-6676-9_4
23. Schneider CA, Rasband WS, Eliceiri KW. NIH Image to ImageJ: 25 years of image analysis. *Nat Methods*. 2012;9(7):671–675. <https://doi.org/10.1038/nmeth.2089>

24. Thevenaz P, Ruttimann UE, Unser M. A pyramid approach to subpixel registration based on intensity. *IEEE Transactions on Image Processing*. 1998;7(1):27–41.
<https://doi.org/10.1109/83.650848>

Chapter 3 Stabilization of metal(II)oxides on the nanoscale¹

Increasing surface-to-volume ratios for nanoscale materials may cause metal(II)oxides phases to be thermodynamically unstable compared to their bulk counterparts. For instance, previous studies have found FeO to be unstable for nanoparticles with dimensions below 100 nm. In this study in-situ TEM was used to gradually reduce nanoparticles and nanochains of Fe₂O₃. Electron energy-loss spectroscopy and selected area diffraction at different temperatures not only confirm earlier predictions, but also reveal the unexpected stabilization of the FeO phase for nanochains with a minimal critical length. Hence, dimensionally constrained phases were stabilized on length-scales that were previously considered unattainable.

Impact Statement

This study provides direct experimental evidence for the previously unanticipated stabilization of metal(II)oxides with dimensions well below 100 nm, which has exciting potential for catalyst technologies and next generation memory devices.

3.1 Introduction

Nanoscale materials have exciting physical properties remarkably different from their bulk counterparts¹, including nanoscale transport processes, modified reduction-oxidation behaviors, and length-scale dependent mechanical strength. Such effects are commonly

¹ Published as B. Qu, C.S. Bonifacio, H. Majidi, K. van Benthem, *Materials Research Letters* **8** (2020) 41–47.

attributed to rapidly increasing surface area to volume ratio with decreasing dimensions, which causes surface thermodynamics to dominate². Higher average binding energy per atom can directly impact oxidation-reduction reactions³, solubility limits⁴, and phase stability⁵⁻⁷. For spinel-type oxide nanocrystals with dimensions around 10 nm, Navrotsky et al. report shifts in redox free energies, oxygen fugacity, and stabilization temperatures when compared to the bulk. From their study the authors generally concluded that smaller surface energies for spinel structures compared to the respective divalent oxides leads to diminished thermodynamic stability⁶.

Iron oxide is ubiquitous in nature, exists in various polymorphs⁸, and finds application as efficient catalyst for fuel-cell reactions⁹, electrode materials for rechargeable solid-state batteries¹⁰, and nanoscale magnets¹¹. In rocks, FeO serves as a redox buffer and coexists with Fe₂O₃ to form magnetite, in which Fe assumes oxidation states of +II and +III. Bulk FeO phase is stable above 560 °C and remains metastable under ambient conditions in the multiphase configuration of magnetite^{12, 13}. At the nanoscale⁶, FeO is replaced by a direct equilibrium between phases of metallic Fe and Fe₃O₄.

This study provides direct experimental evidence that nanoscale FeO is indeed thermodynamically unstable. Assembly of iron oxide nanoparticles in 1-dimensional nanochains and subsequent reduction demonstrates the ability to stabilize FeO at length scale scales below 50 nm⁶. Nanoscale stabilization of metal(II)oxides is promising for catalytic and nanometric solid state memory applications due to the existence of multiphase metal oxides¹⁴ with complex defect structures and related physical properties¹³.

3.2 Materials & Methods

In-situ transmission electron microscopy (TEM) combined with electron energy-loss spectroscopy (EELS) was used to directly observe the temperature-dependent phase stability of nanometric iron oxides, including Fe_2O_3 , Fe_3O_4 and FeO . In-situ heating experiments were carried out with a JEOL JEM 2100AC aberration-corrected STEM at an oxygen partial pressure of $p\text{O}_2 = 7 \times 10^{-9}$ mbar. For in-situ heating, SiC heating membranes that are part of a micro-electro-mechanical system (MEMS) were used as TEM sample support (Figure 3.1 (a)). Sample geometries included (1) individual $\gamma\text{-Fe}_2\text{O}_3$ nanoparticles with diameters around 46 nm dispersed onto the TEM sample support; (2) chains of interconnected nanoparticles that were collected during their synthesis above a self-sustaining diffusion flame within a homogeneous magnetic field¹⁵. Electron energy-loss spectra of the O K and Fe $L_{2,3}$ edges were recorded with an energy dispersion of 0.3 eV/channel. The energy resolution was around 0.9 eV (FWHM of the zero-loss peak). All spectra were background subtracted using power-law fitting and calibrated by zero-loss centering. The probe-forming convergence semi-angle was 23.4 mrad, and the collection semi-angle was approximately 15 mrad. Particle configurations were heated from room temperature to 900 °C at 5 °C/s. All data were recorded after holding samples for at least 10 min at the reported temperatures. Electron micrographs, energy-loss spectra, and selected area electron diffraction (SAED) patterns converged within 10 min of isothermal annealing and are thus assumed to represent thermodynamically stable configurations.

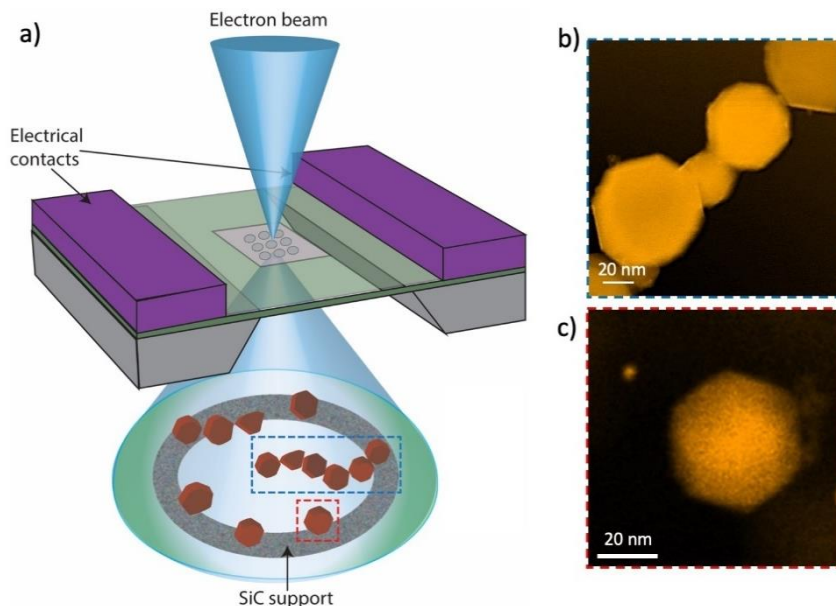


Figure 3.1 (a). Sketch of the experimental setup displaying the MEMS heating device and the incoming focused electron. Below the MEMS device is an exploded view of the sample geometry. (b) and (c) are HAADF micrographs of nanochains and isolated nanoparticles, respectively, that are supported by the SiC heating membrane.

3.3 Results & Discussion

Nanoparticles and nanochains of interconnected particles were observed by high-angle annular dark field (HAADF) imaging during in-situ heating. Figure 3.1 (b) and 1(c) include micrographs of typical particle configurations at room temperature. Micrographs recorded at different temperatures are included in the Appendix (Figure 1S). Single particles and nanochains undergo roughening transitions between 600°C and 800°C. Above 800°C sublimation of isolated particles is observed, while adjacent nanoparticles within nanochains began coarsening around 900°C (ref. ¹⁶ and Figure 1S). The different evolution of nanoparticle and nanochain morphologies with increasing temperature indicates a change in their redox behavior. Near-edge fine structures (ELNES) of the Fe L_{2,3} absorption edges were recorded as a function of temperature to determine changes in oxidation states for Fe cations.

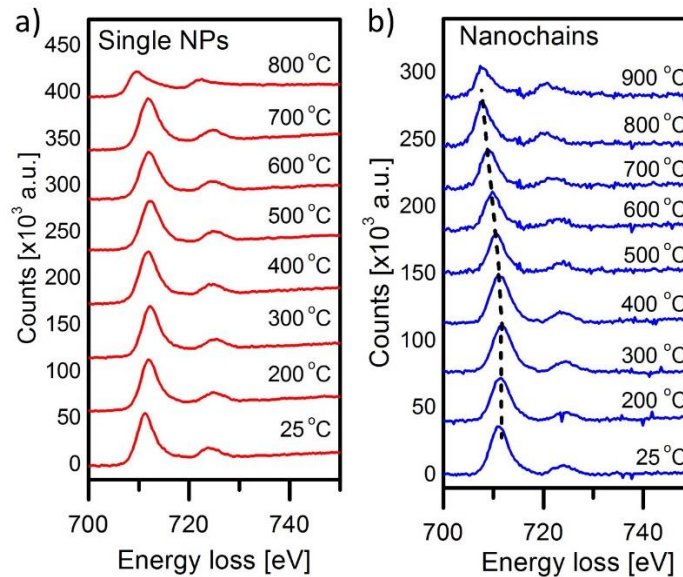


Figure 3.2 Background-stripped Fe L_{2,3} edges acquired from (a) isolated particles and (b) individual nanochains after annealing to the indicated temperatures. The dotted line highlights a systematic shift of spectra towards lower energy-losses.

Figure 3.2 shows background stripped Fe L_{2,3} edges as a function of energy loss and annealing temperature for isolated nanoparticle and nanochain configurations. For isolated particles the ELNES line shapes exhibit no significant change with increasing temperature other than a reduction of the L₂/L₃ intensity ratio above 700°C (Figure 3.2 a). From nanochains, however, a reduction of the L₂/L₃ intensity ratios is observed at temperatures as low as 400°C. Unlike for isolated nanoparticles, the onset of the L₃ edge obtained from nanochains continues to shift towards lower energy losses with temperatures increasing above 400°C. For bulk iron oxides such observations are consistent with the nominal reduction of iron cations¹⁷, hence indicating a clear difference of the reduction-oxidation behavior between individual particles and nanochains. For a more detailed identification of the apparent oxidation states, integrated L₃/L₂ intensity ratios were determined following a two Gaussian peak-fitting method¹⁸. The determined intensity ratios are plotted as a function of temperature in Figure 3.3. The decreasing trend in the

Fe L_3/L_2 intensity ratio for both single nanoparticle and nanochain configurations demonstrate continuous Fe reduction with increasing temperature. Most notable is the discrepancy of the white line intensity ratios for individual nanoparticles in the temperature interval between 400°C and 800°C, where values range between 4.8 and 5.2. Ratios obtained from nanochains drop to significantly smaller values between 3.5 and 4.0. The white line intensity ratios observed in this study reproduce those from previous reports that were obtained by the same technique^{17–20}. Comparison of the experimental data to reference data was subsequently used to identify specific iron oxide phases. Discrepancies between the L_3/L_2 intensity ratios found in this study and the reference data listed in Table 1 reflect systematic errors that are attributed to differences in counting statistics and EELS processing parameters, including the widths of energy intervals for spectrum integration and continuum background fitting. The observed L_3/L_2 intensity ratios reveal that *in situ* annealing of the iron oxide nanochains resulted in the transition from γ -Fe₂O₃ to Fe₃O₄ at 250 °C, followed by FeO between 400 °C and 800 °C, and metallic Fe above 800 °C. In contrast, individual nanoparticles maintain white line intensity ratios consistent with Fe₃O₄ between 250 °C and 700 °C, before an abrupt reduction to metallic Fe at 800 °C. No evidence was detected for FeO composition in the case of isolated nanoparticles. Complete reduction to metallic Fe was confirmed for both configurations using integrated oxygen intensities indistinguishable from the experimental noise.

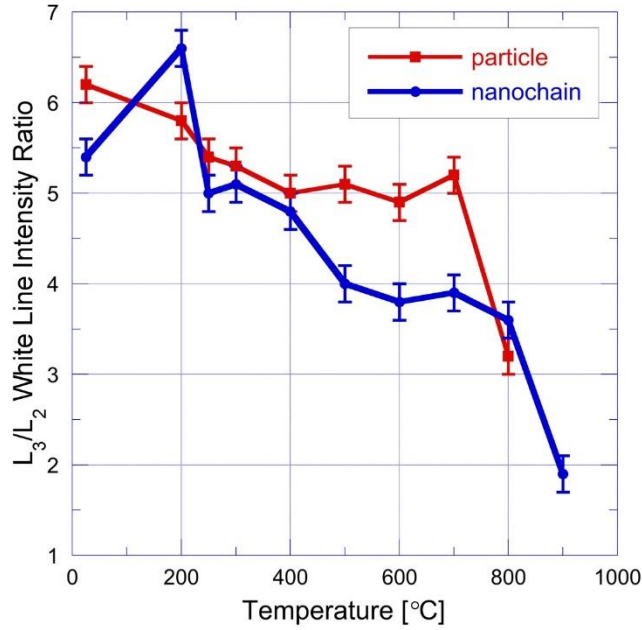


Figure 3.3 L_3/L_2 white line intensity ratios extracted from Figure 3.2 plotted as a function of temperature for both individual nanoparticles (red squares) and nanochains (blue circles). Error bars are ± 0.2 .

Table 1. Reference data for L_3/L_2 intensity ratios assigned to specific iron oxides. The listed data were obtained with identical methods utilized in this study.

Fe L_3/L_2 intensity ratio	Assigned Phase
6.5 ± 0.3	$\alpha\text{-Fe}_2\text{O}_3$ ¹⁹
6.0 ± 0.3	$\alpha\text{-Fe}_2\text{O}_3$ ²⁰
5.8 ± 0.3	$\gamma\text{-Fe}_2\text{O}_3$ ¹⁹
5.5 ± 0.3	$\gamma\text{-Fe}_2\text{O}_3$ ^{18,20}
5.2 ± 0.3	$\gamma\text{-Fe}_3\text{O}_4$ ^{19,20}
4.6 ± 0.3	FeO ¹⁹
4.4 ± 0.3	FeO ¹⁸
3.0	Fe ¹⁷

EELS experiments were carried out either during in-situ heating to the reported temperatures, or immediately after rapid cooling to room temperature. ELNES line shapes and their respective L_3/L_2 intensity ratios revealed no detectable differences, irrespective of whether they were recorded during in-situ heating or after cooling. The gradual reduction of Fe during in-

situ heating indicates the irreversible formation of thermodynamically stable phases for the specific experimental conditions, i.e. temperature intervals and oxygen partial pressure. Re-oxidation during cooling of the sample is suppressed due to the insufficient oxygen partial pressure in the continuously pumped vacuum.

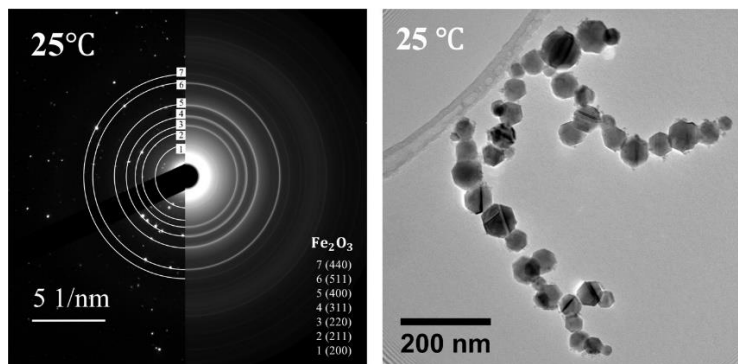


Figure 3.4 SAED pattern and bright field TEM image of $\gamma\text{-Fe}_2\text{O}_3$ nanochains recorded before thermal annealing at 25 °C. For more accurate determination of reciprocal lattice spacings SAED patterns were rotationally averaged.

For individual nanoparticles and nanochains the phase transformation from Fe_2O_3 to Fe_3O_4 initiated at 250 °C. The Fe_3O_4 phase was maintained up to 700 °C in the case of isolated nanoparticles. Transition to the FeO phase was observed for nanochains around 400 °C. Nanochains retained the FeO phase to temperatures as high as 800 °C while no FeO phase was detected for isolated nanoparticles. The shape of the nanoparticles however changed from faceted to round starting at approximately 600 °C before mass loss due to sublimation occurred. The presence of the FeO phase within the nanochain configuration was independently confirmed by in-situ SAED experiments. Figure 3.4 shows an SAED pattern and a bright field TEM image recorded from the same Fe_2O_3 nanochains before thermal annealing. Figure 3.5 shows radial intensity line profiles as a function of reciprocal lattice spacings extracted from rotationally averaged diffraction patterns that were recorded from the same nanochain at different

temperatures. At room temperature (Figure 3.5a) observed reciprocal lattice spacings are in excellent agreement with those reported from previous SAED and X-ray powder diffraction studies for γ -Fe₂O₃^{21,22}. Both maghemite and magnetite (Fe₃O₄) crystallize with the cubic spinel structure (space group Fd-3m), which makes it challenging to distinguish the two phases from each other. However, the relatively small particle diameters combined with the excitation error for the TEM experiments result in the appearance of kinetically forbidden diffraction spots, including the (211) peak observed at room temperature (Figure 3.5a) which is exclusive for γ -Fe₂O₃²¹. Its absence from the SAED patterns recorded at 600°C (cf. Figure 3.5b) provides evidence for the phase transformation from γ -Fe₂O₃ to Fe₃O₄. SAED patterns recorded after continuous heating to 800°C exhibit significantly different distributions of diffraction intensities. Figure 3.5c reveals peak intensities that are in excellent agreement with {111}, {200}, and {220} lattice planes in FeO. The small remanence of diffraction intensities coinciding with {222}, {400}, and {511} reflections in Fe₃O₄ suggest a gradual transformation of the nanochains from Fe₃O₄ to FeO. Such transformation kinetics are expected since the three iron oxides are comprised of similar closed packed arrays of oxygen anions, in which iron cations can easily move between octahedral and tetrahedral sites. It was previously reported that free surface activities change as a function crystallographic orientation²³⁻²⁵, which suggests that different facets of the nanoparticles will obey slightly different reduction kinetics. SAED patterns recorded at 900°C are in excellent agreement with those expected for metallic γ -Fe (cf. Figure 5d). The TEM micrograph in the inset of Figure 3.5d demonstrates sintering of nanochains.

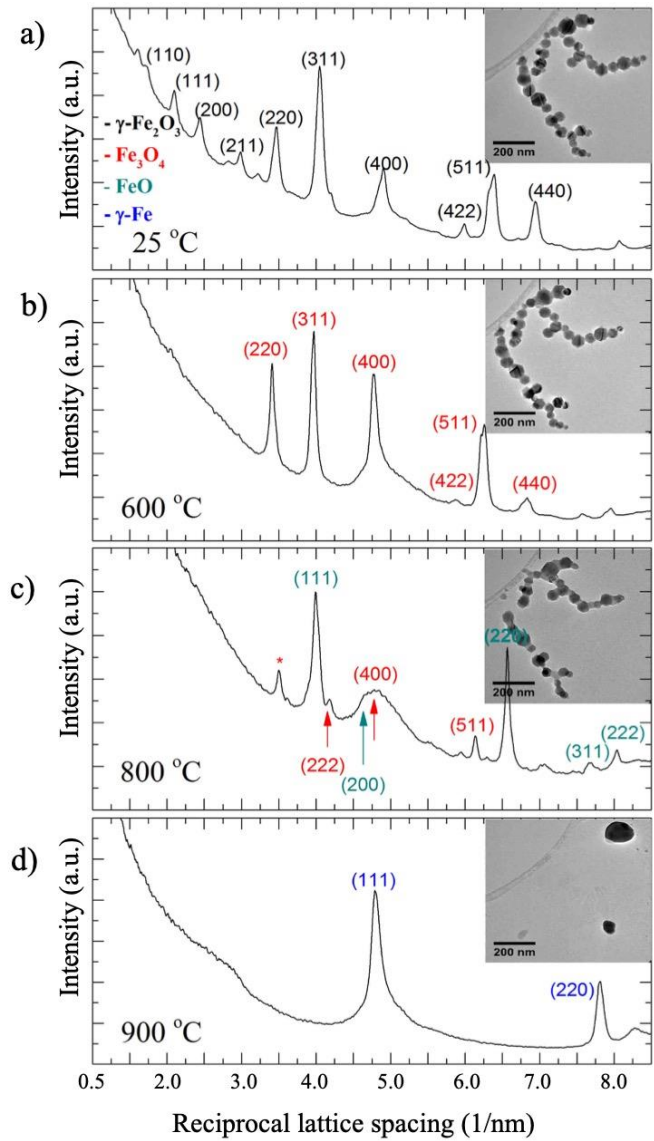


Figure 3.5 Rotationally average reciprocal lattice spacings extracted from SAED patterns recorded between 25°C and 900°C. Lattice spacings for γ -Fe₂O₃, Fe₃O₄, Fe, and metallic Fe are labeled with respective Miller indices.

EELS and SAED experiments during in-situ annealing directly confirm stabilization of the FeO phase on the nanoscale provided nanoparticles are arranged in nanochain configurations. This result is remarkable since the FeO phase remains confined within 50-70 nm in two

independent directions, while phase stabilization is accommodated by interconnecting adjacent particles.

Navrotsky et al.⁶ have argued that differences in surface energies have a strong influence on phase stability by shifting redox free energies by up to 30 kJ/mol. Size-driven thermodynamic crossovers in phase stability at the nanoscale are a result of the changes in the free energies of polymorphs due to differences in surface energies^{6, 26–29} Thermodynamic calculations have predicted that isolated FeO nanoparticles with diameters below 100 nm are unstable and Fe₃O₄ and Fe phases coexist⁶. The EELS results for isolated particles observed in this study provide direct experimental evidence for the coexistence of Fe₃O₄ and Fe. Temperatures as low as 400°C, however, reveal the stabilization of the FeO phase for nanochains with lengths equivalent to 6 to 8 particle diameters. The assembly of individual nanoparticles into chain-like geometries and partial sintering between particles (Figure S1 and reference¹⁶) leads to the formation of particle/particle contacts with grain boundary energies lower than the specific surface energies. This effect alongside potential particle rotation and faceting decreases the total surface energy of the particle ensemble and stabilizes the FeO phase.

EELS data recorded from nanochains consisting of less than 4 interconnected particles did not reveal any FeO formation at temperatures as high as 700°C. Instead, magnetite transformed directly to the metal phase, indicating that nanochains of at least 4 particles, or an equivalent length of about 180 nm are required to stabilize FeO. Considering particle diameters of 46 nm, and interparticle neck diameters around 24-26 nm (see Figure S1), surface to volume ratios of nanochains comprising of at least 6 nanoparticles are 12-14% smaller than those observed for individual nanoparticles of the same size. Surface to volume ratios for 6-particle nanochains are similar to those of individual nanoparticles with diameters around 50-60 nm,

potentially suggesting that particle sizes considerably smaller than those previously estimated may present stability of FeO. Purely geometric arguments in conjunction with earlier analysis of redox phase equilibria⁶ suggest that the stabilization of metal(II)oxide phases in nanochain configurations may be a general phenomenon not restricted to only iron oxides. Phase stability for CoO was reported during reduction reactions of thin films³⁰. The relatively low Fe₃O₄ to FeO transition temperature of 400 °C is consistent with previous indirect observations for thin metal-oxide films³¹.

The results of this study demonstrate the potential to stabilize metal(II)oxides on length scales where they were previously considered unstable. For individual nanoparticles, the stability of metal(II)oxides is inhibited by the larger total surface energy. At the nanoscale increasing surface area to volume ratios can be considered as extra pressure due to increased surface tension, which makes the formation of metal(II)oxides energetically unfavorable compared to 1-dimensional nanochains. The relatively smaller grain boundary energies compared to free surface energies further suggest the ability to similarly stabilize microstructures of nanocrystalline metal(II)oxides. A prediction of critical nanochain length however requires consideration of free surface energies, specific grain boundary energies, redox potentials and oxygen partial pressures. The ability to stabilize nanoscale metal(II)oxides, and especially FeO, will enable applications in nano-magnetic and catalyst technologies for next generation memory devices and more efficient hydrogenation of nitroarenes during the manufacturing of pharmaceuticals and agricultural chemicals.

Acknowledgement

This work was supported by the US National Science Foundation (grant DMR-0955638), the Army Research Office under grants #W911NF-12-10491 (program manager Dr. David Stepp),

and #W911F-16-1-0364 (program manager: Dr. Michael Bakas). The authors acknowledge invaluable discussions with G. Das, I. Kennedy, and A. Navrotsky.

3.4 References

1. Pan ZW, Dai ZR, Wang ZL. Nanobelts of Semiconducting Oxides. *Science*. 2001;291(5510):1947–1949. <https://doi.org/10.1126/science.1058120>
2. Roduner E. Size matters: why nanomaterials are different. *Chem Soc Rev*. 2006;35(7):583–592. <https://doi.org/10.1039/B502142C>
3. Matsuno M, Bonifacio CS, Rufner JF, *et al.* In situ transmission electron microscopic investigations of reduction-oxidation reactions during densification of nickel nanoparticles. *Journal of Materials Research*. 2012;27(18):2431–2440. <https://doi.org/10.1557/jmr.2012.256>
4. Lee J-G, Mori H. Solid solubility in isolated nanometer-sized alloy particles in the Sn-Pb system. *Eur Phys J D*. 2005;34(1):227–230. <https://doi.org/10.1140/epjd/e2005-00148-y>
5. Wautelet M. Estimation of the variation of the melting temperature with the size of small particles, on the basis of a surface-phonon instability model. *J Phys D: Appl Phys*. 1991;24(3):343–346. <https://doi.org/10.1088/0022-3727/24/3/017>
6. Navrotsky A, Ma C, Lilova K, Birkner N. Nanophase transition metal oxides show large thermodynamically driven shifts in oxidation-reduction equilibria. *Science*. 2010;330(6001):199–201. <https://doi.org/10.1126/science.1195875>
7. Bajaj S, Haverty MG, Arróyave R, Frsc WAGI, Shankar S. Phase stability in nanoscale material systems: extension from bulk phase diagrams. *Nanoscale*. 2015;7(21):9868–9877. <https://doi.org/10.1039/C5NR01535A>
8. G. V. Samsonov. *The Oxide Handbook*. American Edition. New York, NY: 1973
9. Harris RA, Shumbula PM, van der Walt H. Analysis of the Interaction of Surfactants Oleic Acid and Oleylamine with Iron Oxide Nanoparticles through Molecular Mechanics Modeling. *Langmuir*. 2015;31(13):3934–3943. <https://doi.org/10.1021/acs.langmuir.5b00671>
10. Koo B, Xiong H, Slater MD, *et al.* Hollow Iron Oxide Nanoparticles for Application in Lithium Ion Batteries. *Nano Lett*. 2012;12(5):2429–2435. <https://doi.org/10.1021/nl3004286>

11. Qi X, Xu J, Zhong W, Du Y. A facile route to synthesize core/shell structured carbon/magnetic nanoparticles hybrid and their magnetic properties. *Materials Research Bulletin*. 2015;67:162–169. <https://doi.org/10.1016/j.materresbull.2015.03.027>
12. Darken LS, Gurry RW. The System Iron—Oxygen. II. Equilibrium and Thermodynamics of Liquid Oxide and Other Phases. *J Am Chem Soc*. 1946;68(5):798–816. <https://doi.org/10.1021/ja01209a030>
13. Chen C-J, Chiang R-K, Lai H-Y, Lin C-R. Characterization of Monodisperse Wüstite Nanoparticles following Partial Oxidation. *J Phys Chem C*. 2010;114(10):4258–4263. <https://doi.org/10.1021/jp908153y>
14. Minervini L, Grimes RW. Defect clustering in wüstite. *Journal of Physics and Chemistry of Solids*. 1999;60(2):235–245. [https://doi.org/10.1016/S0022-3697\(98\)00273-X](https://doi.org/10.1016/S0022-3697(98)00273-X)
15. Das GK, Bonifacio CS, Rojas JD, Liu K, Benthem K van, Kennedy IM. Ultra-long magnetic nanochains for highly efficient arsenic removal from water. *J Mater Chem A*. 2014;2(32):12974–12981. <https://doi.org/10.1039/C4TA02614D>
16. Bonifacio CS, Das G, Kennedy IM, van Benthem K. Reduction reactions and densification during in situ TEM heating of iron oxide nanochains. *Journal of Applied Physics*. 2017;122(23):234303. <https://doi.org/10.1063/1.5004092>
17. Leapman RD, Grunes LA, Fejes PL. Study of the L_{23} edges in the 3d transition metals and their oxides by electron-energy-loss spectroscopy with comparisons to theory. *Phys Rev B*. 1982;26(2):614–635. <https://doi.org/10.1103/PhysRevB.26.614>
18. Jasinski J, Pinkerton KE, Kennedy IM, Leppert VJ. Spatially Resolved Energy Electron Loss Spectroscopy Studies of Iron Oxide Nanoparticles. *Microscopy and Microanalysis*. 2006;12(5):424–431. <https://doi.org/10.1017/S1431927606060491>
19. Colliex C, Manoubi T, Ortiz C. Electron-energy-loss-spectroscopy near-edge fine structures in the iron-oxygen system. *Phys Rev B*. 1991;44(20):11402–11411. <https://doi.org/10.1103/PhysRevB.44.11402>
20. Pearson DH, Fultz B, Ahn CC. Measurements of 3d state occupancy in transition metals using electron energy loss spectrometry. *Appl Phys Lett*. 1988;53(15):1405–1407. <https://doi.org/10.1063/1.100457>
21. Kim W, Suh C-Y, Cho S-W, *et al*. A new method for the identification and quantification of magnetite–maghemite mixture using conventional X-ray diffraction technique. *Talanta*. 2012;94:348–352. <https://doi.org/10.1016/j.talanta.2012.03.001>

22. Ding Y, Morber JR, Snyder RL, Wang ZL. Nanowire Structural Evolution from Fe₃O₄ to ϵ -Fe₂O₃. *Advanced Functional Materials*. 2007;17(7):1172–1178. <https://doi.org/10.1002/adfm.200601024>
23. Li W, Yang KR, Yao X, *et al.* Facet-Dependent Kinetics and Energetics of Hematite for Solar Water Oxidation Reactions. *ACS Appl Mater Interfaces*. 2019;11(6):5616–5622. <https://doi.org/10.1021/acsami.8b05190>
24. Lee I, Delbecq F, Morales R, Albiter MA, Zaera F. Tuning selectivity in catalysis by controlling particle shape. *Nature Mater*. 2009;8(2):132–138. <https://doi.org/10.1038/nmat2371>
25. Tian N, Zhou Z-Y, Sun S-G, Ding Y, Wang ZL. Synthesis of Tetrahedral Platinum Nanocrystals with High-Index Facets and High Electro-Oxidation Activity. *Science*. 2007;316(5825):732–735. <https://doi.org/10.1126/science.1140484>
26. Navrotsky A, Mazeina L, Majzlan J. Size-Driven Structural and Thermodynamic Complexity in Iron Oxides. *Science*. 2008;319(5870):1635–1638. <https://doi.org/10.1126/science.1148614>
27. McHale JM, Auroux A, Perrotta AJ, Navrotsky A. Surface Energies and Thermodynamic Phase Stability in Nanocrystalline Aluminas. *Science*. 1997;277(5327):788–791. <https://doi.org/10.1126/science.277.5327.788>
28. Ranade MR, Navrotsky A, Zhang HZ, *et al.* Energetics of nanocrystalline TiO₂. *Proceedings of the National Academy of Sciences*. 2002;99(suppl_2):6476–6481. <https://doi.org/10.1073/pnas.251534898>
29. Navrotsky A. Calorimetry of nanoparticles, surfaces, interfaces, thin films, and multilayers. *The Journal of Chemical Thermodynamics*. 2007;39(1):1–9. <https://doi.org/10.1016/j.jct.2006.09.011>
30. Papaefthimiou V, Dintzer T, Dupuis V, *et al.* Nontrivial Redox Behavior of Nanosized Cobalt: New Insights from Ambient Pressure X-ray Photoelectron and Absorption Spectroscopies. *ACS Nano*. 2011;5(3):2182–2190. <https://doi.org/10.1021/nn103392x>
31. Bertram F, Deiter C, Pflaum K, Suendorf M, Otte C, Wollschläger J. In-situ x-ray diffraction studies on post-deposition vacuum-annealing of ultra-thin iron oxide films. *Journal of Applied Physics*. 2011;110(10):102208. <https://doi.org/10.1063/1.3661655>

Chapter 4: In situ anisotropic NiO nanostructure growth at high temperature and under water vapor¹

Anisotropic growth of nanostructures from individual nickel nanoparticles was observed during in-situ heating experiments in an environmental scanning electron microscope at 800 °C under water vapor atmosphere. The morphology of nanostructures exhibited one directional growth with rates ranging below 1.8 nm/s. Energy dispersive X-ray spectroscopy and selected area electron diffraction confirmed NiO stoichiometry of the growing nanostructures. Variations of the oxygen partial pressure during ex-situ annealing and in-situ ESEM heating experiments elucidate that anisotropic NiO growth is energetically favored in areas where the local surface energy density is relatively high. Growth of NiO nanostructures was absent in dry air and dry nitrogen environments and required the presence of water vapor. The results of this study suggest that the manipulation of surface energy prior to exposure to water vapor at elevated temperatures can prevent unwanted oxide nanostructure growth.

4.1 Introduction

Nanoparticles have drawn much attention due to their unique physical and chemical properties owing to their high surface-to-volume ratio. Maintaining the desired properties of transitional metal nanoparticles for technological applications requires a detailed understanding and control of the oxidation behavior. Corrosion phenomena of metallic nickel and its alloys

¹ Published as B. Qu, K. van Benthem, *Journal of the American Ceramic Society* **105** (2022) 2454–2464. © 2021 The American Ceramic Society. Reprinted with permission.

have been studied extensively¹⁻³. The oxidation behavior of nickel nanoparticles in air was previously discussed with regards to their size in comparison to the bulk^{4,5}. When exposed to air, a 2-3 nm thick nickel oxide layer forms on the surface of nickel particles⁶⁻⁸. For sintering of metal particles Munir and colleagues⁹ have predicted the retardation of inter-particle neck formation and, thus, densification owing to the presence of oxide layers. Others have subsequently provided experimental evidence for surface cleaning effects, i.e., the removal of nickel oxide layers from necks between metallic nickel particles at elevated temperatures^{6,10}. In the presence of molecular oxygen or water vapor, gas molecules adsorb onto the metal surface, which is considered the first step towards metal oxidation. Above 600°C oxidation of nickel nanoparticles is facilitated by the outward diffusion of metal cations and the inward diffusion of oxidant molecules from the gaseous environment^{4-7,11}. Differences in the respective diffusion coefficients lead to the Kirkendall effect that was previously observed during the oxidation of nickel nanoparticles⁷. The Gibbs adsorption isotherm describes the relationship between change of the surface energy as a function of surface excess¹². Thus, surface anisotropy of nickel oxide influences adsorption of oxidant molecules and is expected to affect oxidation rates on different crystallographic planes. Anisotropic growth of NiO nanorods from nickel and nickel alloy nanoparticles due to rapid oxidation in O₂ was documented by Koga and Hirisawa^{8,13}. The authors proposed that nanorod growth begins with the nucleation of a triangular NiO islands on sections of the nickel particle surface to form (111) interfacial planes. Subsequent nanorod growth of NiO was argued to be maintained by relatively large oxygen diffusion rates in sub-surface areas of nickel particles above 400°C that enable the transport of dissolved oxygen to the nucleated Ni/NiO interface.

The presence of water vapor in addition to molecular oxygen can have considerable influence on the oxidation behavior of metals ¹⁴⁻²⁰. Rahmel ²¹ stated that water vapor does not change the kinetics of oxidation of nickel and nickel alloys. However, water vapor can cause distinguishable features on the surface of the oxide scale during oxidation. Raynaud and Rapp ¹⁵ have reported whisker formation during nickel oxidation in both dry and water vapor environments. Whiskers formed on the surface of electropolished polycrystalline nickel disks heated at 1100 °C in oxygen with water vapor at a base pressure of 30 Pa. In dry oxygen rough interface morphologies displaying pyramidal structures and pits were observed¹⁵. On cold worked nickel grids heated to 1000 °C whisker growth was observed in dry oxygen with whiskers growing faster, longer, and thinner in the presence of water vapor. Proposed growth mechanisms rely on cation diffusion along the screw dislocation cores, i.e., the longitudinal direction of the whiskers, while lattice diffusion is responsible for lateral growth. This mechanism was initially proposed by Tallman and Gulbransen ²² for the formation of α -Fe₂O₃ whiskers during the oxidation of iron at 400-500 °C. Several studies on Ni alloys have demonstrated different oxidation behaviors in water vapor environments compared to molecular oxygen gas ²³⁻²⁷.

Different mechanisms have been proposed for the effect of water vapor on metal oxidation. Norby ²⁸ has suggested an increase in cation diffusion rate as a consequence of maintaining charge neutrality due to increased proton hopping between oxygen ions at temperatures as high as 1500 °C. In a more recent study Luo and co-workers ²⁴ found that Ni-Al alloy single crystal thin films oxidized in water vapor reveal a relaxed incoherent oxide/metal interface instead of a highly strained coherent interface that forms during oxidation in O₂. A faster inward diffusion of oxidant molecules was observed in the presence of water vapor and is attributed to the lower interface energy ²⁴.

This study reports the direct in-situ observation of anisotropic growth of NiO nanostructures during the controlled oxidation of Ni nanoparticles at high temperatures in the presence of water vapor. In-situ environmental scanning electron microscopy (ESEM) was used to observe morphological changes of nickel nanoparticles as a function of water vapor pressure and time. Systematic ESEM studies combined with ex-situ thermal annealing prior to ESEM heating allows for the identification of oxidation and nanostructure growth mechanisms.

4.2 Experimental Details

4.2.1 Specimen Preparation

Nickel nanoparticles with a nominal diameter of 300 nm (SkySpring Nanomaterials, Inc., Houston, TX) were dispersed in isopropanol and sonicated for 15 minutes. The suspension was then drop-casted onto a thermally grown 12 nm thick SiO₂ film supported by a silicon substrate (Figure 4.1(a)). For anticipated TEM characterization following ESEM heating particles were drop-casted onto an 18nm thick electron transparent silicon dioxide membrane (Figure 4.1(b)) that is part of a commercially available TEM specimen grid (Ted Pella, Inc.).

Samples were separated into four groups: A, B, C and D. Samples of group A were not annealed. Sample groups B, C, and D were thermally annealed under high vacuum (base pressure 10⁻⁶ to 10⁻⁵ mbar) in a glass tube furnace (MTI Corporation, Richmond, CA) for 2-7 hours. Annealing conditions are summarized in Table 2. The nominal annealing temperature for all samples was 750 °C. Actual annealing temperatures measured with a separate thermocouple are included in Table 2. Laminar argon flow before vacuum pumping was utilized for sample groups C and D to purge air from the glass tube in order to further minimize the oxygen partial pressure during subsequent annealing. The annealing process in the tube furnace prior to any

ESEM characterization will be referred to as ‘pre-annealing’ throughout the remainder of the manuscript.

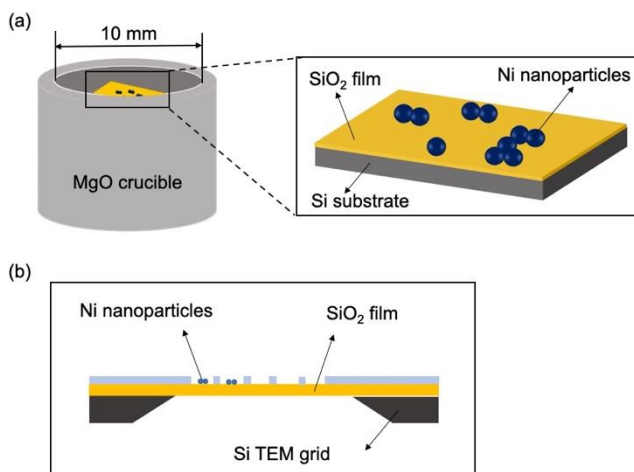


Figure 4.1 Samples are placed into the magnesium oxide crucible of a ThermoFisher heating stage for in-situ heating experiments. (a) Detailed sketch of the samples. Spheres represent nickel nanoparticles; the yellow layer represents the thermally grown silicon oxide supported by a silicon substrate wafer (for illustration purposes only, not to scale). (b) Nickel nanoparticles dispersed onto a TEM grid with silicon dioxide film (grid commercially available from Ted Pella Inc.).

Table 2: Annealing conditions for each sample group before in-situ ESEM heating.

Sample group	Pre-annealing temperature (°C)	Pre-annealing time (hours)	Base pressure (Pa)	Argon purging before pumping
A	<i>no pre-annealing</i>			
B	795	4	$10^{-3} - 10^{-2}$	No
C	795	2		Yes
D	785	7		Yes

4.2.2 ESEM heating

In-situ heating experiments were carried out on all sample groups with a ThermoFisher Quattro Environmental Scanning Electron Microscope (Thermo Fischer Scientific, Hillsboro, OR). A variety of different gas environments was utilized, including dry nitrogen (N₂), dry air, and water vapor. After insertion of the samples air was purged from the microscope chamber using three cycles of pumping to a base pressure of about 50 Pa and subsequent backfilling with the respective process gas. Dry N₂ used during ESEM imaging had a purity of 99.995%, and was connected directly to the auxiliary gas inlet of the ESEM instrument. Dry air was generated by directing laboratory air through copper tubing immersed in liquid N₂ to condense moisture. For experiments under water vapor atmosphere a glass beaker filled with distilled water was evacuated and heated to 30°C to 40°C. The vapor phase above the heated water surface was directed into the microscope chamber. Throughout the remainder of this manuscript in-situ growth experiments will be referred to as '*ESEM heating*'.

Samples were placed into a magnesium oxide crucible that is part of the ThermoFisher in-situ heating stage. A drop of de-ionized water between the silicon wafer and the crucible was used to adhere the sample during initial pumping. Particle agglomerates were heated from room temperature to 800°C (1073 K) at a heating rate of 30-50 °C/min. The temperature was then held constant at 800 °C for at least 20 minutes until no more morphological changes of particle agglomerates were detected during heating. Multiple in-situ heating experiments were carried out at water vapor pressures ranging between 250 Pa and 400 Pa, under dry nitrogen gas atmosphere at a base pressure of 350 Pa and dry air at base pressure of 350 Pa.

Imaging during ESEM heating experiments was carried out at an acceleration voltage of 30 keV and a pixel dwell time of 0.5ms using the gaseous secondary electron detector (GSED).

Images were continuously recorded at a rate of 60 stills/min and stored as video files. The continuous video acquisition was stopped intermittently to allow for slow-scan single frame acquisition. Biasing of the heat shield and the sample stage was applied to maximize image contrast. Image signals extracted from the video files were integrated over 5-6 seconds to generate series of micrographs for subsequent image analysis using the ImageJ software package²⁹. The TurboReg plug-in for ImageJ³⁰ was employed for in-plane alignment of micrographs. An image analysis procedure was developed to ensure consistency in measuring changes in length of the emerging nanostructures as a function of time. For each series of micrographs, a fixed growth direction was defined. The intersection point of the growth direction and a perpendicular line through the center of mass of the respective particle agglomerate was set as the reference point for length measurements.

Energy dispersive x-ray spectroscopy (EDXS) data were recorded at room temperature and under high vacuum conditions (base pressures of $\sim 10^{-3}$ Pa) before and after in-situ heating with a Bruker Quantax 400 XFlash 6 solid-state detector. EDXS maps were acquired from selected areas that include particle agglomerates of interest, followed by the acquisition of an additional data set under identical experimental conditions from an adjacent area that contains only the sample support (cf. Figure 4.1a). Nanoparticle specific EDXS signals ($I_{(\text{particle})}$) were calculated following equations (4.1) and (4.2).

$$I_{(\text{particle})} = I_{(\text{particles} + \text{support})} - \alpha \times I_{(\text{support})} \quad (4.1)$$

$$\alpha = \frac{I_{\text{SiK}\alpha(\text{particles} + \text{support})}}{I_{\text{SiK}\alpha(\text{support})}} \quad (4.2)$$

$I_{(\text{particles} + \text{support})}$ represent the as-recorded EDXS intensities including both the particle agglomerates and the sample support. $I_{(\text{support})}$ is the intensity recorded from an area nearby that

only includes the sample support. α is a scaling factor calculated by dividing the as-acquired count intensity for the Si K_{α} peak ($E=1.7477$ keV) recorded from both particles and the underlying support by the Si K_{α} peak intensity recorded from the adjacent area that contains only the sample support. The scaling parameter was subsequently maximized while avoiding any negative spectral intensities for $I_{(\text{particle})}$. The Si K_{α} peak was selected under the assumption that the particle agglomerate does not contain any Si. Standardless quantitative EDXS analysis of the particle specific intensities ($I_{(\text{particle})}$) was carried out using the Bruker Esprit software package to determine Ni/O atomic ratios.

4.2.3 TEM Characterization

A selection of particles that were deposited on TEM sample grids (cf. Figure 4.1b) and ESEM annealed were subsequently characterized by transmission electron microscopy. High-angle annular dark field (HAADF) scanning transmission electron microscopy (STEM) imaging was carried out with a JEOL JEM 2100AC aberration corrected scanning transmission electron microscope. High-resolution transmission electron microscopy (HRTEM) and selected area electron diffraction (SAED) experiments were recorded with a Gatan Rio 16 CMOS camera attached to the same instrument. EDXS line scans were acquired with an Oxford Aztec Energy TEM Advanced Microanalysis System with X-MaxN TSR Windowless large area Analytical Silicon Drift Detector. TEM experiments were also carried out with nickel nanoparticles with a nominal diameter of 20 nm. Without any pre-annealing ESEM heating of the 20 nm particles was performed under a base pressure of 350 Pa in water vapor with a heating rate of 30°C /min. Particles were held at the annealing temperature of 800°C for 5 minutes

4.3 Results

4.3.1 ESEM heating

Figures 4.2(a) and 2(b) show SEM survey images recorded from nickel particle agglomerates of Group A before and after ESEM heating at 800°C under 400 Pa of water vapor, respectively. Figures 4.2(c) and 2(d) show the corresponding false-color EDXS maps. Before ESEM heating individual Ni particles reveal spherical shapes and relatively smooth surfaces no appearance of extended facets (cf. Figure 4.2(a)). After ESEM heating Figure 4.2(b) reveals the growth of a high-aspect ratio nanostructure which is approximately 860 nm long and between 90nm and 150nm wide. The particle-specific EDXS intensities before (Figure 4.2(c)) and after in-situ heating (Figure 4.2(d)) confirm the presence of both nickel and oxygen while no significant concentrations of other impurities were detected. EDXS signals originating from silicon, aluminum, silver, magnesium and carbon observed in the unprocessed raw data are attributed to the silicon substrate and silicon dioxide film, the SEM sample stub, silver paste for sample mounting, the heating crucible made from magnesium oxide, and carbon contamination during image acquisition, respectively. A more detailed description and discussion of particle specific EDXS results is provided further below and summarized in Table 3.

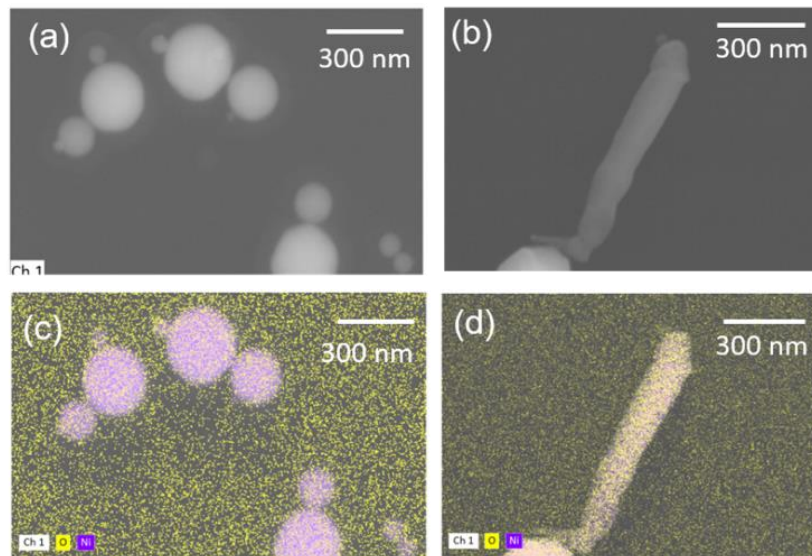


Figure 4.2 SEM images of different nickel nanoparticle agglomerates (a) at room temperature prior to heating and (b) after heating in 400 Pa of water vapor pressure. (c) and (d) present corresponding EDXS chemical distribution maps. The color yellow represents oxygen distribution and violet represents nickel. Micrographs in (a) and (b) were recorded from different agglomerates.

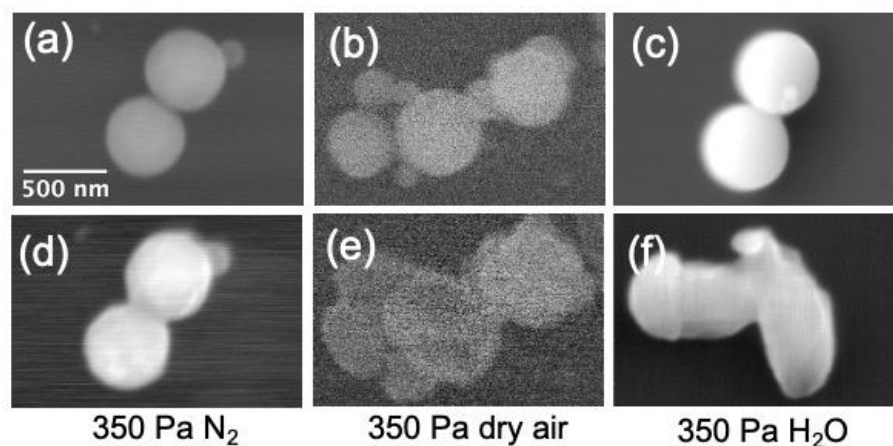


Figure 4.3 ESEM micrographs recorded from Ni nanoparticles before and after ESEM heating under 350Pa of dry nitrogen (a) & d)), 350 Pa of dry air (b) and e)), and 350 Pa of water vapor (c) and f)), respectively.

Figure 4.3 shows ESEM micrographs recorded from two-particle agglomerates from Group A after ESEM heating at 800°C in 350 Pa of dry N₂ (Figure 4.3(a)), dry air (Figure 4.3(b)), and water vapor (Figure 4.3(c)). In the absence of water vapor (Figures 4.3(a) and 4.3(b)) no nanostructures growth was observed. Instead, necks have formed between adjacent particles and particle agglomerates have eventually sintered during ESEM heating. In the presence of water vapor and otherwise identical experimental conditions, however, Figure 4.3(c) reveals the directional growth of a tapered nanostructure. Figure 4.4 shows a series of ESEM images that were recorded during ESEM heating experiments at water vapor pressures ranging between 250 Pa and 400 Pa. In Figures 4.4(f) and (g) the formation of high aspect-ratio nanostructures (in the following referred to as “nanorods”) is observed. In all cases the growth of no more than 1-2 nanorods were observed on any particle. Figures 4.4(e) and (h) however, reveal particle elongation, that is, directional growth characterized by substantially smaller aspect ratios compared to the observed nanorods described above. Both configurations, particle elongation and growth nanorods were observed under water vapor atmosphere irrespective of partial pressure. The supplemental materials include an ESEM heating video of the growing nanostructures recorded at 400 Pa of water vapor pressure.

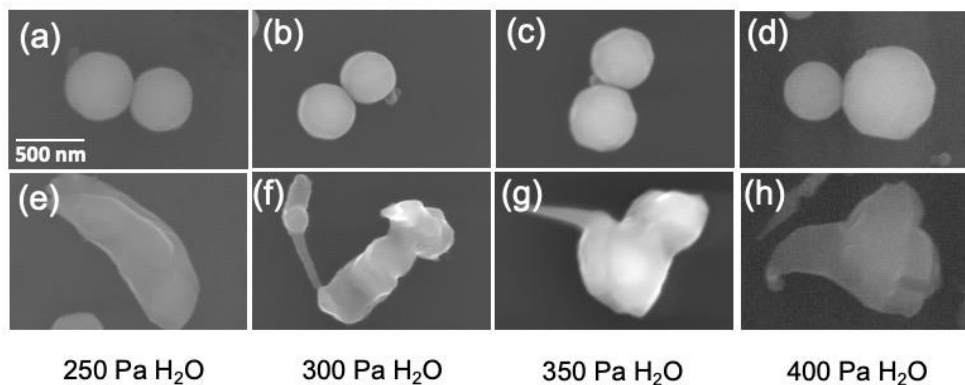


Figure 4.4 ESEM micrographs recorded from Ni nanoparticles before and after ESEM heating under 250 Pa (a & e)), 300 Pa (b and f)), 350 Pa (c and g)), and 400 Pa (d and e)) of water vapor, respectively.

Growth of nanostructures was also observed in areas that were not exposed to the electron beam during ESEM heating. A set of additional ESEM heating experiments under 350 Pa of water vapor was carried out with the electron beam switched off. ESEM imaging after heating in the microscope chamber completed confirmed growth of nanostructures in the absence of exposure to the electron beam.

Image analysis routines described in Methods section were employed to determine growth rates for the nanostructures from the acquired in-situ video data. Growth rates for high aspect ratio nanorod structures is defined as the increase of length in the growth direction per unit time; the growth rate for particle elongation is defined as the increase in length of the longest dimension per unit time. Figure 4.5 shows that growth rates for both high aspect ratio nanostructures and particle elongation as a function of water vapor pressure range between 0.1 and 1.8 nm/s. The growth rate of 2.8 nm/s observed at 300 Pa is considered an outlier. With existing statistics, no obvious trends can be concluded for how the water vapor pressure level affect growth rate.

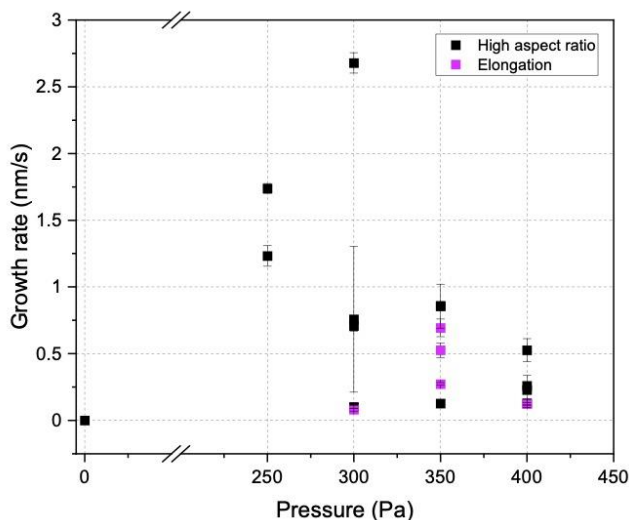


Figure 4.5 Growth rate for nanostructures as a function of water vapor pressure. Black square and violet square symbols represent growth of high aspect ratio structures and particle elongation, respectively.

Nanostructure growth with a variety of different aspect ratios was observed for more than 95% of the particles from Group A and B, while the morphology for more than 95% of particles from Group C and D did not exhibit any nanostructure growth. The only difference of pre-annealing prior to ESEM heating for samples groups C and D compared to groups A and B is whether argon gas was used to purge air from the furnace tube prior to evacuation.

Figure 4.6 shows particles from sample group D after pre-annealing in a tube furnace at 785 °C for 7h. Figure 4.6(a) exhibits a particle with a smooth surface and some faceting, while the particle in Figure 4.6(b) reveals a rougher surface. Figure 4.6(c) and (d) show the same particles after in-situ ESEM heating at 800°C in 350 Pa of water vapor. No noticeable changes in morphology nor any high-aspect ratio nanostructure growth similar to that in Figure 4.4 was observed.

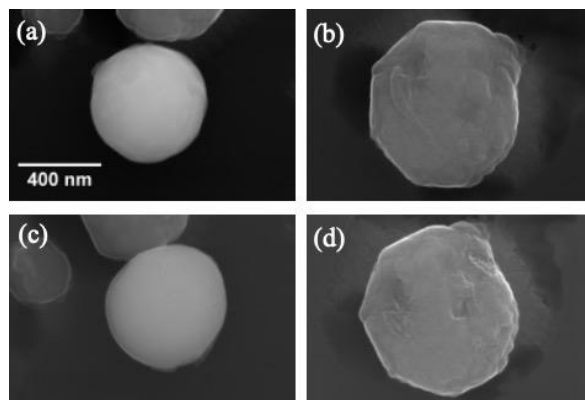


Figure 4.6 ESEM micrographs of two different nickel nanoparticles after pre-annealing in vacuum at 785°C for 7 hours. Images were recorded at room temperature before ((a) and (b)) and after ESEM heating ((c)-(d)). The scale bar applies to all micrographs.

Figure 4.7 shows EDXS spectra recorded after ESEM heating from a particle of sample group D. The Si Ka peak dominates the spectrum that was recorded from the particle and the underlying substrate (cf. $I_{(\text{particle}+\text{support})}$ in equation (4.1)). The scaling factor a was calculated using a spectrum recorded nearby from the underlying substrate only ($I_{(\text{support})}$ in Figure 4.7) following equation (4.2). The resulting particle specific EDXS spectrum $I_{(\text{particle})}$ is shown in Figure 4.7. Table 3 summarizes the EDXS results obtained from particle-specific spectra of all sample groups before and after ESEM heating. Before ESEM heating particles exhibit 90-95 at% Ni and 10-5 at% O. After ESEM heating, however, nickel/oxygen atomic ratios obtained from groups A and B approach values around 1/1, indicating the formation of near-stoichiometric NiO. Samples from group C and D show Ni/O atomic ratios as low as 65/35 and as high as 95/5, indicating partial to no additional oxidation of nickel.

Table 3. Results for EDXS quantitative analysis for pre-annealed nickel particles before and after ESEM heating (*Particles approaching formation of equilibrium crystal shape, with faceted surface).

Annealing condition	Sample	Before ESEM heating		After ESEM heating		High aspect ratio growth
		Ni at. %	O at. %	Ni at. %	O at. %	✓
As received No annealing (Group A)	1	87	13	45	55	✓
	2	93	7	48	52	✓
No Ar flow before pumping 795 °C for 4h (Group B)	1	94	6	53	47	✓
	2	95	5	50	50	✓
	3	94	6	45	55	✓
	4	94	6	50	50	✓
Ar flow before pumping 795 °C for 2h (Group C)	1*	95	5	65	35	✗
	2	98	2	95	5	✗
Ar flow before pumping 785 °C for 7h (Group D)	1*	95	5	68	32	✗
	2	95	5	90	10	✗

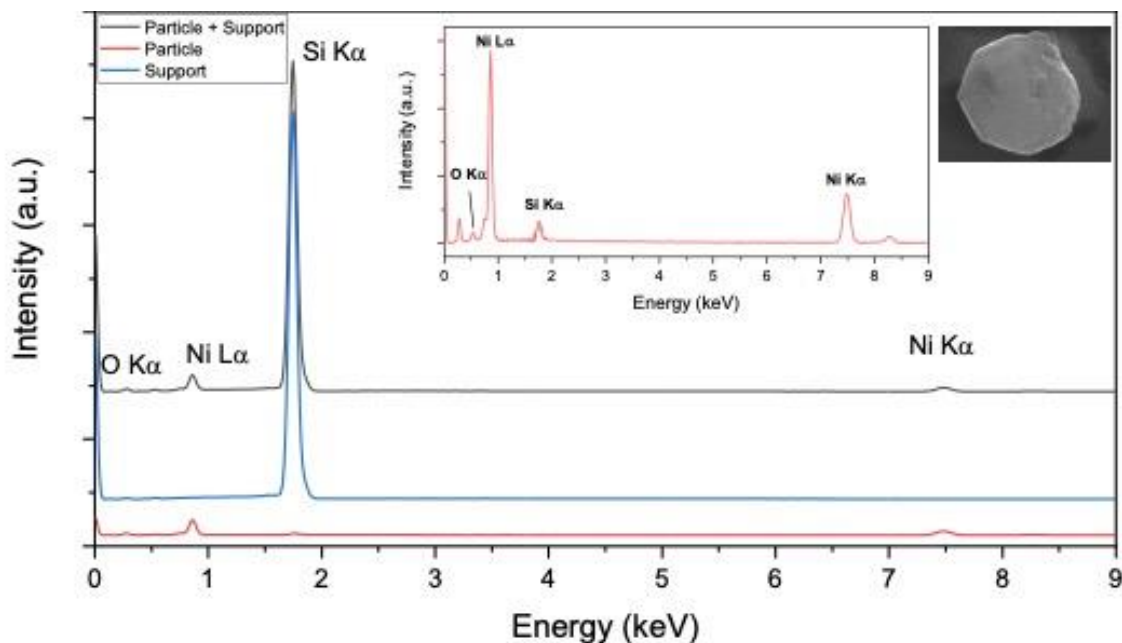


Figure 4.7 EDXS spectra recorded after ESEM heating from the same particle displayed in Figure 4.6d. The plot includes spectra recorded from the particle ($I_{\text{particle+support}}$) and from an adjacent area that only included the underlying support (I_{support}). The particle specific EDXS spectrum (I_{particle}) was calculated using equation (4.2) with a scaling factor $a=0.85$.

4.3.2 TEM characterization

Figure 4.8(a) and 8(b) display HAADF-STEM images recorded from high aspect ratio nanostructures that formed during ESEM heating of sample group A. Figure 4.8(a) demonstrates that nanostructures grow in different directions during ESEM heating. Some nanorods exhibit metal nanoparticles at their tips (Figure 4.8(a)) while others do not (Figure 4.8(b)). The selected area diffraction pattern recorded from another nanostructure shown in Figure 4.8(c) reflects lattice plane spacings that are in excellent agreement with bulk NiO.

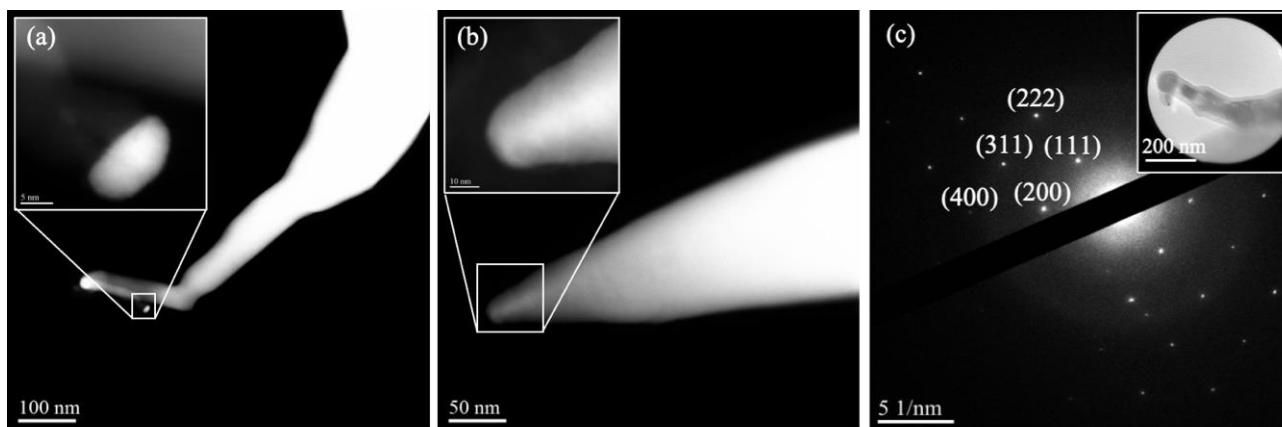


Figure 4.8 (a) & (b) HAADF micrographs of high aspect ratio nanostructures. (c) Selected area electron diffraction pattern of a high aspect ratio nanostructure. Diffraction intensities are indexed according to bulk NiO. The selected area is shown in the inset.

Figure 4.9 (a) and (b) show as-acquired EDXS spectra obtained after ESEM heating from sample Group A during STEM characterization. Spectra were extracted from different locations labeled in the survey images shown as insets. EDXS spectra recorded from location 2 in Figure 4.9(a) and location 3 in Figure 4.9(b) confirm NiO composition of the directionally grown nanostructure. The spherical nanoparticle at the tip of the nanostructure in Figure 4.9(b) is comprised of Au and Cu. Nanostructures without any metal nanoparticles have revealed no traces of Au or Cu.

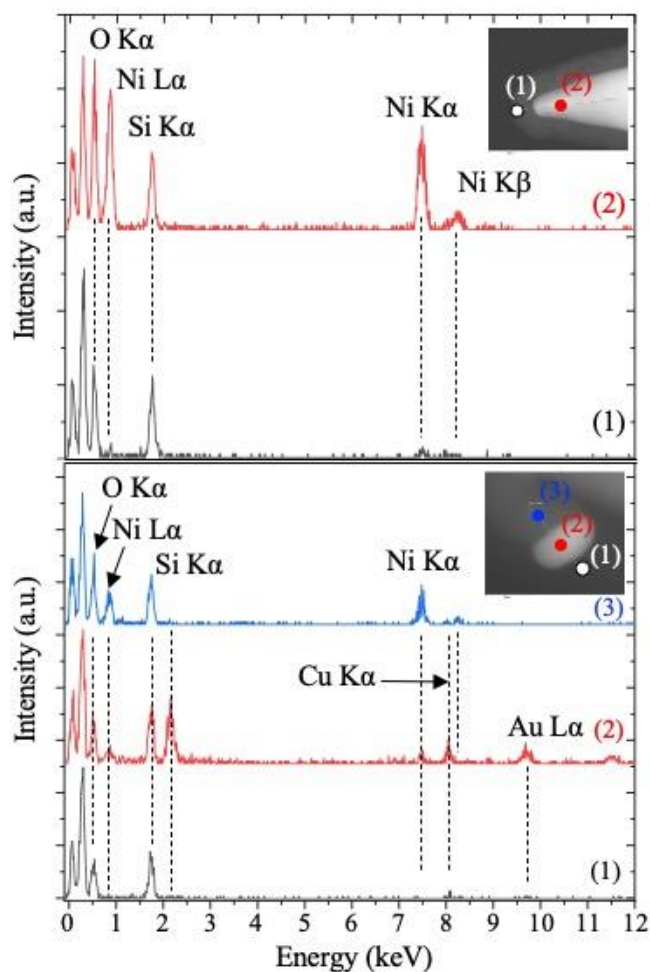


Figure 4.9 EDXS spectra extracted from line profiles during STEM characterization. Spectra were extracted from nanorods that did not (a) and did (b) exhibit a nanoparticle on their tip. Spectra were plotted for locations ahead of the tip of each nanorod (locations marked (1)), the nanoparticle (location (2) in b)) and the nanorod (locations (2) and (3) in a) and b), respectively).

Figure 4.10 (a) shows a TEM micrograph recorded from Ni nanoparticles after 5 min of ESEM heating at 800 °C in 350 Pa of water vapor atmosphere. The particles reveal faceting, and protrusions on one facet of each particle. HRTEM imaging of the area marked in Figure 4.10(a) reveals crystallinity of the protrusion as well as the polycrystalline morphology of a continuous 2-3 nm thick nickel oxide passivation layer surrounding the original metal nanoparticle. The

nickel oxide surface layer outlined by yellow dashed lines shows grain sizes ranging between 5 and 10 nm with selected grain boundary locations encircled. Fast Fourier filtering (FFT) of the HRTEM image indicates lattice spacings consistent with those for both Ni and NiO. The nanostructure protrusion (marked by green dash lines) partly overlaps with the outline of the original Ni nanoparticle and reproduces (200) lattice spacings for NiO.

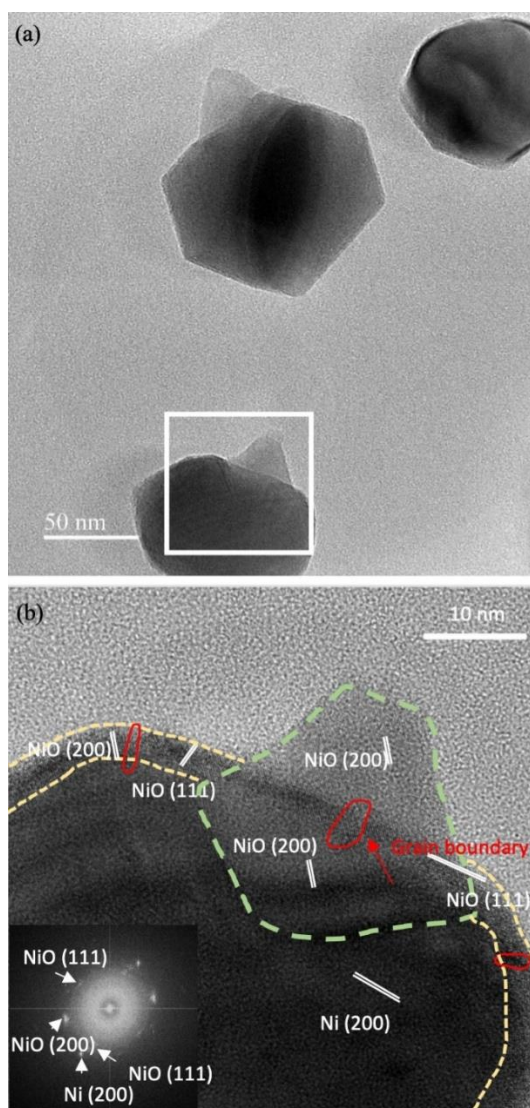


Figure 4.10 (a) Low magnification TEM image of particles after 5 min ESEM heating at 800°C at water vapor pressure of 350 Pa. (b) HRTEM image of the

particle enclosed in the white box from (a); inset is the FFT of the HRTEM image; Polycrystalline NiO surface layer is outlined in yellow dashed line and the NiO nanostructure protrusion is outlined in green dashed line.

4.4 Discussion

In-situ ESEM heating of Ni nanoparticles has revealed the directional growth of nanostructures classified either as high aspect ratio nanorods (cf. Figures 4.2b and 2d) or particle elongation (cf. Figure 4.4(f) and 4(g)). EDXS characterization of the Ni particles prior to either ESEM heating or pre-annealing has revealed a composition of roughly 95 at% of Ni and 5 at% of oxygen. This observation alongside the TEM results presented in Figure 4.10 is consistent with previous electron energy-loss spectroscopy experiments that have demonstrated that Ni particles are covered by poly-crystalline native nickel oxide layers with thicknesses around 2-3 nm⁶. After ESEM heating, EDXS and SAED experiments have confirmed growing nanostructures with near stoichiometric NiO composition. Utilizing different gas atmospheres during ESEM heating has demonstrated the growth of NiO nanostructures in the presence of water vapor, while no comparable growth was observed either in dry air or dry nitrogen environments. The contribution of molecular oxygen (O₂) is thus considered negligible for the observed nanostructure growth.

With the native nickel oxide surface layer, the continuous oxidation of Ni and growth of NiO in the presence of water vapor is initiated by dissociation of H₂O and subsequent adsorption on nickel oxide surfaces. The dissociation of water on NiO has been documented in detail in the literature^{31, 32}. The dissociative adsorption of water can be described by the following reactions³².





Hydroxyl groups serve as oxidant species for nickel. An additional source for oxidant molecules includes the radiolysis of water by electron beam irradiation. In this study, however, ESEM heating experiments carried out with the electron beam switched off resulted in the same directional growth of NiO nanostructures, hence excluding radiolysis as a dominant mechanism.

The adsorption of hydrogen described in reaction equation (4.4) promotes further oxidation of Ni based on enhanced Ni cation diffusion as a result of a proton hopping mechanisms proposed by Norby and co-workers²⁸.

ESEM and TEM characterization has revealed particle elongation and growth of high aspect ratio nanostructures from more than 95% of observed particles. Growth occurred in different directions (cf. Figures 4.8) while each particle exhibits growth of no more than 1-2 individual nanostructures. From these observations it is concluded that growth of NiO nanostructures is anisotropic, which is consistent with several previous studies that have demonstrated water adsorption as a function of crystallographic orientation of available nickel oxide surfaces³²⁻³⁴. Koga and colleagues⁸ have reported the formation of NiO nanorods only after rapid introduction of O₂ into a specialized high temperature furnace. This study, however, reveals dissociative adsorption of hydroxyl groups during in-situ heating which causes continuous anisotropic NiO growth. Luo and co-workers propose that mechanical stress at the Ni/NiO interface affects oxidation rates in water²⁴, which supports the observation of NiO growth only on select surfaces of the utilized Ni nanoparticles.

The following discussion of nucleation and anisotropic growth of NiO nanostructures requires the consideration of thermodynamic and kinetic viewpoints.

Thermodynamic viewpoint:

Anisotropy of the surface energies for both Ni and NiO causes variations of adsorption and oxidation reaction rates, which accounts for the localized directional growth of NiO nanostructures on round particles. The local free energy change ΔG for nanostructure growth accommodated by oxidation is given by ³⁵:

$$\Delta G = \Delta G_1 + \Delta G_2 \quad (4.5)$$

ΔG_1 is the free energy change related to the oxidation reaction, and $\Delta G_2 = \gamma dA$ represents the change in surface energy γ due to the change in particle surface dA . The Gibbs Free Energy for the oxidation reaction is described by

$$\Delta G_1 = \Delta G_0 + RT \ln K_p = \Delta G_0 + RT \ln \left(\frac{p_{(H_2)} p_{(O^{2-})}}{p_{(OH)}} \right). \quad (4.6)$$

K_p represents the reaction constant, $p_{(H_2)}$ and $p_{(OH)}$ are the partial pressures of H_2 and hydroxyl groups, respectively. The local free energy change ΔG is affected by both the surface energy anisotropy and hydroxyl group partial pressure. When the balance of the two reach a reduction in the local free energy, growth of NiO occurs. During the growth, $\Delta G_2 = \gamma dA$ changes with the continuous increase of surface area. From this thermodynamic viewpoint growth is expected to initiate in specific areas where NiO growth can lower the local surface energy due to, for instance, local surface curvature, or the presence of local defect structures, including impurities or the attachment of smaller particles. The HRTEM image in Figure 4.10 shows a NiO protrusion with a roughly 40nm wide contact area with the underlying Ni nanoparticle. Other nanostructures (see Figure 4.4) reveal widths ranging between 50nm and 500nm depending on

the exposed area with sufficiently high local surface energy. Growth is expected to terminate when increase of the total surface area of both Ni particle and NiO nanostructure is no longer energetically favorable.

Meltzman et al.³⁶ have recently documented the formation of equilibrium crystal shapes, i.e., minimization of total surface energy of nickel islands on sapphire substrates by high vacuum annealing at 1300°C. Similarly, the pre-annealing of sample groups B, C, and D summarized in Table 3 has lowered the total surface energy of the native oxide covered Ni nanoparticles and has thus affected NiO nanostructure growth. During ESEM heating nanostructure growth was observed after pre-annealing (sample groups B) only if no high-purity Ar gas was flown over the nanoparticles prior to evacuating the furnace tube (cf. Table 3). For sample group B the oxygen partial pressure p_{O_2} during pre-annealing at nominally 800°C is estimated to be around 10^{-3} Pa, for which the Ellingham diagram³⁷ does not predict reduction of native nickel oxide. Flowing high purity argon gas through the tube furnace prior to its evacuation allowed for displacement of molecular oxygen and caused further reduction of p_{O_2} during the subsequent pre-annealing process of sample groups C and D. Under similar conditions Matsuno and co-workers⁶ have observed the onset of native nickel oxide reduction. It is therefore concluded that the partial reduction the native nickel oxide layer during pre-annealing allows for the reconfiguration of the free nickel particle surfaces to lower the total energy and, hence, suppress NiO nanostructure growth during subsequent ESEM heating experiments. The formation of facets observed from as-annealed particles shown in Figure 4.6 serves as experimental evidence for the surface reconfiguration. The presence of the nickel oxide layer on the particles' surfaces (cf. sample group B), on the other hand, obstructs the free rearrangement of nickel towards a lower energy configuration.

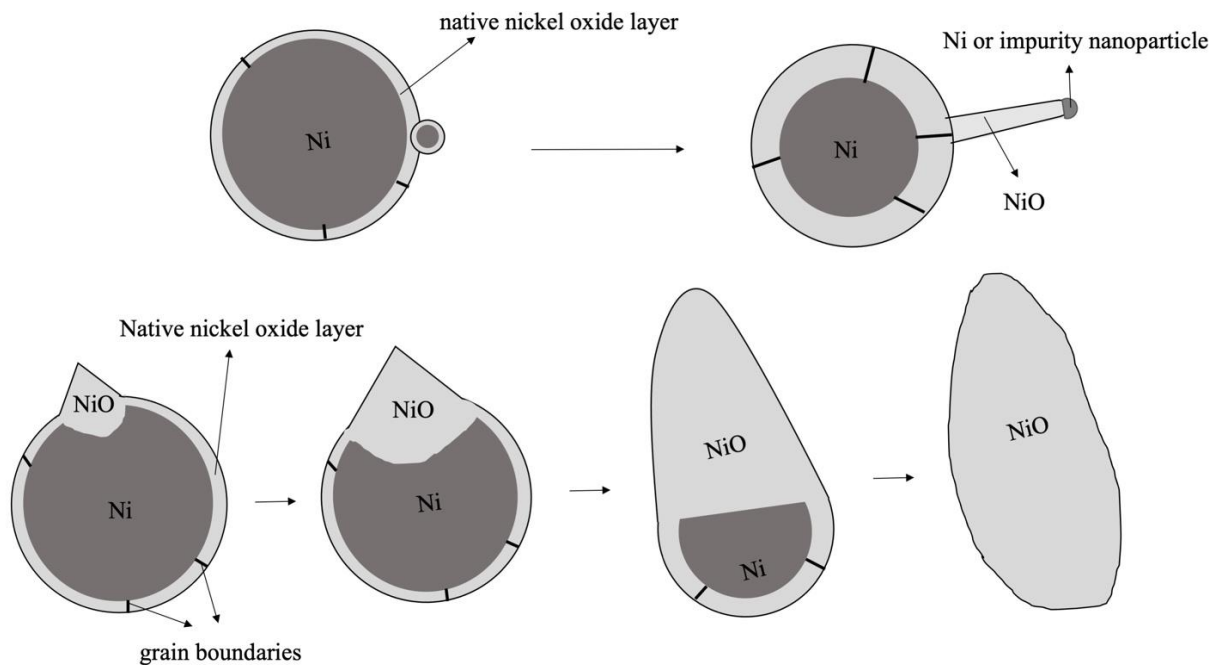


Figure 4.11 Sketches of high aspect ratio NiO growth and particle elongation. In both cases growth initiated from areas of relatively high surface energy density. The extent of the areas determines the width of the growing nanostructure. Growth occurs at Ni/NiO interfaces, and can occur between adjacent Ni particles.

Kinetic viewpoint:

The growth of oxide nanostructures during ESEM heating requires outward diffusion of nickel cations from the metal nanoparticles and a supply of hydroxyl groups through adsorption from the gas phase. At 800°C the diffusion coefficients for Ni in NiO are 10x to 100x larger than those for oxygen¹¹, which would cause the formation of voids inside the oxide-covered nickel nanoparticles^{7, 38, 39}. However, in this study no voids or signs of locally reduced effective density of the particles were detected by SEM or HAADF-STEM imaging. Protrusions observed by TEM (see Figure 4.10) represent the onset of NiO nanostructure growth during ESEM heating. Part of the NiO protrusion extend into the volume of the original Ni particle, which indicates

inward diffusion of hydroxyl groups. It is concluded that particle elongation and especially growth of NiO nanorods with high aspect ratio occur at the Ni/NiO interface rather than the NiO surface. Figure 4.11 shows a sketch of the proposed growth mechanisms. As mentioned above, particle elongation is initiated by the formation of local NiO protrusions that form at the surface of the native oxide-covered Ni nanoparticles. Hydroxyl ion diffusion through the NiO protrusions facilitates continuous oxidation until metallic Ni is consumed. In contrast, high aspect ratio growth is initiated from smaller areas characterized by relatively large local surface area. Such sites can include surface defects or areas where smaller nanoparticles of Ni or other impurities such as Au are attached. In the case of attached nanoparticles, growth proceeds at the Ni/NiO interface and is experimentally observed between the respective particles (cf. Figure 4.4f and Figure 4.8a).

4.5 Conclusions:

In-situ heating of nickel nanoparticles at 800°C in water vapor atmosphere inside an ESEM instrument was found to cause the one directional growth of NiO nanostructures. Hydroxyl groups from water dissociative adsorption were found to serve as oxidant molecules. Nanostructures grow at locations with sufficiently high local surface energy that is effectively lowered by the observed nanostructure growth. The proposed growth model is verified by the observation that no growth takes place on particles that were previously annealed under low oxygen partial pressures to obtain lower energy surface configurations prior to in-situ annealing in water vapor. It is concluded that the manipulation of surface energy prior to heating in water vapor provides an avenue to prevent the growth of oxide nanostructures or control their growth by adjusting oxygen partial pressure. Control over surface configurations of nanoparticles is

critical to ensure, for instance, the ability to sinter of powder compacts during ceramic processing.

Acknowledgement: The authors gratefully acknowledge funding from the Army Research Office under award W911NF1610364 (program manager: Dr. Michael Bakas) and the National Science Foundation under award DMR-1836571. The ESEM instrument was acquired with NSF-MRI award DMR-1725618. Discussions with James Ranney (ThermoFisher Scientific), Dr. Andrew Thron (Advanced Materials Characterization Laboratory, UC Davis) and Dr. Daria Eiteneer (Folsom Lake College) are greatly appreciated.

Statement of Contributions: KvB has conceived the study, while BQ has carried out all experiments, and subsequent data analysis. Both authors have contributed equally writing the manuscript.

4.6 References:

1. Rice DW, Phipps PBP, Tremoureux R. Atmospheric Corrosion of Nickel. *J Electrochem Soc.* 1980;127(3):563. <https://doi.org/10.1149/1.2129712>
2. Haugsrud R. On the high-temperature oxidation of nickel. *Corrosion Science.* 2003;45(1):211–235. [https://doi.org/10.1016/S0010-938X\(02\)00085-9](https://doi.org/10.1016/S0010-938X(02)00085-9)
3. Mrowec S, Grzesik Z. Oxidation of nickel and transport properties of nickel oxide. *Journal of Physics and Chemistry of Solids.* 2004;65(10):1651–1657. <https://doi.org/10.1016/j.jpcs.2004.03.011>
4. Karmhag R, Tesfamichael T, Wäckelgård E, Niklasson GA, Nygren M. Oxidation Kinetics of Nickel Particles: Comparison Between Free Particles and Particles in an Oxide Matrix. *Solar Energy.* 2000;68(4):329–333. [https://doi.org/10.1016/S0038-092X\(00\)00025-6](https://doi.org/10.1016/S0038-092X(00)00025-6)

5. Song P, Wen D, X. Guo Z, Korakianitis T. Oxidation investigation of nickel nanoparticles. *Physical Chemistry Chemical Physics*. 2008;10(33):5057–5065. <https://doi.org/10.1039/B800672E>
6. Matsuno M, Bonifacio CS, Rufner JF, *et al.* In situ transmission electron microscopic investigations of reduction-oxidation reactions during densification of nickel nanoparticles. *Journal of Materials Research*. 2012;27(18):2431–2440. <https://doi.org/10.1557/jmr.2012.256>
7. Railsback JG, Johnston-Peck AC, Wang J, Tracy JB. Size-Dependent Nanoscale Kirkendall Effect During the Oxidation of Nickel Nanoparticles. *ACS Nano*. 2010;4(4):1913–1920. <https://doi.org/10.1021/nn901736y>
8. Koga K, Hirasawa M. Anisotropic growth of NiO nanorods from Ni nanoparticles by rapid thermal oxidation. *Nanotechnology*. 2013;24(37):375602. <https://doi.org/10.1088/0957-4484/24/37/375602>
9. Munir ZA. Analytical treatment of the role of surface oxide layers in the sintering of metals. *J Mater Sci*. 1979;14(11):2733–2740. <https://doi.org/10.1007/BF00610647>
10. Bonifacio C, Holland T, van Benthem K. Time-dependent dielectric breakdown of surface oxides during electric-field-assisted sintering. *Acta Materialia*. 2014;63:140–149. <https://doi.org/10.1016/j.actamat.2013.10.018>
11. Chevalier S, Desserrey F, Larpin JP. Oxygen Transport during the High Temperature Oxidation of Pure Nickel. *Oxid Met*. 2005;64(3):219–234. <https://doi.org/10.1007/s11085-005-6560-x>
12. Gibbs JW. On the Equilibrium of Heterogeneous Substances. 1879 <https://doi.org/10.11588/heidok.00013220>
13. Koga K, Hirasawa M. Gas-phase generation of noble metal-tipped NiO nanorods by rapid thermal oxidation. *Mater Res Express*. 2014;1(4):045021. <https://doi.org/10.1088/2053-1591/1/4/045021>
14. Galerie A, Wouters Y, Caillet M. The kinetic behaviour of metals in water vapour at high temperatures: can general rules be proposed? *Materials Science Forum*. 2001;369–372.
15. Raynaud GM, Rapp RA. In situ observation of whiskers, pyramids and pits during the high-temperature oxidation of metals. *Oxid Met*. 1984;21(1):89–102. <https://doi.org/10.1007/BF00659470>
16. Hänsel M, Quadackers WJ, Young DJ. Role of Water Vapor in Chromia-Scale Growth at Low Oxygen Partial Pressure. *Oxidation of Metals*. 2003;59(3):285–301. <https://doi.org/10.1023/A:1023040010859>

17. Bertrand N, Desgranges C, Poquillon D, Lafont MC, Monceau D. Iron Oxidation at Low Temperature (260–500 °C) in Air and the Effect of Water Vapor. *Oxid Met.* 2010;73(1):139–162. <https://doi.org/10.1007/s11085-009-9171-0>
18. Payne BP, Biesinger MC, McIntyre NS. The study of polycrystalline nickel metal oxidation by water vapour. *Journal of Electron Spectroscopy and Related Phenomena.* 2009;175(1):55–65. <https://doi.org/10.1016/j.elspec.2009.07.006>
19. Pieraggi B, Rolland C, Bruckel P. Morphological characteristics of oxide scales grown on H11 steel oxidised in dry or wet air. *Materials at High Temperatures.* 2005;22(1–2):61–68. <https://doi.org/10.1179/mht.2005.007>
20. Saunders SRJ, Monteiro M, Rizzo F. The oxidation behaviour of metals and alloys at high temperatures in atmospheres containing water vapour: A review. *Progress in Materials Science.* 2008;53(5):775–837. <https://doi.org/10.1016/j.pmatsci.2007.11.001>
21. Rahmel A. Einfluss von wasserdampf und kohlendioxid auf die oxydation von nickel in sauerstoff bei hohen temperaturen. *Corrosion Science.* 1965;5(12):815–820. [https://doi.org/10.1016/S0010-938X\(65\)80011-7](https://doi.org/10.1016/S0010-938X(65)80011-7)
22. Tollman RL, Gulbransen EA. Crystal Morphology and Mechanisms of Growth of Alpha-Fe₂O₃ Whiskers on Iron. *J Electrochem Soc.* 1967;114(12):1227. <https://doi.org/10.1149/1.2426455>
23. Wang S, Dong Z, Zhang L, Tsiakaras P, Shen PK, Luo L. Atomic Scale Mechanisms of Multimode Oxide Growth on Nickel–Chromium Alloy: Direct In Situ Observation of the Initial Oxide Nucleation and Growth. *ACS Appl Mater Interfaces.* 2021;13(1):1903–1913. <https://doi.org/10.1021/acsami.0c18158>
24. Luo L, Li L, Schreiber DK, *et al.* Deciphering atomistic mechanisms of the gas-solid interfacial reaction during alloy oxidation. *Science Advances.* 2020;6(17):eaay8491. <https://doi.org/10.1126/sciadv.aay8491>
25. Luo L, Su M, Yan P, *et al.* Atomic origins of water-vapour-promoted alloy oxidation. *Nature Materials.* 2018;17(6):514–518. <https://doi.org/10.1038/s41563-018-0078-5>
26. Hayashi S, Narita S, Narita T. Oxidation Behavior of Ni-3, 6 wt% Al Alloys at 800 °C in Atmospheres Containing Water Vapor. *Oxid Met.* 2010;74(1):33–47. <https://doi.org/10.1007/s11085-010-9196-4>
27. Wang Z, Takeda Y. Roles of permeated hydrogen in the oxidation process of Ni-based alloy in high temperature water environment. *Corrosion Science.* 2021;179:109139. <https://doi.org/10.1016/j.corsci.2020.109139>

28. Norby T. Protonic defects in oxides and their possible role in high temperature oxidation. *J Phys IV France*. 1993;03(C9):C9-99-C9-106. <https://doi.org/10.1051/jp4:1993907>
29. Schneider CA, Rasband WS, Eliceiri KW. NIH Image to ImageJ: 25 years of image analysis. *Nat Methods*. 2012;9(7):671–675. <https://doi.org/10.1038/nmeth.2089>
30. Thevenaz P, Ruttimann UE, Unser M. A pyramid approach to subpixel registration based on intensity. *IEEE Transactions on Image Processing*. 1998;7(1):27–41. <https://doi.org/10.1109/83.650848>
31. McKay JM, Henrich VE. Surface electronic structure of NiO: Defect states, O₂ and H₂O interactions. *Phys Rev B*. 1985;32(10):6764–6772. <https://doi.org/10.1103/PhysRevB.32.6764>
32. Zhao W, Bajdich M, Carey S, Vojvodic A, Nørskov JK, Campbell CT. Water Dissociative Adsorption on NiO(111): Energetics and Structure of the Hydroxylated Surface. *ACS Catal*. 2016;6(11):7377–7384. <https://doi.org/10.1021/acscatal.6b01997>
33. Cappus D, Xu C, Ehrlich D, *et al.* Hydroxyl groups on oxide surfaces: NiO(100), NiO(111) and Cr₂O₃(111). *Chemical Physics*. 1993;177(2):533–546. [https://doi.org/10.1016/0301-0104\(93\)80031-4](https://doi.org/10.1016/0301-0104(93)80031-4)
34. Kitakatsu N, Maurice V, Hinnen C, Marcus P. Surface hydroxylation and local structure of NiO thin films formed on Ni(111). *Surface Science*. 1998;407(1):36–58. [https://doi.org/10.1016/S0039-6028\(98\)00089-2](https://doi.org/10.1016/S0039-6028(98)00089-2)
35. Zhang J-S, editor. 25 - Environmental Damage at High Temperature. *High Temperature Deformation and Fracture of Materials*. Woodhead Publishing; 2010:330–348. <https://doi.org/10.1533/9780857090805.2.330>
36. Meltzman H, Chatain D, Avizemer D, Besmann TM, Kaplan WD. The equilibrium crystal shape of nickel. *Acta Materialia*. 2011;59(9):3473–3483. <https://doi.org/10.1016/j.actamat.2011.02.021>
37. Gaskell DR, Laughlin DE. Introduction to the Thermodynamics of Materials, Sixth Edition. CRC Press; 2017
38. Nakamura R, Lee J-G, Mori H, Nakajima H. Oxidation behaviour of Ni nanoparticles and formation process of hollow NiO. *Philosophical Magazine*. 2008;88(2):257–264. <https://doi.org/10.1080/14786430701819203>
39. Nakamura R, Matsubayashi G, Tsuchiya H, Fujimoto S, Nakajima H. Formation of oxide nanotubes via oxidation of Fe, Cu and Ni nanowires and their structural stability: Difference in formation and shrinkage behavior of interior pores. *Acta Materialia*. 2009;57(17):5046–5052. <https://doi.org/10.1016/j.actamat.2009.07.00>

Chapter 5: In-situ anisotropic growth of nickel oxide nanostructures through layer-by-layer metal oxidation¹

This study reports the one-directional growth of single crystalline nickel oxide nanostructures that is facilitated by the oxidation of nickel nanoparticles. Layer-by-layer growth at the buried NiO/Ni interface was directly observed by in-situ high resolution transmission electron microscopy at 650°C in an oxygen partial pressure around 4×10^{-4} Pa. Individual layers of NiO grow by ledge movement, i.e., disconnection migration along the oxide/metal interface plane. Oxidation at interfacial steps is governed by oxygen vacancy migration along the interface plane, while the junction between the oxide/metal interface and the gas phase serves as nucleation site. The results of this study demonstrate the applicability of the terrace-ledge-kink crystal growth model for reactive crystal growth processes at internal heterophase interfaces.

One-dimensional nanostructures such as nanotubes, nanowires, and nanorods hold promise for a variety of applications owing to their exciting physical properties that can be considerably different compared to their bulk counterparts¹⁻⁵. For their synthesis directional crystal growth strategies are reported⁶⁻¹⁰ and include vapor-liquid-solid (VLS)⁶, solution-liquid-solid (SLS)⁷, and vapor-solid-solid (VSS)⁸ mechanisms. These techniques leverage catalyst particles that serve as solvent and promote crystal growth by re-precipitation of the solute at the catalyst/nanostructure interface. The morphology and size of resulting nanostructures typically

¹ Published as B. Qu, K. van Benthem, *Scripta Materialia* **214** (2022) 114660.

depend on the size of the catalyst particles ¹¹. However, controlling the growth process and management of dopant distributions however remains challenging during catalytic chemical vapor deposition. For instance, Oh and co-workers observed unwanted supersaturation of Au point defects in VLS grown silicon nanowires ¹². Kossel ¹³ and Stranski ¹⁴ originally introduced the terrace ledge-kink (TLK) model as a thermodynamic description of surface transformations during crystal growth. For VLS growth Hofmann and co-workers have subsequently demonstrated ledge propagation at the Pd silicide/Si interface during Si nanowire growth in disilane atmosphere ¹⁵. Ledge movement occurs by re-precipitation of Si from the silicide phase. The Burton-Cabrera-Frank screw dislocation growth model ^{9, 10} utilizes the TLK formalism to describe crystal growth under low supersaturation. Self-perpetuating steps are formed from screw dislocation intersecting with the free surface ^{9, 10}. The model was experimentally confirmed by a series of nanowire growth studies for different materials systems ¹⁶⁻¹⁸. For metal oxide growth, adatoms from the gas phase are attached to step edges while screw dislocations within the growing nanostructure or oxide scale provide diffusion pathways for reactants ^{19, 20}.

Gleiter ²¹ adopted the terrace ledge kink mechanism to describe grain boundary migration during the recrystallization of Al-Cu alloys. Atoms are emitted from steps on the shrinking grain and added to the growing grain. Several authors have subsequently utilized the concept of disconnections, i.e., defects at grain boundaries with step and dislocation character ²² to describe grain boundary kinetics in oxide ceramics ²³⁻²⁷. Zou et al. documented step movement during solid state reactions at curved metal/oxide interfaces ²⁸. However, interface curvature may have represented an additional driving force for interface migration ²⁸. This study provides direct evidence for reactive layer-by-layer growth of nickel oxide at a buried and atomically flat Ni/NiO interface. While anisotropic growth of nickel oxide nanostructures in water vapor was

recently observed during in-situ environmental scanning electron microscopy ²⁹, in-situ TEM experiments reported in the following demonstrate that the TLK model is also applicable to reactive crystal growth, including internal oxidation and oxide scale growth.

Anisotropic growth of NiO nanorods was carried out by in-situ heating of nickel nanoparticles (SkySpring Nanomaterials, Inc.) in an environmental scanning electron microscope (ESEM). Nanoparticles with a nominal diameter of 300 nm were dispersed in isopropanol and drop-casted either onto thermally grown SiO₂ films supported by a silicon substrate, or a PELCO[®] Silicon Dioxide Support Film for TEM with a 18nm thick SiO₂ membrane (Ted Pella, Inc.). ESEM heating was performed with a ThermoFisher Quattro Environmental Scanning Electron Microscope (Thermo Fisher Scientific, Hillsboro, OR) under water vapor with base pressures ranging between 250 Pa and 400 Pa. Nickel nanoparticles were heated to 800 °C at a rate of 30-50 °C/min. The temperature was held at 800 °C for up to 45 minutes until no more morphological changes of the nickel nanoparticle agglomerates were detected. After ESEM heating bright field scanning transmission electron microscopy (STEM) imaging was carried out with a JEOL JEM 2100AC aberration corrected scanning transmission electron microscope. Energy dispersive X-ray spectroscopy (EDXS) line profiles were acquired with an Oxford Aztec Energy TEM Advanced Microanalysis System with an X-MaxN TSR Windowless large area Analytical Silicon Drift Detector.

Figure 5.1(a) reproduces earlier results of anisotropic growth of NiO nanostructures with a variety of different aspect ratios during ESEM heating at 800°C under 400 Pa of water vapor atmosphere ²⁹. Subsequent bright field STEM and conventional TEM imaging of as-grown high aspect ratio nanostructures reveal the absence (Figure 5.1(b)) or presence (Figure 5.1(c)) of metal nanoparticles at their tip. EDXS analysis (see Figure 5.1(d)) identified nanoparticle compositions

as either pure Ni or Au-rich solid solutions of Cu and Au, which are impurities within the raw powder and were discussed previously²⁹ Similar matchstick-like morphologies of NiO nanostructures were previously documented by Koga and Hirasawa³⁰ after rapid oxidation of Ni-Au alloy nanoparticles above 600°C. The presence of Au-Cu nanoparticles at the tips of some NiO nanorods formed during ESEM heating is consistent with previously observed catalytic growth behavior^{31, 32}. However, many NiO nanostructures observed in this study revealed either residual Ni particles (see (1) in Figure 5.1(c)) or no particles (Figure 5.1(b), which suggests an additional growth mechanism.

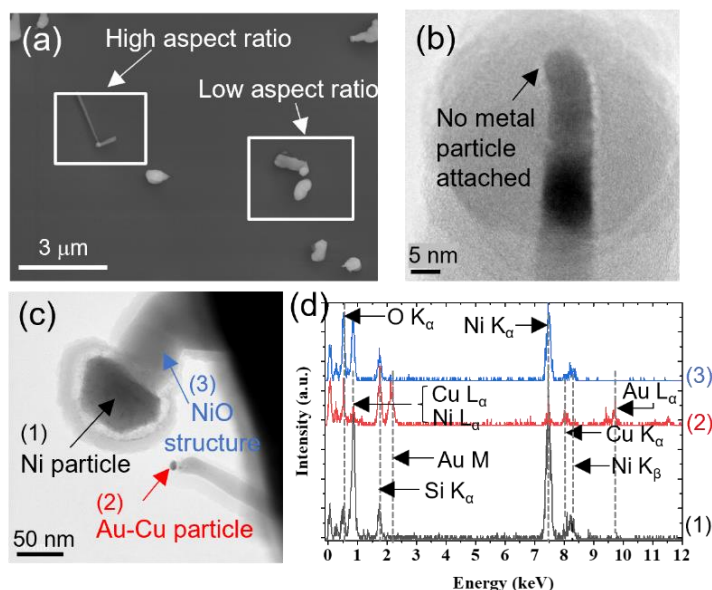


Figure 5.1 (a) SEM micrograph of nickel particles after ESEM heating at 800°C in 400 Pa of water vapor. Elongated nanostructures with different aspect ratios are observed. (b) & (c) STEM bright field images of three different nanostructures displaying the absence or presence of metal nanoparticles at their tips, respectively. (d) EDXS spectra recorded from metal nanoparticles labeled (1) and (2) in (c).

To interrogate atomic-scale growth mechanisms, in-situ high resolution transmission electron microscopy (HRTEM) heating experiments under simultaneous gas flow were carried out with a

gas injection/specimen heating holder³³ inserted into a Hitachi HF-9500 transmission electron microscope operated at 300 kV. For these experiments Ni nanoparticles formed by dewetting of previously deposited Ni thin films were deposited directly onto the tungsten heating wire of the in-situ sample holder. HRTEM images were recorded as video files while the tungsten wire was resistively heated to 650 °C. Dry laboratory air was directed onto the TEM sample using a gas injection nozzle. During in-situ imaging the base pressure in the sample area was roughly 2×10^{-3} Pa. Figure 5.2 shows a series of HRTEM micrographs extracted from a video recorded during the nanostructure growth process (see supplemental materials). After initial onset of NiO growth (see Figure 5.2(a) and (b)) the NiO/Ni interface becomes mostly flat for the remainder of the nanostructure growth. Dashed lines mark the interface between the growing NiO nanostructure and the shrinking Ni nanoparticle. Throughout nanostructure growth lattice fringe contrast is observed from NiO and Ni indicating that both phases have remained solid and crystalline. The ratio of interplanar lattice spacings observed from the NiO nanorod and the Ni nanoparticle (cf. Figure 5.2(f)) is 1.2 ± 0.1 , which is consistent with the lattice constant ratio of 1.18 between NiO and Ni.

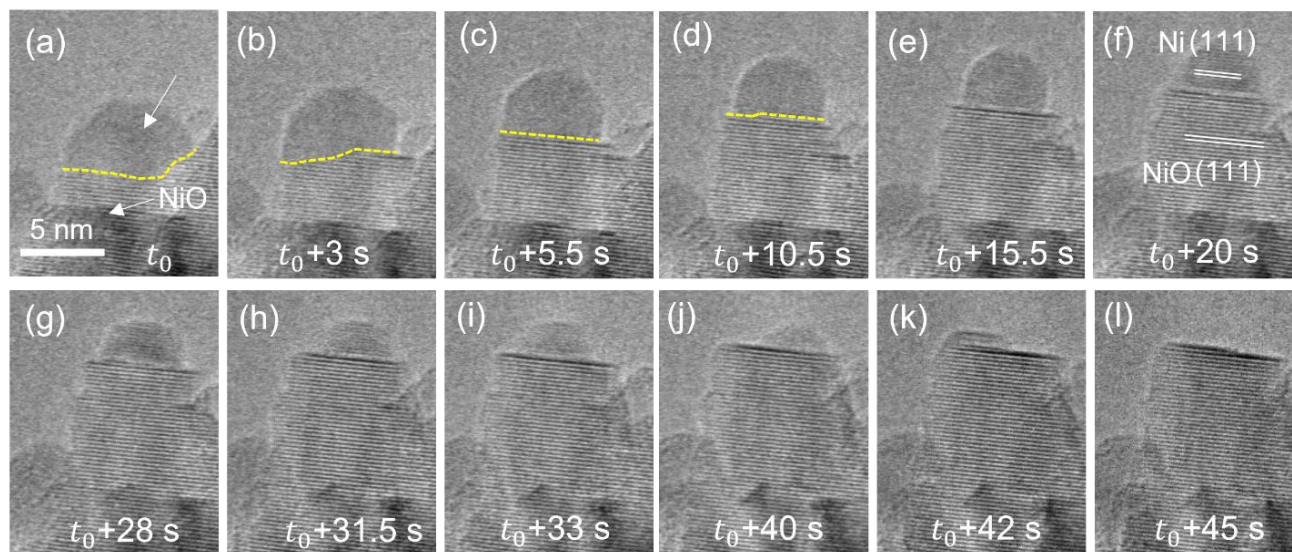


Figure 5.2 HRTEM micrographs extracted from an in-situ video recorded at 650 °C and a base pressure around 10^{-3} Pa. The NiO/Ni interface is marked by yellow dashed lines in (a)-(d). Time stamps are provided for each individual image. A single-crystalline NiO nanostructure grows in the vertical direction while the crystalline nickel nanoparticle changes shape and reduces in size until fully consumed at t_0+45 s.

The change of the Gibbs free energy for oxide formation ³⁴ suggests oxidation of metallic nickel under the in-situ TEM experimental conditions of 650 °C and an oxygen partial pressure around 4×10^{-4} Pa. Consistent with previous observations of anisotropic growth of NiO nanostructures (cf. Figure 5.1 and ²⁹), Figure 5.2 therefore reveals that oxidation of Ni proceeds at the metal/oxide interface through layer-by-layer growth of NiO. The Ni nanoparticle shrinks (Figure 5.2(a)-(k)) by the subsequent removal of lattice planes until it is fully consumed by the reactive growth process (cf. Figure 5.2(l)) and NiO growth terminates. Figure 5.3 shows the appearance and subsequent disappearance of individual steps at the NiO/Ni interface at different times. Lattice planes grow by the movement of individual steps along the interface plane. Examples are highlighted by arrows in Figure 5.3 (a), (c), (e) and (g). New NiO lattice planes emerge from the side of the growing nanostructure, i.e., the NiO/Ni/gas phase junction. Similar to VLS growth of Si nanowires ³⁵ these triple junctions serve as nucleation sites for NiO layer growth.

Unexpectedly, the diameter of the growing nanorod remains unchanged during the continuous shrinkage of the Ni nanoparticle (Figure 5.2(f)-(k)). From this observation it is concluded that it is energetically more favorable for NiO to grow layer-by-layer instead of following a Stranski-Krastanov growth mode ¹⁴. The movement of the metal nanoparticle on the oxide surface (Figure 5.2(g-k)) is likely a result of Ni surface diffusion during NiO growth, while the associated vacancy mechanism within the metal nanoparticle causes particle deformation and thus migration to continuously minimize free surface and interface energies. At the same time the Ni

nanoparticle also changes its shape as a result of balancing its total surface energy with the NiO/Ni interface energy.

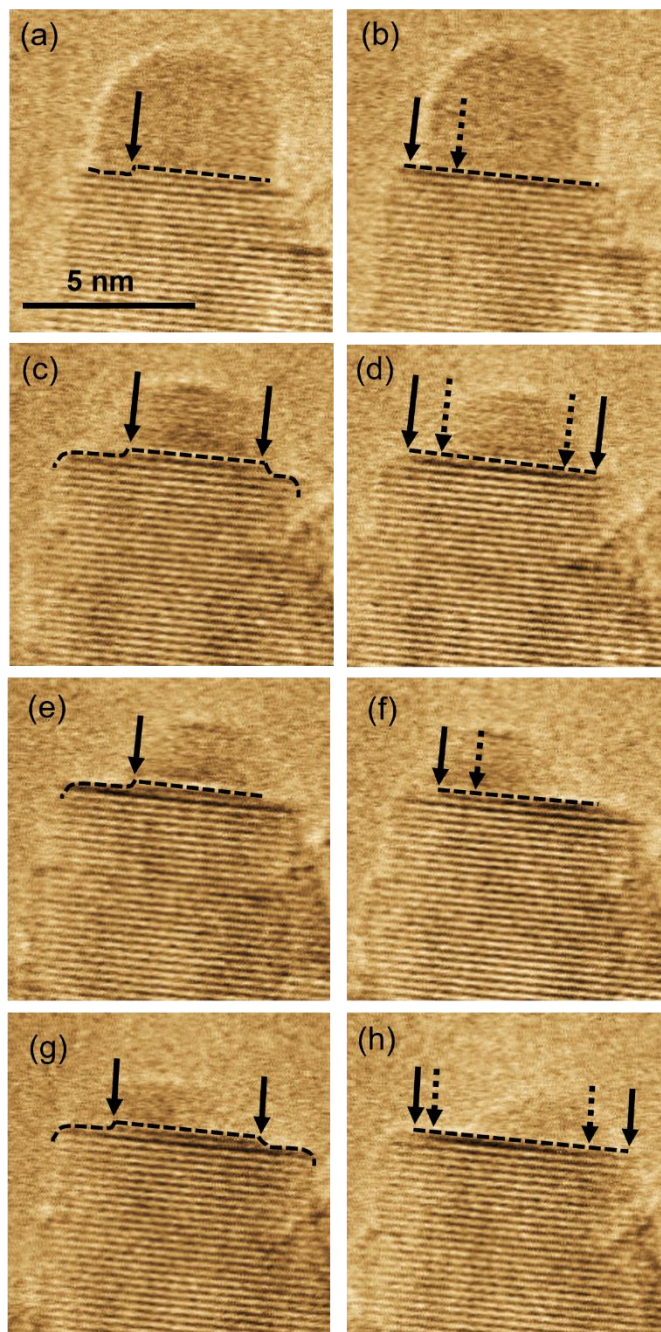


Figure 5.3 HRTEM images extracted from an in-situ video recorded at 650°C under 2×10^{-3} Pa of air. The images were rotated and intensities were color-coded for better

presentation. Adjacent images (a&b, c&d, e&f, and g&h) represent subsequent video frames. The NiO/Ni interface is marked by the dashed lines. Steps at the interface are highlighted by arrows. The dashed arrows in (b) (d) (e) and (f) marks the step location in (a) (c) (f) and (g), respectively.

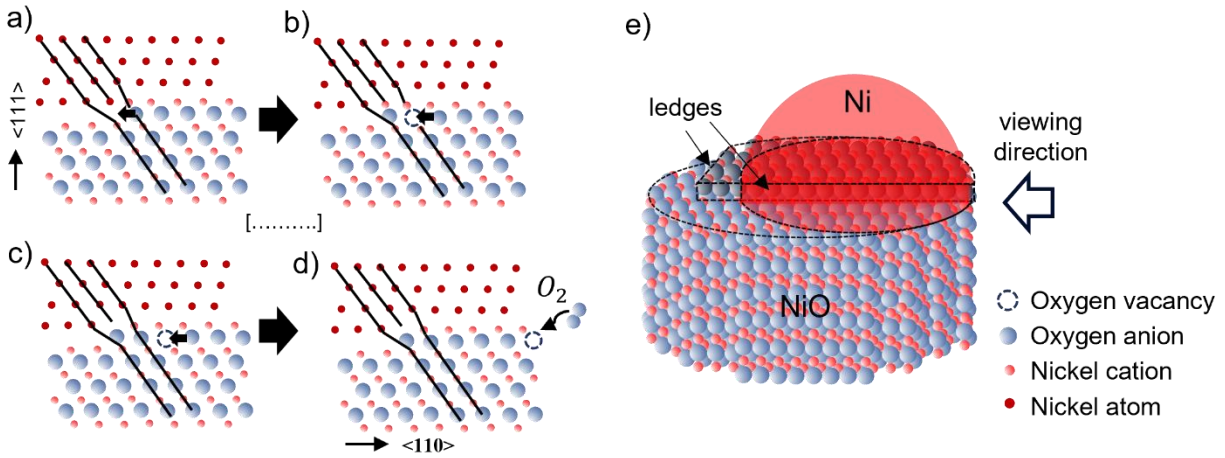


Figure 5.4 (a) 2D model of the NiO/Ni interface configuration representing the observed growth mechanism of NiO nanostructures. Misfit dislocations at the NiO/Ni interface in conjunction with steps in the interface plane represent disconnections. Ledge movement is facilitated by oxygen vacancy diffusion along the interface plane which ensures oxygen supply for continuing oxidation of Ni atoms. (e) 3D representation of the shrinking Ni particle supported by the NiO surface.

The NiO growth process observed in Figures 5.2 and 5.3 is sketched in Figure 5.4(a-d) for one possible crystal orientation with a $\{111\}$ interface plane. Figure 5.4(e) is a 3D sketch representing the matchstick-like configuration of the NiO nanorod and the Ni particle with a possible viewing direction during the HRTEM experiments indicated by the black hollow arrow. The experimental observations in Figures 5.2 and 5.3 suggest that nickel oxidation occurs at kink sites along the NiO/Ni interface. The lattice mismatch between NiO and Ni is accommodated by misfit dislocations at the NiO/Ni interface (cf. Figure 5.4(a-d)). The layer-by-layer growth through the advancement of interfacial steps in the presence of misfit dislocations allows for the

consideration of interface disconnections that facilitate the observed growth of NiO at the cost of the shrinking Ni nanoparticle. This description is phenomenologically similar to the concept of mobile disconnections for the migration of grain boundaries in ceramics^{22, 24-27}. To advance a disconnection an interfacial nickel atom that is considered part of the metal nanoparticle bonds to an oxygen anion of the NiO surface (Figure 5.4(a)). At 650°C the thermodynamic driving force for oxidation is sufficient. As a result, oxygen migrates along the interface plane which advances the kink in the $\langle 110 \rangle$ direction for a $\{111\}$ interface plane (cf. Figure 5.4(a) and 4(b)). As a result, an oxygen vacancy is created within the interfacial NiO plane which migrates along the interface (Figure 5.4(c)) towards the triple junction between the NiO/Ni interface and the gas phase (Figure 5.4(d)). This process enables oxygen anion supply from the gas phase for subsequent oxidation reactions to facilitate kink advancement. The in-situ HRTEM imaging results displayed in Figure 5.3 are consistent with such disconnection movement by anion-vacancy diffusion. Due to the 2D projection some interfacial steps may not be detected during HRTEM imaging while others may not necessarily be located at a NiO/Ni interface, but rather represent steps on the free NiO surface (cf. Figures 5.3(g) and 5.4(e)).

In bulk NiO metal cations have a higher mobility than oxygen anions³⁶. Hirth and Mitchell³⁷ have argued that during nickel oxidation interfacial oxygen remains in the same position and disconnections at the metal/oxide interface are immobile. Instead, nickel diffuses through the oxide towards the external surface where oxidation takes place^{38, 39}. In this study, however, extensive Ni diffusion is not required as oxidation takes place at the NiO/Ni interface where metallic Ni atoms are available. Instead, the oxidation process is assumed to be governed by oxygen vacancy migration along the NiO/Ni interface plane. Once the metal particle becomes smaller than the oxide crystal, step migration on the surface NiO replaces disconnection motion

at the interface and may be characterized by a different migration rate. Such change in migration rate may cause changes in crystallographic growth direction previously observed during in-situ ESEM experiments²⁹. Furthermore, once the in-plane particle radius exceeds its out-of-plane thickness, nickel oxide growth might be dominated by oxygen anion flux through the nickel particle.

Medlin and collaborators^{40, 41} have recently applied a model by Hirth and Pond²² to estimate the flux of material required for an interfacial phase transformation. For the oxidation reaction at the Ni/NiO (111) interface observed in Figure 5.3 the flux of oxygen anions J_o that is required for ledge movement is estimated by

$$J_O \left(\frac{\text{mol}}{\text{m}^2 \cdot \text{s}} \right) = \frac{I_O}{L \cdot \Delta y} = \frac{L \cdot v \cdot (h \Delta X_O + b_n X_O^{\text{Ni}})}{L \cdot \Delta y} = \frac{v \cdot (d_{\text{Ni}(111)} \Delta X_O + b_n X_O^{\text{Ni}})}{\Delta y} \quad (5.1)$$

I_O represents the current of oxygen anions; $d_{(\text{hkl})}$ is the interplanar spacing of the corresponding (hkl) planes. h represents the overlap step height of the disconnection; b_n represents the burgers vector in the direction perpendicular to the interface; X_O is the number of oxygen atoms per unit volume in a phase DX_O and is the difference between X_O^{Ni} and X_O^{NiO} ; L represents the length of the ledge; Δy represents the distance a disconnection travels and v represents the step movement velocity. A combination of equation (5.1) and Fick's First Law was used to estimate the diffusion coefficient for oxygen associated with disconnection movement. According to Fick's first law, the diffusion coefficient of oxygen is calculated to be $1.2 \times 10^{-18} \text{ m}^2/\text{s}$. This result is in excellent agreement with the effective diffusion coefficient for oxygen in NiO, i.e. $6.2 \times 10^{-18} \text{ m}^2/\text{s}$ ³⁶. The volume diffusion coefficient of oxygen in NiO is $7.7 \times 10^{-21} \text{ m}^2/\text{s}$ ³⁶, hence corroborating that NiO nanorod growth is governed by oxygen diffusion along the NiO/Ni interface.

The growth process outlined above resembles TLK growth originally proposed by Kossel¹³ and Stranski¹⁴ in which adatoms are attached at thermodynamically favorable kink sites, i.e., at steps in projection of the crystal surface. The experimental results presented in this study expand the TLK model and demonstrate its applicability for reactive crystal growth at buried solid-state heterogeneous interfaces. NiO nanorod growth by NiO/Ni interface migration is accomplished by the consumption of the Ni nanoparticle that serves as reactant for the formation of NiO as the reaction product. The thermodynamic driving force for ledge movement is rooted in the temperature and oxygen partial pressure during the in-situ growth experiments. The growth model may also represent a viable mechanism for the anisotropic growth of NiO nanostructure in water vapor²⁹. Unlike previous reports²⁸ disconnection movement is observed from atomically flat interfaces for which no curvature contributes an additional driving force for interface migration. Calculations of materials flux required for the advancement of disconnections are consistent with oxygen vacancy interface diffusion. The growth model discovered in this study demonstrates the feasibility to apply the existing TLK model to reaction-controlled migration of internal interfaces.

The authors acknowledge financial support from the National Science Foundation [DMR-1836571]. The ESEM was acquired through the NSF-MRI program [DMR-1725618]. The authors are grateful for assistance by Dr. Xiaofeng Zhang and Dr. Takeo Kamino (Hitachi High Technologies). Discussions with Dr. Douglas Medlin (Sandia National Laboratories) and Joseph Wood were invaluable.

References:

1. Lieber CM. One-dimensional nanostructures: Chemistry, physics & applications. *Solid State Communications*. 1998;107(11):607–616. [https://doi.org/10.1016/S0038-1098\(98\)00209-9](https://doi.org/10.1016/S0038-1098(98)00209-9)
2. Chen J, Wiley BJ, Xia Y. One-Dimensional Nanostructures of Metals: Large-Scale Synthesis and Some Potential Applications. *Langmuir*. 2007;23(8):4120–4129. <https://doi.org/10.1021/la063193y>
3. Wang ZL. Splendid One-Dimensional Nanostructures of Zinc Oxide: A New Nanomaterial Family for Nanotechnology. *ACS Nano*. 2008;2(10):1987–1992. <https://doi.org/10.1021/nn800631r>
4. Rørvik PM, Grande T, Einarsrud M-A. One-Dimensional Nanostructures of Ferroelectric Perovskites. *Advanced Materials*. 2011;23(35):4007–4034. <https://doi.org/10.1002/adma.201004676>
5. Weng B, Liu S, Tang Z-R, Xu Y-J. One-dimensional nanostructure based materials for versatile photocatalytic applications. *RSC Advances*. 2014;4(25):12685–12700. <https://doi.org/10.1039/C3RA47910B>
6. Wagner RS, Ellis WC. Vapor-liquid-solid mechanism of single crystal growth. *Appl Phys Lett*. 1964;4(5):89–90. <https://doi.org/10.1063/1.1753975>
7. Trentler TJ, Goel SC, Hickman KM, *et al.* Solution–Liquid–Solid Growth of Indium Phosphide Fibers from Organometallic Precursors: Elucidation of Molecular and Nonmolecular Components of the Pathway. *J Am Chem Soc*. 1997;119(9):2172–2181. <https://doi.org/10.1021/ja9640859>
8. Wen C-Y, Reuter MC, Tersoff J, Stach EA, Ross FM. Structure, Growth Kinetics, and Ledge Flow during Vapor–Solid–Solid Growth of Copper-Catalyzed Silicon Nanowires. *Nano Lett*. 2010;10(2):514–519. <https://doi.org/10.1021/nl903362y>
9. Burton WK, Cabrera N, Frank FC. Role of Dislocations in Crystal Growth. *Nature*. 1949;163(4141):398–399. <https://doi.org/10.1038/163398a0>
10. Burton WK, Cabrera N, Frank FC, Mott NF. The growth of crystals and the equilibrium structure of their surfaces. *Philosophical Transactions of the Royal Society of London Series A, Mathematical and Physical Sciences*. 1951;243(866):299–358. <https://doi.org/10.1098/rsta.1951.0006>
11. Westwater J, Gosain DPGDP, Usui SUS. Control of the Size and Position of Silicon Nanowires Grown via the Vapor-Liquid-Solid Technique. *Jpn J Appl Phys*. 1997;36(10R):6204. <https://doi.org/10.1143/JJAP.36.6204>

12. Oh SH, Benthem K van, Molina SI, *et al.* Point Defect Configurations of Supersaturated Au Atoms Inside Si Nanowires. *Nano Lett.* 2008;8(4):1016–1019. <https://doi.org/10.1021/nl072670+>
13. Kossel W. Extending the Law of Bravais. *Nachr Ges Wiss Göttingen.* 1927;143.
14. Stranski IN. Zur Theorie des Kristallwachstums. *Z Phys Chem.* 1928;136:259–278.
15. Hofmann S, Sharma R, Wirth CT, *et al.* Ledge-flow-controlled catalyst interface dynamics during Si nanowire growth. *Nature Mater.* 2008;7(5):372–375. <https://doi.org/10.1038/nmat2140>
16. Morin SA, Bierman MJ, Tong J, Jin S. Mechanism and Kinetics of Spontaneous Nanotube Growth Driven by Screw Dislocations. *Science.* 2010;328(5977):476–480. <https://doi.org/10.1126/science.1182977>
17. Meng F, Estruga M, Forticaux A, *et al.* Formation of Stacking Faults and the Screw Dislocation-Driven Growth: A Case Study of Aluminum Nitride Nanowires. *ACS Nano.* 2013;7(12):11369–11378. <https://doi.org/10.1021/nn4052293>
18. Jin S, Bierman MJ, Morin SA. A New Twist on Nanowire Formation: Screw-Dislocation-Driven Growth of Nanowires and Nanotubes. *J Phys Chem Lett.* 2010;1(9):1472–1480. <https://doi.org/10.1021/jz100288z>
19. Raynaud GM, Rapp RA. In situ observation of whiskers, pyramids and pits during the high-temperature oxidation of metals. *Oxid Met.* 1984;21(1):89–102. <https://doi.org/10.1007/BF00659470>
20. Tollman RL, Gulbransen EA. Crystal Morphology and Mechanisms of Growth of Alpha-Fe₂O₃ Whiskers on Iron. *J Electrochem Soc.* 1967;114(12):1227. <https://doi.org/10.1149/1.2426455>
21. Gleiter H. The mechanism of grain boundary migration. *Acta Metallurgica.* 1969;17(5):565–573. [https://doi.org/10.1016/0001-6160\(69\)90115-1](https://doi.org/10.1016/0001-6160(69)90115-1)
22. Hirth JP, Pond RC. Steps, dislocations and disconnections as interface defects relating to structure and phase transformations. *Acta Materialia.* 1996;44(12):4749–4763. [https://doi.org/10.1016/S1359-6454\(96\)00132-2](https://doi.org/10.1016/S1359-6454(96)00132-2)
23. Han J, Thomas SL, Srolovitz DJ. Grain-boundary kinetics: A unified approach. *Progress in Materials Science.* 2018;98:386–476. <https://doi.org/10.1016/j.pmatsci.2018.05.004>
24. Heuer AH, Zahiri Azar M. A disconnection mechanism of enhanced grain boundary diffusion in Al₂O₃. *Scripta Materialia.* 2015;102:15–18. <https://doi.org/10.1016/j.scriptamat.2015.01.026>

25. Sternlicht H, Rheinheimer W, Dunin-Borkowski RE, Hoffmann MJ, Kaplan WD. Characterization of grain boundary disconnections in SrTiO₃ part I: the dislocation component of grain boundary disconnections. *J Mater Sci.* 2019;54(5):3694–3709. <https://doi.org/10.1007/s10853-018-3096-4>
26. Sternlicht H, Rheinheimer W, Kim J, *et al.* Characterization of grain boundary disconnections in SrTiO₃ Part II: the influence of superimposed disconnections on image analysis. *J Mater Sci.* 2019;54(5):3710–3725. <https://doi.org/10.1007/s10853-018-3095-5>
27. Sternlicht H, Rheinheimer W, Mehlmann A, Rothschild A, Hoffmann MJ, Kaplan WD. The mechanism of grain growth at general grain boundaries in SrTiO₃. *Scripta Materialia.* 2020;188:206–211. <https://doi.org/10.1016/j.scriptamat.2020.07.015>
28. Zou L, Li J, Zakharov D, Stach EA, Zhou G. In situ atomic-scale imaging of the metal/oxide interfacial transformation. *Nat Commun.* 2017;8(1):307. <https://doi.org/10.1038/s41467-017-00371-4>
29. Qu B, van Benthem K. In situ anisotropic NiO nanostructure growth at high temperature and under water vapor. *Journal of the American Ceramic Society.* 2022;105(4):2454–2464. <https://doi.org/10.1111/jace.18260>
30. Koga K, Hirasawa M. Gas-phase generation of noble metal-tipped NiO nanorods by rapid thermal oxidation. *Mater Res Express.* 2014;1(4):045021. <https://doi.org/10.1088/2053-1591/1/4/045021>
31. Tai K, Sun K, Huang B, Dillon SJ. Catalyzed oxidation for nanowire growth. *Nanotechnology.* 2014;25(14):145603. <https://doi.org/10.1088/0957-4484/25/14/145603>
32. Sun K, Xue J, Tai K, Dillon SJ. The Oxygen Reduction Reaction Rate of Metallic Nanoparticles during Catalyzed Oxidation. *Sci Rep.* 2017;7(1):7017. <https://doi.org/10.1038/s41598-017-07717-4>
33. Kamino T, Yaguchi T, Konno M, *et al.* Development of a gas injection/specimen heating holder for use with transmission electron microscope. *J Electron Microsc.* 2005;54(6):497–503. <https://doi.org/10.1093/jmicro/dfi071>
34. Gaskell DR, Laughlin DE. Introduction to the Thermodynamics of Materials, Sixth Edition. CRC Press; 2017
35. Chen L, Lu W, Lieber CM. Chapter 1 Semiconductor Nanowire Growth and Integration. 2014;1–53. <https://doi.org/10.1039/9781782625209-00001>
36. Chevalier S, Desserrey F, Larpin JP. Oxygen Transport during the High Temperature Oxidation of Pure Nickel. *Oxid Met.* 2005;64(3):219–234. <https://doi.org/10.1007/s11085-005-6560-x>

37. Hirth JP, Mitchell TE. The role of interface structure in oxidation reactions. *Acta Materialia*. 2008;56(19):5701–5707. <https://doi.org/10.1016/j.actamat.2008.07.058>
38. Pieraggi B, Rapp RA, Hirth JP. Role of interface structure and interfacial defects in oxide scale growth. *Oxid Met*. 1995;44(1):63–79. <https://doi.org/10.1007/BF01046723>
39. Pieraggi B, Rapp RA. Stress generation and vacancy annihilation during scale growth limited by cation-vacancy diffusion. *Acta Metallurgica*. 1988;36(5):1281–1289. [https://doi.org/10.1016/0001-6160\(88\)90280-5](https://doi.org/10.1016/0001-6160(88)90280-5)
40. Medlin DL, Sugar JD. Interfacial defect structure at Sb₂Te₃ precipitates in the thermoelectric compound AgSbTe₂. *Scripta Materialia*. 2010;62(6):379–382. <https://doi.org/10.1016/j.scriptamat.2009.11.028>
41. Heinz NA, Ikeda T, Snyder GJ, Medlin DL. Interfacial disconnections at Sb₂Te₃ precipitates in PbTe: Mechanisms of strain accommodation and phase transformation at a tetradymite/rocksalt telluride interface. *Acta Materialia*. 2011;59(20):7724–7735. <https://doi.org/10.1016/j.actamat.2011.08.043>

Chapter 6 Defect redistribution along grain boundaries in SrTiO₃ by externally applied electric fields

This study reports electric field effects on the 45° (100) twist grain boundary core structure of SrTiO₃ bicrystals. Nominal electric field strengths of 50 V/mm and 150 V/mm parallel to the grain boundary plane were applied to the bicrystals during high temperature annealing after diffusion bonding has completed. Atomic structure imaging of the grain boundaries displayed different interface structure near the positive and negative electrodes, respectively. At both nominal field strengths the interface expansion near the positive electrode was roughly 0.8 nm. After annealing at nominally 50 V/mm the width of the grain boundary core close to the negative electrode decreased to roughly 0.4 nm. Unlike for the smaller electric field strength, annealing at nominally 150 V/mm caused decomposition of the boundary structure close to the negative electrode. Electron energy-loss spectroscopy experiments demonstrated a larger degree of oxygen sublattice distortion at the negative electrode side. X-ray photoelectron spectroscopy confirmed enhanced concentrations of Ti³⁺ and Ti²⁺ compared to bulk for both single crystals and bicrystals annealed with an external electric field. The experimental results suggest that oxygen vacancy formation due to the electric field and their migration towards the negative electrode causes the observed alteration of grain boundary structures. At sufficiently high field strength the agglomeration of anion vacancies leads to the decomposition of the grain boundary.

6.1 Introduction

The effect of electric fields on the sintering of ceramic powder compacts has been studied extensively in the past¹. Field assisted sintering, spark plasma sintering (SPS) and flash sintering all utilize applied electric fields and resulting currents to enhance densification²⁻⁶. In addition, externally applied electric fields can decrease the required sintering temperatures or applied pressures, and can enhance or suppress grain growth^{2, 7-13}. Qin and coworkers discovered electrode effects on microstructure development of yttrium-stabilized zirconia during flash sintering with an applied DC bias¹⁴. Enhanced grain growth was observed near the cathode, which is attributed to the DC bias lowering the activation energy for cation migration owing to local reduction-oxidation reactions¹⁴. Jeong and co-workers observed an increased grain boundary migration rate in Al₂O₃ when an external electric field was applied during sintering¹⁵. Mishra and coworkers reported blackening behavior of polycrystalline gadolinium-doped ceria during flash sintering, indicating the migration of oxygen vacancies towards the cathode^{1, 16}. Rheinheimer and coworkers suggested electric field induced defect redistribution in strontium titanate^{13, 17}. Hughes and co-workers have reported electric field effects on atomic grain boundary core structures for 42° (100) twist grain boundaries in SrTiO₃ that were diffusion bonded in the presence of an electric field directed across the interface plane^{18, 19}. In the absence of any externally applied electric field diffusion bonding resulted in a width of the grain boundary core of around 0.8 nm. However, the interface expansion was only approximately 0.4 nm after diffusion bonding in the presence of an externally applied electric field. It was hypothesized that the oppositely charged (100) interface planes of the two half crystals formed a large oxygen vacancy concentration gradient across the forming boundary plane and resulted in

the smaller width of the grain boundary core^{18, 19}. Electron energy loss spectroscopy further revealed disordering on the oxygen sublattice for increasing applied field strengths.

Previous studies by Hughes et al. have shown that grain boundary core modifications accomplished by electric fields during diffusion bonding were only metastable and relied on surface modifications by the electric field during the joining process¹⁹. Instead, this study reports transformations of an almost identical twist grain boundary during annealing of the bicrystal in electric fields post-diffusion bonding. A variety of experimental techniques, including high angle annular dark field STEM (HAADF-STEM), electron energy loss spectroscopy (EELS) and X-ray photoelectron spectroscopy (XPS) were used to characterize atomic and electronic grain boundary structures as a function of relative distance to the electrodes employed for applying electric fields parallel to the grain boundary plane. Comparison of the SrTiO₃ grain boundary core structures near the positive and negative electrodes for two different electric field strengths provides evidence for oxygen vacancy re-distribution and potential decomposition.

6.2 Experimental Techniques

SrTiO₃ bicrystals (SurfaceNet GmbH, Rheine, Germany) with a 45° (100) twist grain boundary were diffusion bonded at 1425°C under an uniaxial pressure of 1 MPa. After diffusion bonding was completed the bicrystals were annealed at 1425°C for 1 hour while an electrostatic field was applied in the direction along the grain boundary plane. Figure 6.1 presents a sketch of the experimental setup. For the application of the electric field two parallel Pt-Rh electrodes were used that were electrically isolated from the bicrystal by roughly 1 mm thick aluminum oxide layers. Annealing experiments were carried out with biases U applied to the electrodes that

were separated from each other by a distance d . Based on this experimental geometry (cf. Figure 6.1) the two resulting applied nominal electric field strengths were $U_{\text{low}}/d = 50 \text{ V/mm}$ and $U_{\text{high}}/d = 150 \text{ V/mm}$. However, the electric field within the SrTiO₃ bicrystal is smaller than the externally applied nominal field E_{total} due to the relatively low dielectric constant of aluminum oxide. In accordance with earlier work by Rheinheimer and co-workers^{13, 17} the electric field within SrTiO₃ (E_{STO}) was calculated using equation (6.1) under the assumption that the SrTiO₃ crystals and the alumina layers can be represented as a series of capacitors with different relative permittivities.

$$\frac{E_{\text{STO}}}{E_{\text{total}}} = \frac{d_{\text{STO}} + d_i}{d_{\text{STO}} \left(1 + \frac{\epsilon_{r, \text{STO}} d_i}{\epsilon_{r, \text{alumina}} d_{\text{STO}}} \right)} \quad (6.1)$$

d_{STO} is the dimension of the SrTiO₃ bicrystal in the direction of the applied field, i.e., the length of the grain boundary plane, d_i is the thickness of the alumina layer, $\epsilon_{r, \text{STO}}$ and $\epsilon_{r, \text{alumina}}$ are the relative permittivities of SrTiO₃ and alumina, respectively. Experiments were conducted with a thin layer of zirconia powder separating the bicrystal from the Al₂O₃ layers to avoid potential solid-state reactions. Incorporating the presence of zirconia (assuming a total thickness of 0.2 mm) into equation (6.1) results in a reduction of the effective field strength to $E_{\text{low}}=26.4 \text{ V/mm}$ and $E_{\text{high}}=79.3 \text{ V/mm}$, respectively¹³.

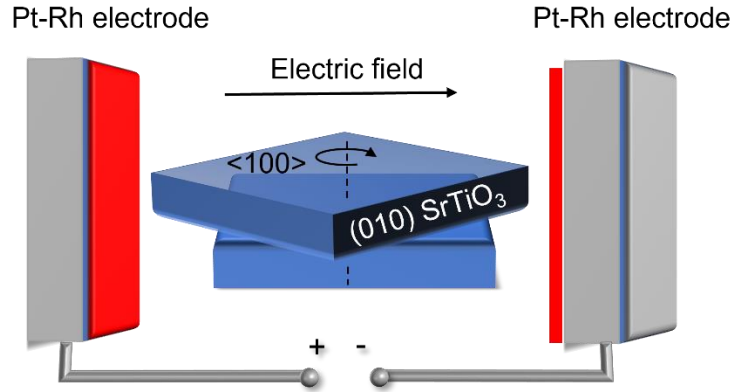


Figure 6.1 Experimental setup of electric field application to the SrTiO₃ bicrystal. The two half single crystals are represented by the blue blocks. The upper crystal is twisted 45° to form the <100> twist boundary. The Pt-Rh electrodes are represented by the two grey blocks. The aluminum oxide insulating layers are represented by the red layers right next to the electrodes. The electric field is parallel to the grain boundary plane.

After electric field annealing the structural homogeneity of the bicrystals was qualitatively assessed by scanning electron microscopy. Secondary electron (SE) imaging of the areas that include the grain boundary over the full length of the grain boundary plane was carried out using either a FEI Scios dual-beam focused ion beam (FIB) instrument (FEI, Hillsboro, OR), or a Thermo Fisher Quattro environmental scanning electron microscope (Thermo Fisher Scientific, Hillsboro, OR). The Thermo Fisher MAPS2.0 software was used to capture high magnification SE micrographs along the entire length of the grain boundary. Recorded images were subsequently spliced together by maximizing cross-correlation functions in overlapping areas to obtain large field micrographs with potential topography contrast indicating grain boundary grooving. A similar experimental approach was previously utilized to assess the quality of interfacial bonding of bicrystals fabricated by SPS.^{20, 21}

Grain boundaries were prepared for cross-sectional transmission electron microscopy (TEM) characterization using FIB sectioning. Electron transparent lamellae were extracted for each bicrystal from areas close to the positive and negative electrode. Samples were thinned to thicknesses between 200 nm and 300 nm and subsequently extracted by standard in-situ lift-out procedures. Thereafter a Fischione Nanomill instrument (Fischione Industries, Export, PA) was used to reduce sample thicknesses to around 50 nm using a low-energy Ar⁺ ion beam.

Atomic grain boundary structures were characterized by aberration-corrected HAADF-STEM imaging. Samples of the bicrystal annealed at 50 V/mm were imaged with a JEOL JEM 2100AC aberration-corrected STEM at UC Davis operated at 200 kV. The bicrystal annealed in the presence of a nominal electric field strength of 150 V/mm was characterized with an acceleration voltage of 300 kV utilizing the FEI TEAM 0.5 instrument installed at Lawrence Berkeley National Laboratory. The local electronic grain boundary core structures were determined by spatially resolved EELS. Spectra of the O K and Ti L_{2,3} absorption edges were recorded with a Gatan Imaging Filter (GIF Tridem; Gatan Inc. Pleasanton, CA) attached to the JEOL JEM 2100AC microscope. The energy dispersion during EELS acquisition was 0.1 eV/channel and pixel dwell times were either 0.1 or 0.2 s/spectrum. The probe-forming convergence semi-angle and the collection semi-angle were both 16 mrad. All the spectra were background subtracted using the conventional power-law fitting procedure²². Principle component analysis (PCA) was applied to all background subtracted spectra to improve signal-to-noise ratios using the singular value decomposition algorithm in HyperSpy²³. The near-edge fine structures (ELNES) of the background subtracted Ti L_{2,3} edge spectra were reconstructed from the first 8 components of the PCA deconstruction. The O K ELNES were reconstructed from the first 6 components. All ELNES plots were calibrated with respect to the edge onset of

the bulk spectrum, i.e., the energy-loss at which the second derivative of the bulk spectrum equals zero. Energy dispersive X-ray spectroscopy (EDXS) line profiles were recorded across the grain boundaries with an Oxford Aztec Energy TEM Advanced Microanalysis System with an X-MaxN TSR Windowless large area Analytical Silicon Drift Detector.

X-ray photoelectron spectroscopy (XPS) measurements of Ti 2p signals were carried out using a Kratos AXIS Supra instrument equipped with a monochromatic Al K_{α} source ($h\nu = 1486.6$ eV). XPS data were acquired at 150W (10mA, 15kV) from surfaces of the bicrystals that faced the negative electrode during electric field annealing. A slot aperture was employed with an energy resolution of about 1.6 eV, a dwell time of 600 ms, and a step size of 0.040 eV. Single crystals of SrTiO₃ were field annealed using the same temperatures and field strength as the bicrystals. XPS data from the single crystals were acquired from 4 or 5 equidistant locations between the electrodes. XPS experiments with the single crystals were carried out using a 55 μm circular aperture. Spectra were recorded with a dwell time of 200 ms and a step size of 0.015 eV. The Kratos ESCApe program was used for data acquisition and subsequent peak area fitting. Intensity minima were identified on both sides of the Ti 2p peak doublet and a Shirley²⁴ background was fitted to the corresponding energy interval. Each spectrum was subsequently fitted with six asymmetrical Gaussian-Lorentzian peaks. For direct comparison individual XPS spectra were background-subtracted. The largest spectral intensity, i.e., the maximum of the main Ti 2p peak in bulk SrTiO₃ was calibrated to an energy of 458.4 eV.

6.3 Results:

(a) SEM

Figure 6.2 displays large field of view SEM maps of the bicrystals after field annealing. For Figure 6.2 (a) the location of the grain boundary plane after field annealing at 50V/mm was ascertained from high resolution micrographs recorded from the edges of the bicrystal close to the two electrodes and is indicated by a dashed line. No SE contrast resulting from grain boundary grooving can be observed. Figure 6.2(b) and (c) show SEM maps recorded from the bicrystals close to the negative electrode after field annealing at 150 V/mm. Dark line-shaped contrasts are observed indicating the location of the grain boundary (highlighted by white arrows). Close to the positive electrode (cf. Figure 6.3(d)) no topography contrast due to grain boundary grooving was detected.

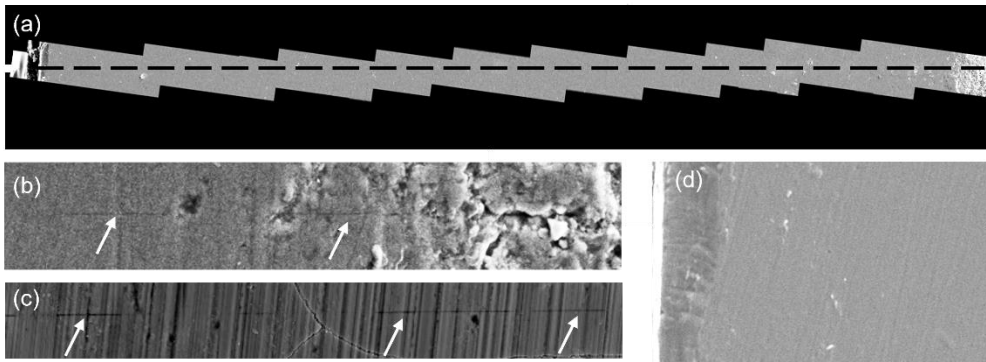


Figure 6.2 (a) SE map of the entire grain boundary area after bicrystal annealing with a nominal field strength of 50 V/mm. The dashed line indicates the location of the grain boundary. (b, c) SE maps of the grain boundary area close to the negative electrode after annealing at 150 V/mm. (d) SE image of the grain boundary area close to the positive electrode after annealing at 150 V/mm.

(b) HAADF-STEM

Figure 6.3(a) and (b) show atomic resolution HAADF-STEM images recorded from the grain boundary core structures of the bicrystal annealed at 50 V/mm. Figure 6.3(a) was recorded from an area close to the positive electrode, while Figure 6.3(b) was captured close to the negative electrode. The grain boundary core structures on both sides of the bicrystal are periodic along the grain boundary plane. The width of the grain boundary core, i.e., the interface expansion, is defined as the distance between the last crystal plane in either half crystal that is indistinguishable from the bulk. The interface expansions are approximately 0.80 nm close to the positive electrode, and only about 0.36 nm close to the negative electrode.

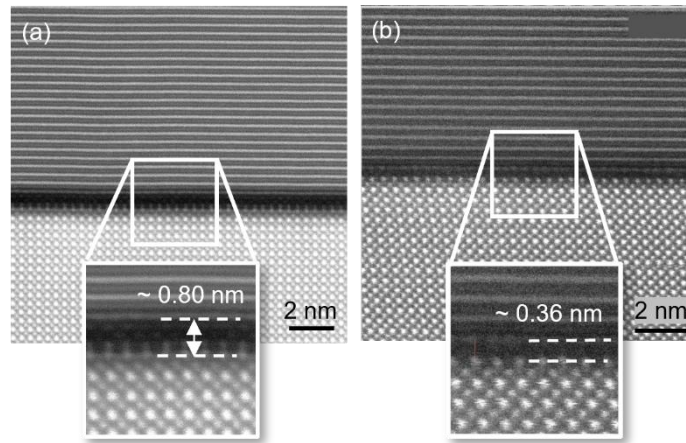


Figure 6.3 HAADF-STEM images of grain boundary core structures after annealing at 50 V/mm recorded from close to (a) the positive and (b) the negative electrode.

After electric field assisted annealing at nominally 150 V/mm the grain boundary expansion close to the positive electrode was roughly 0.8 nm (see Figure 6.4(a)). At the negative electrode side, however, no clearly defined abrupt grain boundary core structure was observed. Instead, conventional bright field TEM imaging (Figure 6.4(b)) revealed the formation of at least one secondary phase between the two adjacent half crystals. The interfacial phase was observed

to be sensitive to electron beam damage. Its width increases with proximity to the negative electrode used during field annealing. EDXS linescans across the interfacial phase revealed the local enrichment of SrTiO₃ with aluminum (Al) and silicon (Si), as indicated in Figure 6.4(b).

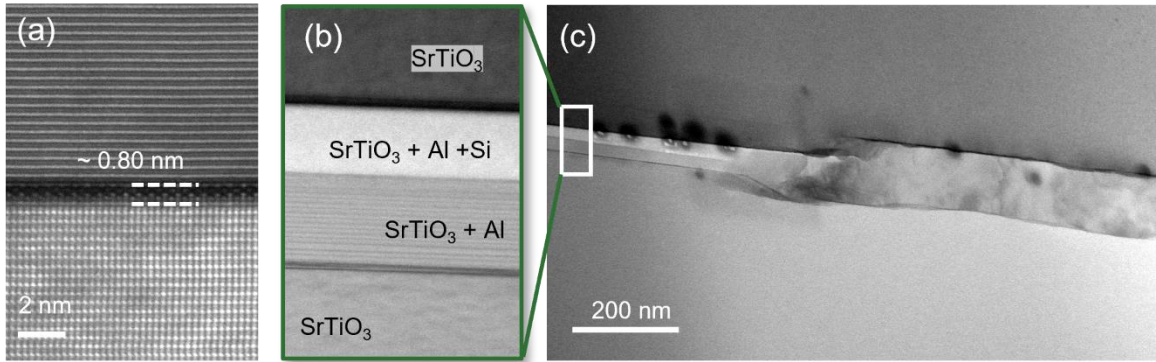


Figure 6.4 (a) HAADF-STEM image of the grain boundary core recorded close to the positive electrode after field annealing at nominally 150 V/mm. (b) and (c) are bright field TEM images that were recorded close to the negative electrode and display the formation of interfacial phases. EDXS analysis (not displayed) revealed the presence of Al and/or Si.

(c) *EELS*:

Ti L_{2,3} and O K ELNES plotted in Figure 6.5(a) were acquired from an area close to the negative electrode for the SrTiO₃ bicrystal annealed in the presence of a nominal field strength of 50 V/mm. The Ti L_{2,3} ELNES line shape obtained from bulk SrTiO₃ exhibits well-resolved *t*_{2g} and *e*_g peak splitting of 2.4 eV for both L₂ and L₃ edges. At the grain boundary, however, the crystal field splitting is reduced to approximately 1.6 eV (cf. green spectrum in Figure 6.5(a)). The O K edge in bulk SrTiO₃ reveals five major peaks labeled A through E. The spectrum recorded from the grain boundary plane displays a different ELNES with peaks A', B' and C'

that are suppressed relative to the bulk, while peak D observed in the bulk is absent at the grain boundary.

Ti $L_{2,3}$ and O K ELNES recorded from an area close to the positive electrode after annealing at 50 V/mm are plotted in Figure 6.5(b). Spectra recorded from both half crystals of the bicrystal reproduce those of bulk SrTiO₃ (cf. Figure 6.5(a)). At the grain boundary (red spectrum in Figure 6.5(b)), t_{2g} and e_g peaks of the Ti $L_{2,3}$ ELNES are resolved but exhibit a slightly reduced crystal field splitting of 1.9 eV compared to 2.4 eV in bulk SrTiO₃. The O K ELNES recorded from the grain boundary core is less pronounced compared to the bulk but indicates otherwise almost identical line shapes.

Figure 6.6 shows the Ti $L_{2,3}$ and O K ELNES recorded from an area close to the positive electrode after annealing at 150 V/mm. No EELS data was recorded from the negative electrode side of the same bicrystal due to the absence of an atomically structured grain boundary core (cf. Figure 6.4(b) & (c)). While the spectra recorded from the half crystals are indistinguishable from both those for bulk SrTiO₃ and those displayed in Figure 6.5, the Ti $L_{2,3}$ ELNES recorded from the grain boundary core does not present distinguishable t_{2g} and e_g signatures. The O K ELNES recorded from the grain boundary core shows a relatively small signal to noise ratio which challenges the resolution of individual ELNES peaks. However, it appears that all major peaks A through E observed for bulk SrTiO₃ are retained at the grain boundary core.

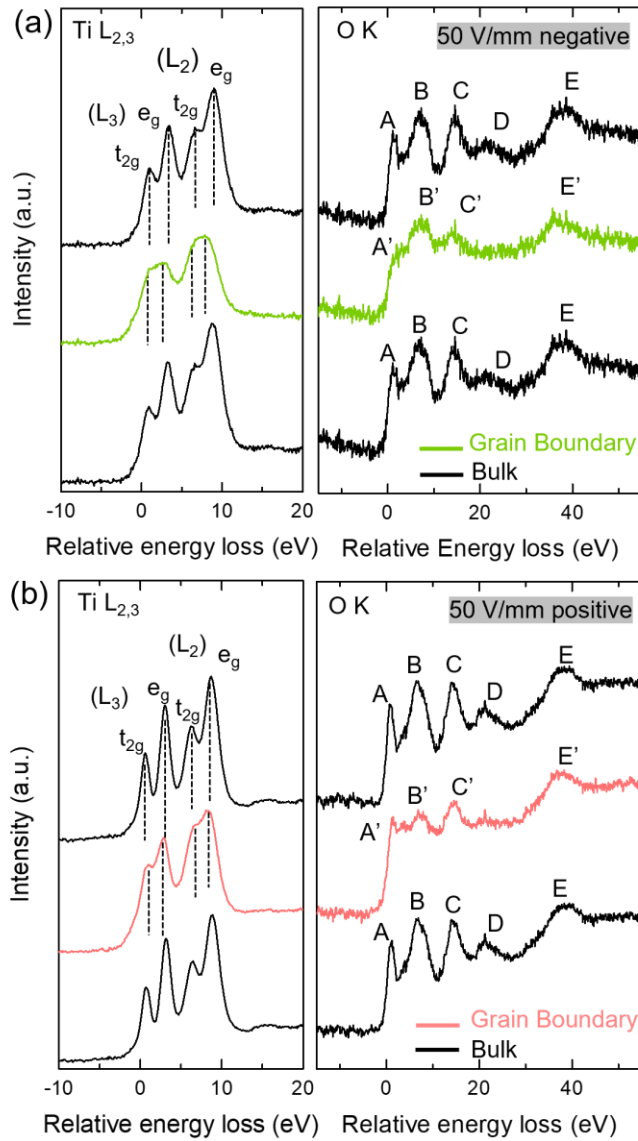


Figure 6.5 Ti $L_{2,3}$ and O K edges recorded after annealing at 50V/mm from the grain boundary core and adjacent SrTiO₃ half crystals close to (a) the negative and (b) the positive electrode. Spectra obtained from the SrTiO₃ half crystals (bulk) are all plotted in black; Ti $L_{2,3}$ and O K spectra obtained from the grain boundary are plotted in green and red, respectively

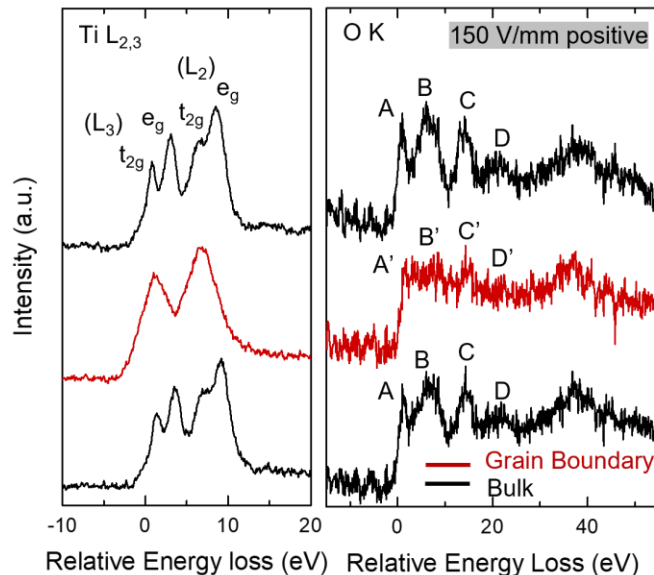


Figure 6.6 Ti L_{2,3} and O K edges recorded near the positive electrode after annealing at 150 V/mm from the grain boundary and adjacent SrTiO₃ half crystals. Spectra obtained from the SrTiO₃ half crystals (bulk) are all plotted in black while spectra acquired from the grain boundary are plotted in red.

(d) XPS:

Figure 6.7 shows XPS spectra of the Ti 2p_{3/2} and Ti 2p_{1/2} doublet acquired from a reference spectrum of single-crystalline bulk SrTiO₃ in comparison to data recorded from field annealed SrTiO₃ single crystals and surfaces of the field annealed bicrystals that included the grain boundary. All spectra in Figure 6.7 were normalized with respect to the maximum intensity of the Ti(IV) peak representing an oxidation state of Ti⁴⁺ in bulk SrTiO₃²⁵. The spectra were then smoothed using Savitzky-Golay method with a quadratic polynomial²⁶. Spectra recorded from the field-annealed samples also include spectral intensities labeled Ti(III) and Ti(II) reflecting Ti³⁺ and Ti²⁺ oxidation states, respectively²⁵. After annealing in the presence of an electric field strength of nominally 50 V/mm the spectra recorded from the bicrystal and the single crystal are indistinguishable. Annealing at 150 V/mm, however, causes the bicrystal to reveal relatively higher intensities of the Ti(III) and Ti(II) peaks, while the signals for the single crystal are

smaller compared to the data recorded after annealing at 50 V/mm. The same data normalized to the total integrated intensities demonstrates that Ti(III) and Ti(II) signals increase at the cost of Ti(IV) intensities.

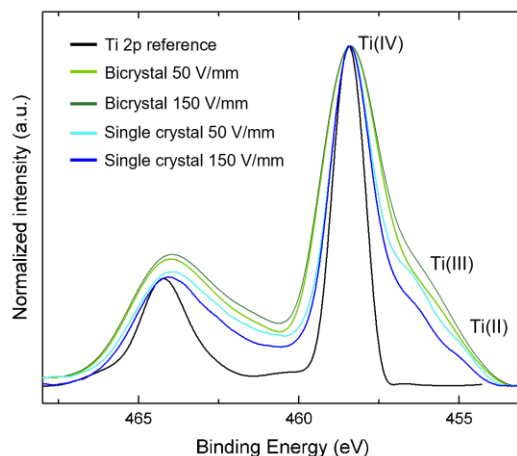


Figure 6.7 Ti 2p XPS doublet for the reference single crystal (black), for bicrystals after electric field annealing at 50 V/mm (light green) and 150 V/mm (dark green), and for single crystals after annealing at 50 V/mm (light blue) and 150 V/mm (dark blue).

After field annealing the single crystals of SrTiO_3 were cut through their center and polished for cross-sectional XPS analysis. Ti 2p spectra were recorded from multiple equidistant locations between the surfaces that were facing the two electrodes during annealing. After peak fitting fractional intensities of the Ti(III) and Ti(II) signatures were extracted and plotted in Figures 6.8 as a function relative distance for both field strengths. Trend lines between the data points were added to guide the eye, and the equivalent fractional intensities recorded from the surface close to the negative electrode of bicrystal samples were included for comparison. After annealing at 50 V/mm Figure 6.8(a) and 6.8(b) show that fractional intensities for Ti(III) and

Ti(II) remain mostly unchanged between the two electrodes. The fractional Ti(II) intensities throughout the single crystal are in good agreement with those observed from the negative electrode side of the bicrystal. The trendline in Figure 6.8(a) suggests a gradual increase of Ti(III) when approaching the negative electrode. Ti(III) intensities recorded from the single crystal, however, do not reproduce those observed from the bicrystal. After annealing at 150 V/mm fractional intensities for Ti(III) and Ti(II) show trends with non-zero slopes between the two electrodes. Fractional intensities for Ti(III) gradually decrease when approaching the negative electrode and diverge from the data observed from the bicrystal (see Figure 6.8(a)). In contrast, fractional intensities for Ti(II) increase when approaching the negative electrode and converge towards the fractional intensities observed from the bicrystal.

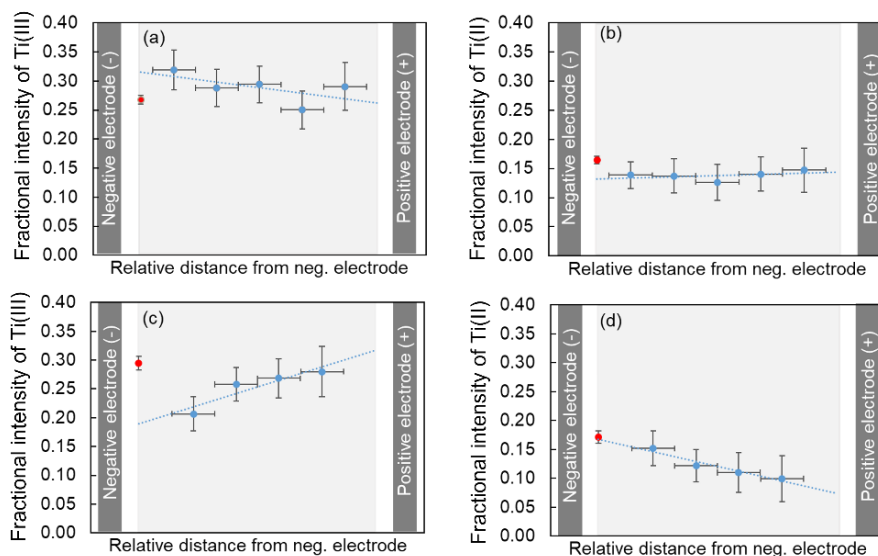


Figure 6.8 Fractional intensities of the Ti(III) and Ti(II) signatures as a function of relative distance recorded after annealing at (a & b) 50 V/mm and 150 V/mm (b & c), respectively. The light grey background indicate the location of the SrTiO₃ single crystal between the two electrodes. XPS data were acquired from equal distant locations of field-annealed single crystals of SrTiO₃. The red data points represent XPS measurements recorded from the surface of the SrTiO₃ bicrystal close the negative electrode. The dashed line is a trend line and serves a guide to the eye.

6.4 Discussion:

SEM and STEM imaging of the 45° (100) bicrystals of SrTiO₃ has shown that thermal annealing in the presence of an electric field directed parallel to the grain boundary plane alters grain boundary core structures. For a nominal field strength of 50 V/mm no topography variations due to grain boundary grooving were detected by SEM (cf. Figure 6.2 (a)) indicating a relatively dense interface structure without extensive pore formation²⁷. HAADF-STEM imaging however has revealed different interface expansions of about 0.8 nm close to the positive electrode, and only around 0.4 nm close to the negative electrode. The widths of grain boundary cores observed in this study are consistent with those previously observed from grain boundaries with almost identical macroscopic degrees of freedom but diffusion bonded with electric fields directed across the interface plane¹⁹. The application of electric bias to (100) surfaces of SrTiO₃ alters the oxygen stoichiometry of the free surface depending on the polarization²⁸. The resulting large oxygen concentration gradient across the interface plane during diffusion bonding was reported to be responsible for the narrowing of the grain boundary core structure in the presence of an electric field. The different interface expansions observed in this study from the same grain boundary after annealing with an electric field along the grain boundary plane is an additional indicator for the migration of oxygen vacancies that was previously suggested by Rheinheimer and co-workers¹⁷. Cation re-arrangement hence occurs to accommodate charge neutrality.

ELNES experiments of the bicrystal annealed at 50 V/mm carried out close to the negative and positive electrodes demonstrate a reduction of Ti at the grain boundary compared to the bulk. The crystal field splitting of the t_{2g} and e_g states is smaller close to the negative electrode, indicating a stronger modification of TiO₆ octahedra that results from an increased oxygen

vacancy concentration. Hughes and coworkers¹⁹ reported a suppression of peak B in the O K ELNES line shapes for SrTiO₃ bicrystals bonded with no electric field indicating alterations of Sr-O bonding^{29, 30}. Muller also reported similar results for SrTiO₃ with low oxygen vacancy concentration³¹. ELNES line shapes recorded in this study from areas close to the positive electrode exhibit an only slightly dampened peak B. From this observation it is concluded that the oxygen vacancy concentration and, hence, the local space charge configuration of the bicrystal close to the positive electrode is dominated by the structural inhomogeneity caused by the misorientation of the adjacent half crystals, and is less affected by the applied electric field. In the same area ELNES line shapes for the O K edge are similar to bulk SrTiO₃ with all five major peaks resolved albeit less pronounced. This observation suggests marginal re-arrangement of oxygen anions and a negligible contribution of oxygen vacancies¹⁸. However, the ELNES line shapes of O K edge acquired at the negative electrode side of the bicrystal differs dramatically as the two major peaks labeled A and D are mostly absent. Peak A originates from the hybridization of titanium 3*d* orbitals and oxygen 2*p* orbitals. Peak D originates from the splitting of Ti 3*d* orbitals that is reflected at higher electron energy losses. The absence of both peaks indicates that the Ti-O bonding close to the negative electrode is different than that at the positive side, which can be attributed to a distortion on the oxygen sublattice and local reduction of the Ti⁴⁺. The O K ELNES recorded close to the negative electrode is indeed consistent with a bonding configuration in a reduced titanium oxide³². The combination of atomic resolution imaging and energy-loss spectroscopy therefore confirms that within an applied electric field the positively charged oxygen vacancies migrate along the grain boundary plane towards the negative, hence resulting in a local enrichment of oxygen vacancies.

After annealing of the bicrystal in the presence of a nominal field strength of 150 V/mm, SEM micrographs recorded from areas close to the negative electrode reveal significant topography contrast due to grain boundary grooving. Such contrast is absent close to the positive electrode. This observation suggests considerable alterations of the grain boundary core structure both as a function of proximity of the negative electrode, and the applied electric field strength. STEM observations from the grain boundary close to the positive electrode reveal a periodic interface structure along the interface plane with a width of the grain boundary core of around 0.8 nm. This result is similar to that observed from the area close to the positive electrode after annealing at a lower field strength of only 50 V/mm. Close to the negative electrode, however, FIB lamella extracted from areas that did not show strong topography contrast (see arrow in Figure 6.2b) revealed a broad dark contrast during ion-beam thinning (cf. Figure 6.9).

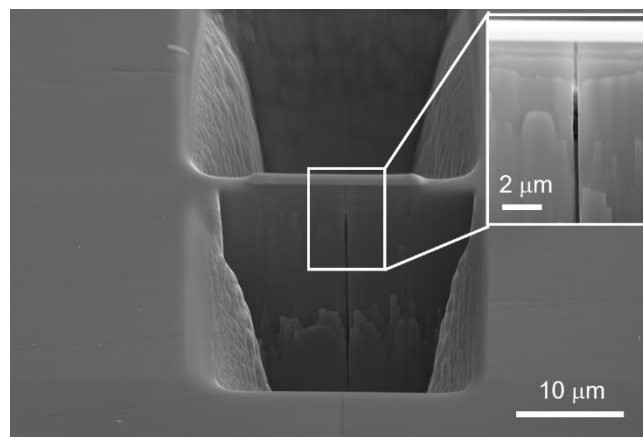


Figure 6.9 SEM image of the FIB lamella extracted from areas without strong topography contrast near the 150 V/mm negative electrode side. Higher magnification image of the dark contrast observed during ion-beam thinning is displayed on the top right.

Subsequent STEM characterization (Figure 6.4(b) & (c)) revealed the formation of at least two beam sensitive interfacial phases that are enriched with Al and Si. It is therefore concluded

that the relatively high applied field strength provides a considerable driving force for the migration of oxygen vacancies towards the negative electrode. As a result, the local enrichment of oxygen vacancies causes deconstruction of the grain boundary as observed in Figure 6.4(b) and 4(c). Rodenbücher et al.³³ have previously shown that DC fields and the presence of oxygen vacancies can cause local reduction and induce stoichiometry polarization which allows for a controlled decomposition of SrTiO₃. Similar kinetic unmixing was reported for high oxygen deficiencies for BaTiO₃³⁴ and for NiTiO₃³⁵ which crystallizes with the ilmenite structure. The insertion of Al and Si into the highly defective grain boundary region close to the negative electrode likely resulted from solid state diffusion from Al₂O₃ buffers layers during thermal annealing, or mechanical polishing agents during sample preparation, respectively.

XPS experiments (cf. Figure 6.7) confirm the expected formation of oxygen vacancies due to the applied electric field by the appearance of Ti(III) and Ti(II) signatures that reflect Ti³⁺ and Ti²⁺ oxidation states. Neither were detected from bulk SrTiO₃ prior to electric field annealing. XPS spectra from the single crystal and the bicrystal are indistinguishable recorded after field annealing at 50 V/mm, which suggests that the oxygen vacancy concentrations resolved by XPS are dominated by the electric field and not by the charge compensation mechanism related to the grain boundary. However, after annealing at 150V/mm Ti³⁺ and Ti²⁺ intensities decrease in bulk SrTiO₃ compared to the smaller field strength and increase for the bicrystal. From this observation it is concluded that at sufficiently high field strength the generation of oxygen vacancies is counteracted by re-filling of vacancy sites with oxygen from the atmosphere. This kinetic effect decreases the vacancy concentration compared to that observed at lower field strength. In the case of the bicrystal, however, comparison of Figures 6.8(c) and (d) to Figures

6.8(a) and (b), respectively suggests that the increased field strength causes the formation of more Ti^{2+} states by further reducing Ti^{3+} close to the negative electrode.

6.5 Conclusions:

This study provides direct experimental evidence for oxygen vacancy redistribution along a twist grain boundary in $SrTiO_3$ when an external electric field is applied. Field annealing at a nominal field strength of 50 V/mm causes a larger grain boundary expansion near the positive electrode compared to areas close to the negative electrode. ELNES analysis of electronic grain boundary structures combined with XPS experiments confirmed the migration of oxygen vacancies towards the negative electrode during electric field annealing. For sufficiently high field strengths oxygen vacancy agglomeration near the negative electrode can cause decomposition of the grain boundary structure. However, XPS experiments also suggest that during annealing at relatively high field strength it may become energetically more favorable to fill vacancy sites with oxygen from atmosphere. The experimental results of this study indicate that electric fields can alter grain boundary atomic and electronic core structures by the redistribution of oxygen vacancies as a function of the externally applied field strength and direction. It may therefore become feasible to replace variations of oxygen partial pressure atmospheres during ceramic manufacturing by the application of electric fields.

Acknowledgements:

The authors from UC Davis acknowledge financial support from the US National Science Foundation (DMR- 1836571). The Kratos AXIS Supra XPS instrument was funded by the NSF-MRI program (DMR-1828238). Parts of this project were carried out at the Center for Nano and

Micro Manufacturing (CNM2) and the Advanced Materials Characterization and Testing Laboratory (AMCaT) at UC Davis. Work at the National Center for Electron Microscopy (NCEM) was supported by the Office of Science, Office of Basic Energy Sciences, of the U.S. Department of Energy under Contract No. DE-AC02-05CH11231.

6.6 References:

1. Guillon O, De Souza RA, Mishra TP, Rheinheimer W. Electric-field-assisted processing of ceramics: Nonthermal effects and related mechanisms. *MRS Bulletin*. 2021;46(1):52–58. <https://doi.org/10.1557/s43577-020-00008-w>
2. Munir ZA, Anselmi-Tamburini U, Ohyanagi M. The effect of electric field and pressure on the synthesis and consolidation of materials: A review of the spark plasma sintering method. *J Mater Sci*. 2006;41(3):763–777. <https://doi.org/10.1007/s10853-006-6555-2>
3. Munir ZA, Quach DV, Ohyanagi M. Electric Current Activation of Sintering: A Review of the Pulsed Electric Current Sintering Process. *Journal of the American Ceramic Society*. 2011;94(1):1–19. <https://doi.org/10.1111/j.1551-2916.2010.04210.x>
4. Yu M, Grasso S, Mckinnon R, Saunders T, Reece MJ. Review of flash sintering: materials, mechanisms and modelling. *Advances in Applied Ceramics*. 2017;116(1):24–60. <https://doi.org/10.1080/17436753.2016.1251051>
5. Guillon O, Gonzalez-Julian J, Dargatz B, *et al*. Field-Assisted Sintering Technology/Spark Plasma Sintering: Mechanisms, Materials, and Technology Developments. *Advanced Engineering Materials*. 2014;16(7):830–849. <https://doi.org/10.1002/adem.201300409>
6. Majidi H, van Benthem K. Consolidation of Partially Stabilized ZrO₂ in the Presence of a Noncontacting Electric Field. *Phys Rev Lett*. 2015;114(19):195503. <https://doi.org/10.1103/PhysRevLett.114.195503>
7. Olevsky EA, Kandukuri S, Froyen L. Consolidation enhancement in spark-plasma sintering: Impact of high heating rates. *Journal of Applied Physics*. 2007;102(11):114913–114913.
8. Schwarz S, Thron AM, Rufner J, Benthem K, Guillon O. Low Temperature Sintering of Nanocrystalline Zinc Oxide: Effect of Heating Rate Achieved by Field Assisted Sintering/Spark Plasma Sintering. *J Am Ceram Soc*. 2012;95(8):2451–2457. <https://doi.org/10.1111/j.1551-2916.2012.05205.x>

9. Chaim R. Densification mechanisms in spark plasma sintering of nanocrystalline ceramics. *Mater Sci Eng A*. 2007;443(1–2):25–32.
10. Yang D, Conrad H. Enhanced Sintering Rate and Finer Grain Size in Ytria-Stablized Zirconia (3Y-TZP) with Combined DC Electric Field and Increased Heating Rate. 2010. <https://doi.org/10.1016/j.msea.2010.10.041>
11. Ghosh S, Chokshi AH, Lee P, Raj R. A Huge Effect of Weak dc Electrical Fields on Grain Growth in Zirconia. 2009;92(8):1856–1859. <https://doi.org/10.1111/j.1551-2916.2009.03102.x>
12. Rufner JF, Kaseman D, Castro RHR, van Benthem K. DC Electric Field-Enhanced Grain-Boundary Mobility in Magnesium Aluminate During Annealing. *J Am Ceram Soc*. 2016;99(6):1951–1959. <https://doi.org/10.1111/jace.14157>
13. Rheinheimer W, Füllung M, Hoffmann MJ. Grain growth in weak electric fields in strontium titanate: Grain growth acceleration by defect redistribution. *Journal of the European Ceramic Society*. 2016;36(11):2773–2780. <https://doi.org/10.1016/j.jeurceramsoc.2016.04.033>
14. Qin W, Majidi H, Yun J, van Benthem K. Electrode Effects on Microstructure Formation During FLASH Sintering of Yttrium-Stabilized Zirconia. *Journal of the American Ceramic Society*. 2016;99(7):2253–2259. <https://doi.org/10.1111/jace.14234>
15. Jeong J-W, Han J-H, Kim D-Y. Effect of Electric Field on the Migration of Grain Boundaries in Alumina. *Journal of the American Ceramic Society*. 2000;83(4):915–918. <https://doi.org/10.1111/j.1151-2916.2000.tb01294.x>
16. Mishra TP, Neto RRI, Speranza G, *et al*. Electronic conductivity in gadolinium doped ceria under direct current as a trigger for flash sintering. *Scripta Materialia*. 2020;179:55–60. <https://doi.org/10.1016/j.scriptamat.2020.01.007>
17. Rheinheimer W, Parras JP, Preusker J-H, De Souza RA, Hoffmann MJ. Grain growth in strontium titanate in electric fields: The impact of space-charge on the grain-boundary mobility. *Journal of the American Ceramic Society*. 2019;102(6):3779–3790. <https://doi.org/10.1111/jace.16217>
18. Hughes LA, Marple M, van Benthem K. Electrostatic fields control grain boundary structure in SrTiO₃. *Appl Phys Lett*. 2018;113(4):041604. <https://doi.org/10.1063/1.5039646>
19. Hughes LA, Benthem K van. Effects of electrostatic field strength on grain-boundary core structures in SrTiO₃. *Journal of the American Ceramic Society*. 2019;102(8):4502–4510. <https://doi.org/10.1111/jace.16344>
20. Hughes LA, van Benthem K. Formation of SrTiO₃ bicrystals using spark plasma sintering techniques. *Scr Mater*. 2016;118:9–12. <https://doi.org/10.1016/j.scriptamat.2016.03.005>

21. Hughes LA, van Benthem K. Spark Plasma Sintering Apparatus Used for the Formation of Strontium Titanate Bicrystals. *Journal of Visualized Experiments*. 2017;(120):e55223–e55223. <https://doi.org/10.3791/55223>
22. Egerton RF. An Introduction to EELS. In: Egerton RF, ed. *Electron Energy-Loss Spectroscopy in the Electron Microscope*. Boston, MA: Springer US; 2011:1–28. https://doi.org/10.1007/978-1-4419-9583-4_1
23. Peña F de la, Prestat E, Fauske VT, *et al.* hyperspy/hyperspy: Release v1.6.5. Zenodo; 2021 <https://doi.org/10.5281/zenodo.5608741>
24. Oelhafen P. Practical surface analysis by auger and X-ray photoelectron spectroscopy: Edited by D. Briggs and MP Seah, John Wiley and Sons, 1983, 533pp., ISBN 0471 26279 X. Elsevier; 1984
25. Powell C. X-ray Photoelectron Spectroscopy Database XPS, Version 4.1, NIST Standard Reference Database 20. 1989. <https://doi.org/10.18434/T4T88K>
26. Gorry PA. General least-squares smoothing and differentiation by the convolution (Savitzky-Golay) method. *Anal Chem*. 1990;62(6):570–573. <https://doi.org/10.1021/ac00205a007>
27. Hughes LA, van Benthem K. Low Angle Twist Boundary in SrTiO₃ Fabricated by Spark Plasma Sintering Techniques. *J Am Ceram Soc*. 2018. <https://doi.org/10.1111/jace.15863>
28. Leisegang T, Stöcker H, Levin AA, *et al.* Switching Ti Valence in SrTiO₃ by a dc Electric Field. *Phys Rev Lett*. 2009;102(8):087601. <https://doi.org/10.1103/PhysRevLett.102.087601>
29. Seo H, Posadas AB, Mitra C, Kvit AV, Ramdani J, Demkov AA. Band alignment and electronic structure of the anatase TiO₂/SrTiO₃(001) heterostructure integrated on Si(001). *Phys Rev B*. 2012;86(7):075301. <https://doi.org/10.1103/PhysRevB.86.075301>
30. Zhang J. Application of electron energy-loss spectroscopy to ferroelectric thin films. Halle (Saale), Univ., Diss., 2004; 2004
31. Muller DA, Nakagawa N, Ohtomo A, Grazul JL, Hwang HY. Atomic-scale imaging of nanoengineered oxygen vacancy profiles in SrTiO₃. *Nature*. 2004;430(7000):657–661. <https://doi.org/10.1038/nature02756>
32. Huang C-N, Bow J-S, Zheng Y, Chen S-Y, Ho N, Shen P. Nonstoichiometric Titanium Oxides via Pulsed Laser Ablation in Water. *Nanoscale Res Lett*. 2010;5(6):972–985. <https://doi.org/10.1007/s11671-010-9591-4>

33. Rodenbücher C, Meuffels P, Bihlmayer G, *et al.* Electrically controlled transformation of memristive titanates into mesoporous titanium oxides via incongruent sublimation. *Sci Rep.* 2018;8(1):3774. <https://doi.org/10.1038/s41598-018-22238-4>
34. Yoo H-I, Lee C-E, De Souza RA, Martin M. Equal mobility of constituent cations in BaTiO₃. *Appl Phys Lett.* 2008;92(25):252103.
35. Chun J, Martin M, Yoo H-I. Electrotransport-induced unmixing and decomposition of ternary oxides. *J Appl Phys.* 2015;117(12):124504. <https://doi.org/10.1063/1.4915626>

Chapter 7: Tip guided growth of nickel nanostructure with the application of electric current

7.1 Introduction

Previous study by Rufner and co-workers reported the one-directional growth of nickel nanostructure inside the scanning transmission electron microscope¹. A DC bias was applied to a fixed tungsten tip and the sample was connected to microscope ground. Contact was made between the tip and the nickel particle agglomerate. Figure 7.1 (a) shows the recorded current as a function of time and the DC bias applied during each time frame. No external heating was applied to during the experiment. Dielectric breakdown of the thin oxide layer on particle took place and is indicated by the arrows in Figure 7.1(a). Figure 7.1(b) shows the one directional longitudinal growth process of the nickel nanostructure.

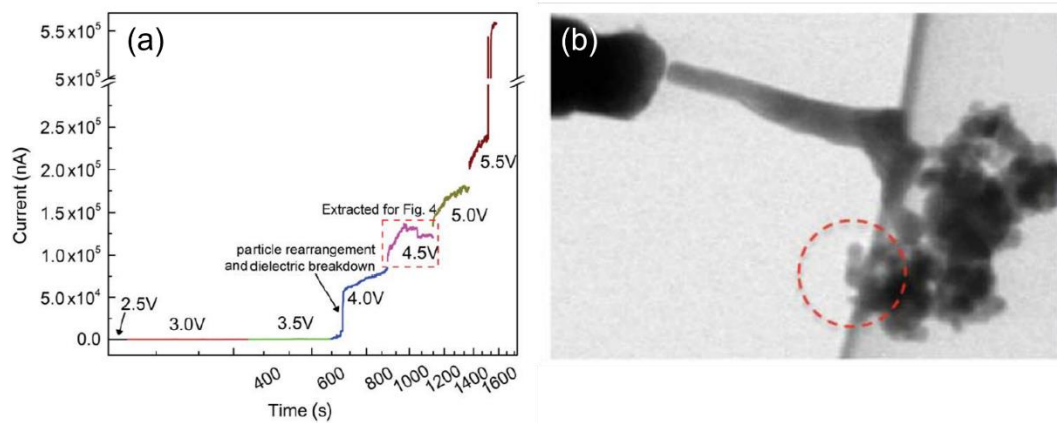


Figure 7.1 (a) Current versus time plot for the full duration of the in situ TEM experiment. (b) The obtained nanostructure after growth.

(Reproduced from Reference¹)

One possible growth mechanism proposed is electromigration. Electromigration causes mass transport when a current flows through the metal material. The driving force \mathbf{F} comes from two forces from the process and is expressed in equation (7.1). One is electrostatic force caused by the electric field on the metal atoms, denoted by $\mathbf{F}_{\text{direct}}$, and the electron wind force generated by the bombardment of the flowing electrons onto the metal atoms, denoted by \mathbf{F}_{wind} ^{2, 3}. Z^* is the effective charge.

$$\mathbf{F} = \mathbf{F}_{\text{direct}} + \mathbf{F}_{\text{wind}} = (Z_{\text{direct}} + Z_{\text{wind}})e\mathbf{E} = Z^*e\mathbf{E} \quad (7.1)$$

Due to the electron shielding effect of the metal nucleus, the electrostatic force $\mathbf{F}_{\text{direct}}$ can be neglected. Thus the electron wind force \mathbf{F}_{wind} is the dominant driving force for electromigration³. The mass transport due to electromigration is in the direction of electron flow.

The experimental evidence presented in the study is limited for a clear identification of the growth mechanism. A fixed indenter tip also gives less control over the growth process. This study reports the growth of nickel nanostructure utilizing a mobile nanoindenter tip inside a scanning electron microscope. Nickel nanoparticles sitting on a nickel micropillar were used. Finite element modeling was employed for temperature distribution estimation on the system.

7.2 Methods

7.2.1. Fabrication of nickel micropillars and sample preparation

Nickel micropillars with 1 μm diameter and 1 μm in height were synthesized using photolithography and electroplating. A silicon substrate with 12 nm thermally grown SiO_2 thin film was used for the fabrication of nickel micropillars. Before the fabrication, surface cleaning

of the substrate was accomplished by solvent cleaning with water sonicating bath followed by a reactive ion etching (RIE) plasma clean. The substrate was cleaned in acetone, methanol and propanol for 5 min each, followed by 1min of DI water rinse and N₂ blow dry. RIE plasma clean was conducted in the PETS RIE machine. The substrate is first plasma cleaned in O₂ for 30 s and then in Ar for 30 s.

Figure 7.2 summarizes the fabrication process. Figure 7.2(a) shows the seed layer deposition step. A Lesker labline sputtering system was used for both titanium and nickel deposition. 70 nm of titanium and 220 nm of nickel seed layers were consecutively deposited onto the substrate in 5 mTorr of Ar atmosphere. After seed layer deposition the substrate was plasma cleaned again using the same parameters prior to photoresist deposition. Shown in Figure 7.2(b), a 1 μm thick positive photoresist layer is deposited onto the substrate. A repeating pattern is produced on the photoresist layer using photolithography with a A GCA 8500 i-line Stepper. As displayed in Figure 7.2 (c), a mask with the desired pattern is placed on top of the substrate and the substrate is exposed to UV light. Holes on the mask allows the penetration of UV light and the photoresist at the exposed area becomes soluble in developer solution. To remove the exposed photoresist layer and form the final pattern, the substrate is submerged in CD-26 developer solution for 60 seconds followed by immediate DI water rinse and N₂ blow dry. The resulting substrate configuration is exhibited in Figure 7.2(e). Figure 7.2(f) displays the electroplating of nickel onto the substrate. A layer with a nominal thickness of 0.958 μm was electroplated at 60 °C with a plating current of 6.6 mA. The plating solution used was Transene sulfamate nickel plating SN-10. The nickel that deposited on top the remaining photoresist will be stripped off the substrate together with the photoresist in the next step. The final micropillar substrate was obtained by subsequently removing the photoresist using the Futurrex RR41 resist

remover. Figure 7.3 (a) shows an SEM image of the obtained Ni micropillar forest. However, during fabrication some micropillars exhibit a “mushroom” top morphology due to the excess electroplating deposition, shown in Figure 7.3 (b) and (c).

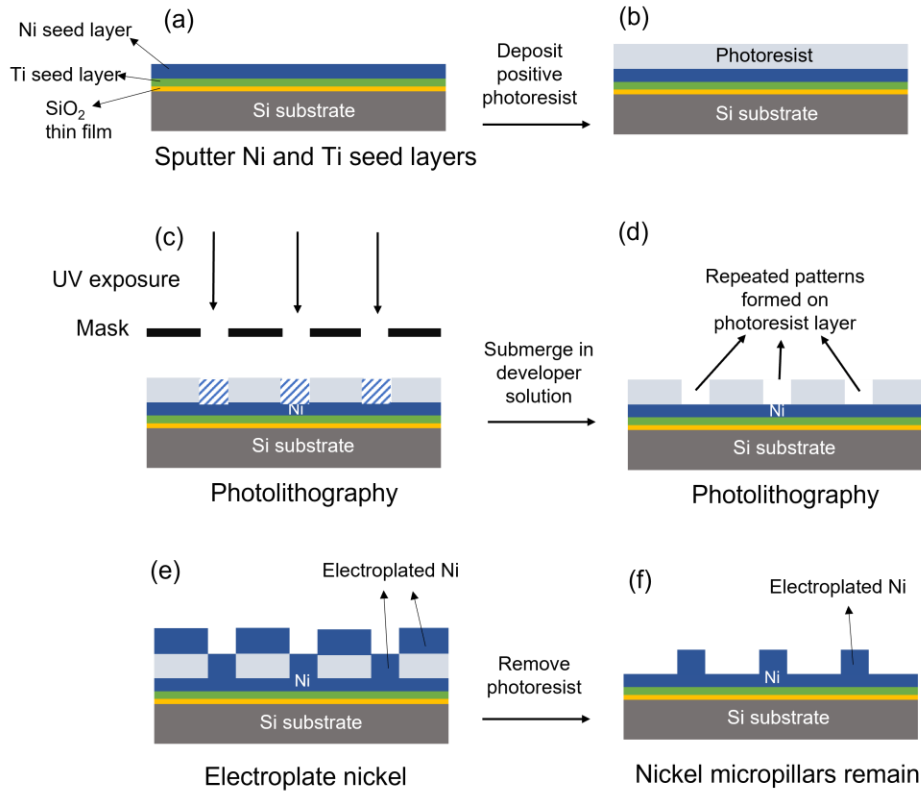


Figure 7.2 Nickel micropillar fabrication process using photolithography and electroplating.

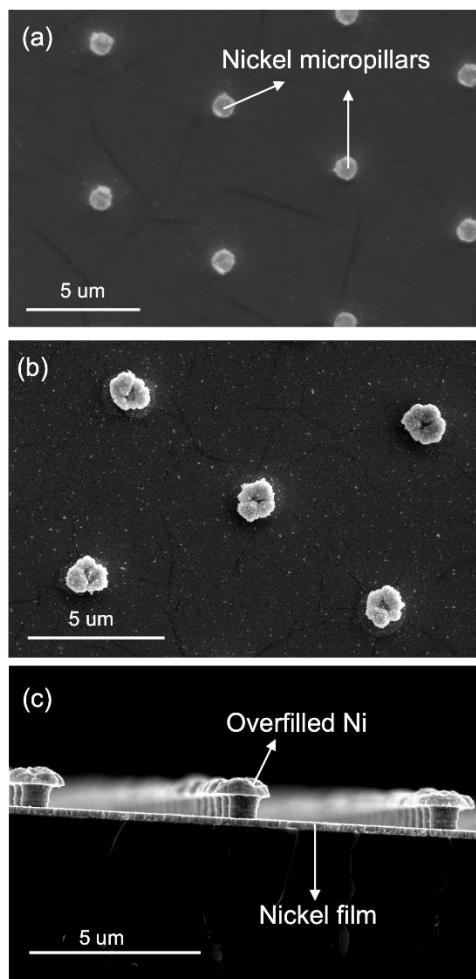


Figure 7.3 (a) Top view SEM image of the fabricated nickel micropillar arrays (b) Top view SEM image of nickel micropillars that exhibited wider top due to nickel overfill (c) Side view SEM image of the nickel micropillars with overfilled nickel.

Nickel nanoparticles with nominal diameter of 300 nm were sonicated in isopropanol for around 20 minutes and drop casted onto the micropillar substrate. Some nickel particles landed on top of the nickel micropillars and some landed on the nickel film. Configuration of nickel micropillars with nanoparticles on top were chosen for all experiments.

7.2.2. Current-activated growth of nickel nanostructures

Current-activated growth experiments were carried out with a ThermoFisher Quattro S environmental scanning electron microscope. No external heating was supplied during the experiments. Figure 7.4(a) shows a sketch of the experimental setup and Figure 7.4(b) shows the detailed construction of the sample. The substrate was fixed on an angled SEM sample stub with double sided copper tape, represented by the orange layer. Another piece of copper tape was used to create a conducting pathway between the nickel micropillars and the sample stage. A tungsten carbide cone shaped indenter tip (Micro Star Technologies, Huntsville, TX) is installed on an InSEM nanoindenter (KLA, Milpitas, CA), which is attached to the microscope. A Keithley model 6517B electrometer was used to apply a DC bias to the nanoindenter tip and measure the electric current in the circuit. Both the bias application and current measurement were controlled by a Python program. A positive DC bias was applied to the conducting tip of the nanoindenter and the sample stage was connected to ground. One directional movement of the nanoindenter along the indenter axis was achieved by the displacement and extension control provided by the manufacturer's InView software package. The growth process was recorded through a series of SEM micrographs and saved as a video file (images extracted from the video are included in Appendix).

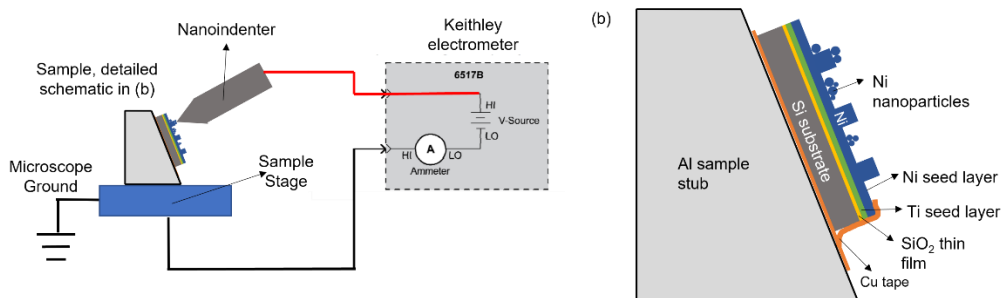


Figure 7.4 (a) Schematic of experimental setup. (b) Detailed construction of the nickel nanoparticle and micropillar sample

Contact between the nanoindenter and particle was made before any bias application or current measurement. I-V scans between -0.1 V and +10 V were first carried out to investigate electronic properties of the Ni particles and micropillar. Subsequently, a constant positive DC bias of 6-8 V was applied. A maximum current limit of 1 mA was set, i.e., that the applied bias was automatically shut off once the recorded electric current exceeded the set current limit. Mechanical drift of the indenter towards the sample was observed during the experiments. Effects of mechanical drift are discussed where appropriate for specific experimental data. Once a steady current was achieved, the indenter was manually retracted away from the sample stage using the displacement control in order to facilitate nanostructure growth.

7.3 Results:

7.3.1 SEM and electrical measurements:

Figure 7.5 (a) and (b) show one nickel micropillar and a number of Ni nanoparticles before and after indenter contact, respectively. The nickel micropillar displays rough edges on the top surface, indicated by the white arrows. Due to the limited step size of indenter tip and sample stage movement, precise contact is difficult to achieve. As a result, one nickel nanoparticle (labeled #1 in Figure 7.5) appears compressed by the indenter tip after contact.

The periodic intensity fluctuation in the vertical direction observed in Figure 7.5(b) caused by the instrumentation's interference with the scanning coil.

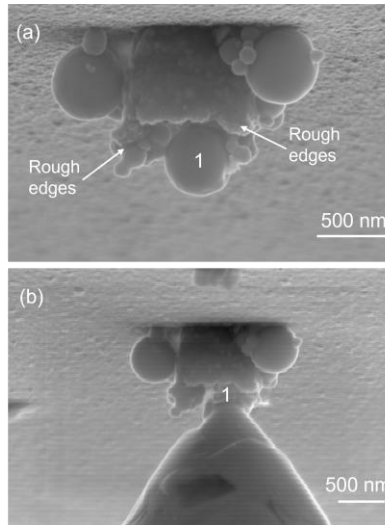


Figure 7.5 SEM images of the nickel nanoparticle and micropillar configuration (a) before and (b) after nanoindenter contact

Figure 7.6 (a) shows the recorded current versus applied bias from -0.1-10 V (I-V scan) of the particle and pillar before a constant bias is applied. The recorded I-V curve exhibits Ohmic behavior in the bias range between -0.1 V and +10 V. The resistance decreased slightly for each scan. A constant bias of +8 V was selected to carry out the current-activated growth experiment. A current safety limit of 1 mA was selected. Over the duration of 20 minutes after the bias was applied, the measured current continuously increased from 147 μA to 1.01 mA until the applied voltage was removed when the current exceeded the safety limit. Due to a software problem, no current values were recorded between 898 and 1192 s. The current recorded after 1193s exceeded the current safety limit of 1 mA. The bias was subsequently lowered to +7 V to reduce the current and continue the experiment Figure 7.6(c) shows a plot of the measured current versus time when a constant bias of +7 V was applied. The current steadily increased from 722 μA to 938 μA over 6 minutes. After 364 s a sharp increase from 0.938 mA to 11.6 mA within a time interval of 0.2 s which exceeded the set current safety limit and triggered the automatic shut

off of the applied bias. The applied bias was subsequently lowered to +6V, +5 V, +2 V and +0.5 V, while for each applied bias the current safety limit was instantaneously exceeded. For a bias of +0.1 V the recorded currents remained below 1 mA.

Several other experiments were conducted with similar nanoparticle and micropillar configurations. Figure 7.7 (a)-(c) displays the current values for different applied biases recorded either immediately before the software controlled current limit was triggered, or when a stable current below 1mA was registered. From all three experiments reproduced in Figure 7.7 a linear relationship between current and applied voltage was observed up to approximately 11mA which triggered the current safety limit.

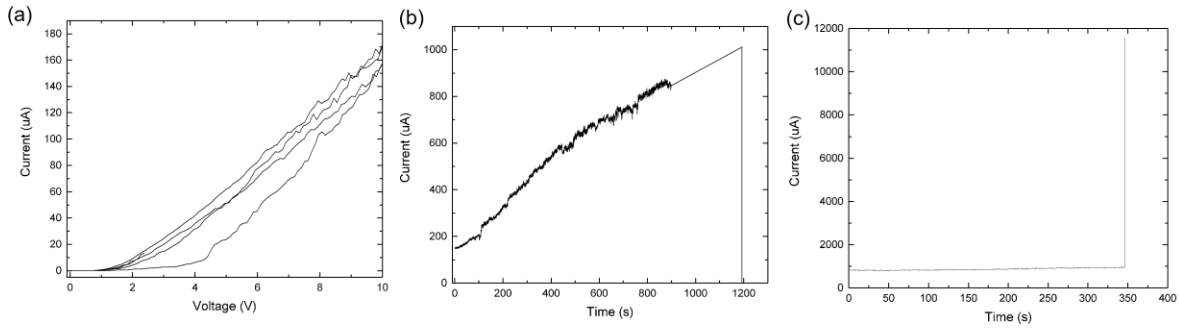


Figure 7.6 (a) Plot of measured current versus applied voltage before constant bias application (b) Plot of measured current versus time with a constant voltage of +8 V is applied (c) Plot of measured current versus time when a constant voltage of +7 V is applied.

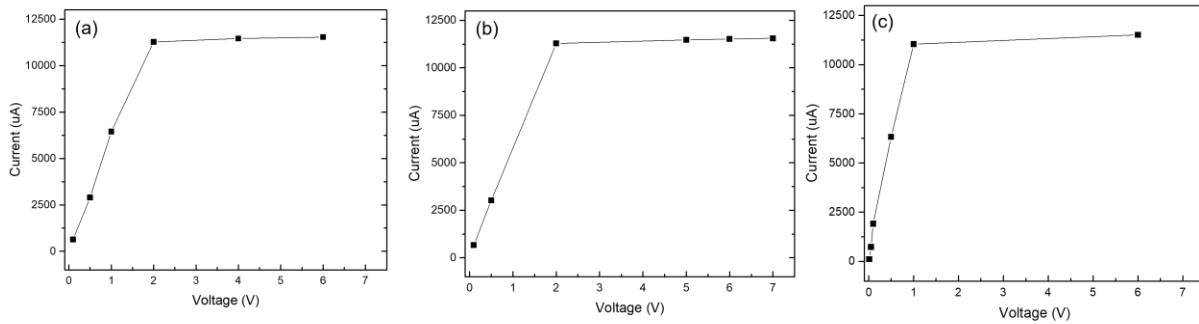


Figure 7.7 (a) Plot of instant measured current versus applied voltage after hard dielectric breakdown took place (b) (c) Similar results obtained from two additional experiments carried out with similar particle configurations.

Figure 7.8 shows the current versus time plot continuing from the experiment where a constant bias of +0.1 V is applied. Orange-colored regions labeled I-VI represent experiments with a continuous constant bias applied. No manual movement of the tip was attempted and no obvious tip drift is observed within the orange regions. The white blank regions in between are gaps where no bias is applied or with attempted experiments 1-6 marked by orange crosses where current exceeds limit right upon bias application. A current value of zero is assigned to these regions. The time periods indicated by the red arrows are current-decrease regions and green arrows represent current increase regions. The experiments conducted reveal different current behavior. In experiment I and III, the recorded current started between 650 – 850 μA and gradually decreased to zero. In experiment IV, the current started at around 800 μA but increased around 20 μA before gradually dropped down to zero. Experiment V and VI reveal a starting current of zero and then started gradually increase after some time. Recorded current for experiment V reached a maximum value of approximately 360 μA and dropped back to zero. For experiment VI on the other hand, recorded current exceeded the 1 mA current limit and bias was shut down.

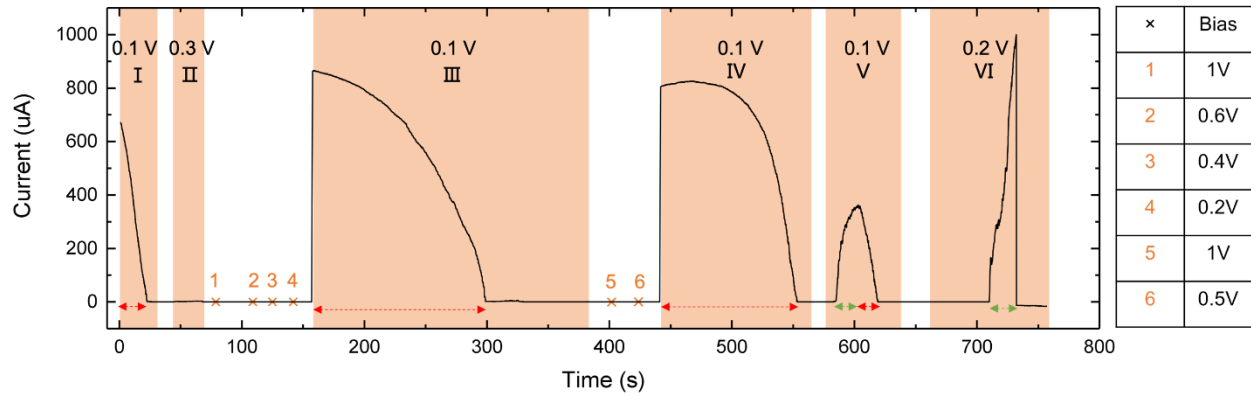


Figure 7.8 Plot of measured current versus time over a series of measurements. Each orange-colored region represents an individual experiment where a constant bias is applied, numbered I-IV. The corresponding constant bias is documented at the top of each region. White gap regions in between orange regions include times where no bias is applied or instant experiments where bias is applied but shuts off instantly upon application due to current overflow. Attempted experiments are marked out by orange crosses on the plot and the corresponding bias for each cross is listed in the table on the right.

Figure 7.9 shows the plot of measured current (black solid line) and relative position of the indenter (blue square) versus time when a constant positive bias of +0.1 V was applied after the final experiment shown in the sequence in Figure 7.8. During this experiment the indenter tip was manually retracted after 60 s to guide nanostructure growth. The indenter imaged exhibited steps on the edges due to the vertical image intensity fluctuation mentioned in the last section. As a result, the measured relative position of the indenter showed a stepped trend. Since the indenter retraction was controlled manually, the true movement speed was not strictly linear. The growth rate deduced is an approximation. Recorded currents fluctuated between 600 and 700 μA during indenter retraction. 60 -70 s of the experiment is referred to as stage I. During this stage, the indenter retracted at a very low speed where no obvious elongation or growth of nanostructure is observed. These data points are plotted as red and were not included in the calculation of growth rate. At the meantime, current gradually increased to around 760 μA . 70 to 93 s marks stage II of

the growth experiment. The indenter retraction speed increases and nanostructure growth was observed on the nickel particle along the indenter movement direction. Growth continued up until 93 s with a growth rate of 3.12 nm/s and resulted in 25 nm of elongation. Measured current during stage II maintained at a steady value of 760 μA with minimal fluctuation. Growth terminated at 93 s when the indenter tip and particle lost contact and current dropped to zero.

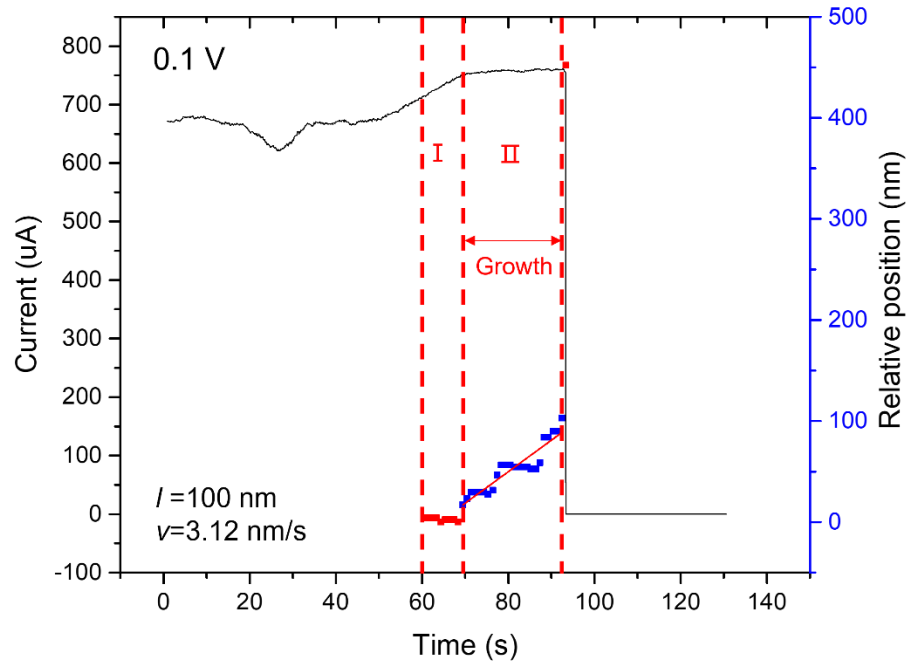


Figure 7.9 Plot of measured current (black solid line) and indenter tip relative position (blue and red squares) versus time when a constant bias of +0.1 V is applied. Red dashed line marks out the two stages of nanostructure growth. Blue squares are data points used for growth rate calculation and red squares are data points omitted for the calculation

Figure 7.10 (a) and (b) show the nickel nanoparticle and micropillar before and after nanostructure growth. The nickel particle 1 exhibited round morphology and had a diameter of 478 nm before the current-activated growth experiment. The particle agglomerate included two

smaller nickel nanoparticles that are highlighted by an arrow in Figure 7.10 (a). After the growth experiment, the morphology of particle 1 has changed to an elongated nanostructure with a blunt tip pointing towards the indenter tip. The dimension of particle 1 has increased to 600 nm in the direction parallel to the indenter axis. Arrows included in Figure 7.10 (b) highlight small, elongated metal structures (“spikes”) with relatively blunt tips. Figure 7.10 (c) exhibits a similar feature on the tip of the indenter head. The spikes align in the moving direction of the indenter tip indicated by the red dashed line in Figure 7.10(c).

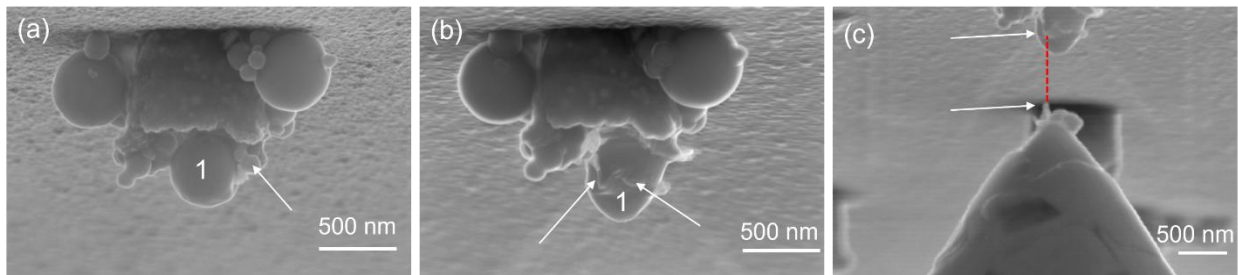


Figure 7.10 SEM images of the nickel nanoparticle and micropillar configuration (a) before nanoindenter contact and current activated growth experiment (b) after growth experiment. (c) Nanoindenter tip and nanostructure after growth experiment

7.3.2 Finite element modeling

Direct measurement of the particle agglomerate temperature during the in-situ SEM experiments was not feasible. Instead, finite element modeling using the COMSOL Multiphysics program packet was employed to estimate the local temperature distribution during the nanostructure growth process. The simplified three-dimensional model displayed in Figure 7.11 (a) and (c) was used to approximate the more complex experimental geometry. For finite element calculations the model was considered an immobile solid with no external current or heat source. A bias of +0.1 V is applied to the end surface of the indenter. The bottom surface of the nickel film was set to ground potential. The AC/DC and the heat transfer modules of the COMSOL

software package were used to calculate temperature distributions that arise from Joule heating while heat dissipation was considered to occur by conduction and radiation.

Equation (7.2) describes the relationship between the electric current density J and the applied bias V :

$$\mathbf{J} = \sigma \mathbf{E} = -\sigma \nabla V \quad (7.2)$$

s is the electrical conductivity and E is the electric field. Heat transfer in solids is described by equations (7.3) through (7.6).

$$\rho C_p \left(\frac{\partial T}{\partial t} \right) + \nabla \cdot (\mathbf{q} + \mathbf{q}_r) = Q \quad (7.3)$$

$$\mathbf{q} = -k \nabla T \quad (7.4)$$

$$Q = q_e = \mathbf{j} \cdot \mathbf{E} \quad (7.5)$$

$$-\mathbf{n} \cdot \mathbf{q}_r = \varepsilon \sigma_{SB} (T_{amb}^4 - T^4) \quad (7.6)$$

ρ is the physical density of the material, C_p is the specific heat capacity, q is the heat flux by conduction; q_r is the heat flux by radiation, Q is an external heat source resulting from Joule heating, ε is the surface emissivity, σ_{SB} is the the Stefan-Boltzmann constant, and T_{amb} is the ambient temperature.

Figure 7.11(b) shows the results of the finite element model calculation with the condition that the far end of the indenter and the side surfaces of the Ni film (cf. Figure 7.3(b)) remain at room temperature due to the fact that the sample stage and indenter have large thermal mass and serve as heat sinks. Under this condition the model predicts the temperature of the

growing nanostructure to be around 450 K. Figure 7.11 (d) displays the temperature distribution without such conditions, resulting in a temperature of roughly 1100 K for the growing nanostructure.

The 3D model utilized for finite element modeling is not a precise reproduction of the rather complex experimental setup inside the SEM instrument. Only the indenter, particle, micropillar and part of the nickel film were simulated. The ohmic resistance of the experimental setup including instrument electronics but without the particle agglomerate and the micropillar was determined to be roughly 27Ω by directly contacting the conducting indenter to the nickel seed layer (cf. Figure 7.2(a)). The total ohmic resistance during the growth process was determined to be around $137 - 161 \Omega$.

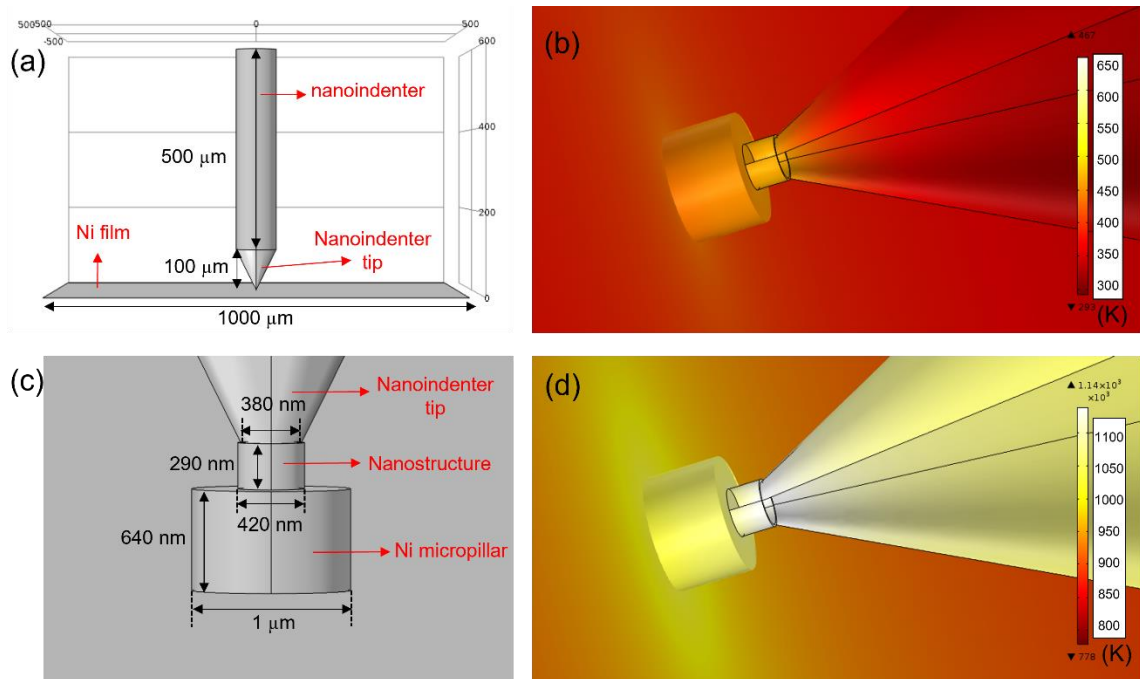


Figure 7.11 (a) Simplified 3D model used in finite element modeling (c) Higher magnification view of the 3D model that includes the indenter tip, nanostructure and micropillar. (b) Temperature distribution of nanostructure and micropillar with room temperature BC. (d) Temperature distribution of the nanostructure and micropillar without any BC

7.4 Discussion

The experimental results reported in the preceding section demonstrate the feasibility of tip-guided growth of metal nanostructures by the application of a bias that induces current flow and Joule heating. A prerequisite for current flow through the particle agglomerate is the formation of electrically conducting pathways.

7.4.1. Dielectric breakdown of nickel oxide layer

After exposure to air a semiconducting thin native oxide layer is usually present on the surface of nickel nanoparticles and prevents electric current flow at room temperature⁴⁻⁷. In the presence of an electric field, dielectric breakdown of the oxide layer can occur and was previously observed by in-situ transmission electron microscopy in combination with electrical measurements^{5, 8, 9}. Figure 7.6 (a) shows the I-V curve for the particle-micropillar configuration after indenter contact. The acquired I-V scans exhibit Schottky contact characteristics at lower voltage regions, which is a reflection of the semiconducting property of the nickel oxide film^{10, 11}. The measured current value increases slightly for each round of I-V curve acquisition. Similarly, gradual current increase is also observed when a constant bias of +8 V is applied after the I-V scan shown in Figure 7.6 (b). This behavior indicates soft dielectric breakdown of the oxide film and reproduces earlier results reported in the literature^{5, 8, 9}. Soft breakdown describes the electric field-induced formation of defects, i.e., oxygen vacancies in the case of nickel oxide, that give rise to high resistivity conductive pathways through the formerly insulating oxide film⁵. Once the gradually increasing current reached the imposed current limit the bias was reduced to +7 V. The subsequent continuous gradual current increase displayed in Figure 7.6(c) suggests additional soft breakdown event that eventually lead to percolation of oxygen vacancies and the

formation of hard breakdown, i.e. the rapid current increase observed after 350 s caused by the formation of highly conducting pathways across the nickel oxide film⁵.

Figures 7.7 (a)-(c) reflect the electrical properties of the nanoparticle/micropillar configuration after hard dielectric breakdown enabled by the removal of interfacial nickel oxide^{5, 8}. Currents displayed in Figure 7.7 were obtained at the onset of bias application instead of after prolonged application of constant bias. It is therefore concluded that temperature effects due to Joule heating are negligible. The linear regions of the I-V plots in Figure 7.7 suggest Ohmic contacts with a total resistance ranging between 80 - 180 Ω .

7.4.2. Sintering of particle agglomerates

Once permanent conductive pathways are established within the particle agglomerate, i.e., hard dielectric breakdown of the oxide passivation layers, Figure 7.8 displays different variations of electric currents during constant bias experiments. For experiment I that was conducted with a bias of 0.1V the current drops from initially around 670 μA to near zero after 33 s. Reapplication of a slightly higher bias of +0.3 V (experiment II) did not result in an obvious increase in current above 1-3 μA . This observation indicates that the indenter tip partially disconnected from the particle agglomerate during experiment I. While the indenter was not intentionally moved during intervals I and II it is likely that Joule heating during experiment I has caused some sintering of the particle agglomerate leading to partial disconnection from the indenter tip. However, subsequent application of biases at times labeled '1' through '4' in Figure 7.8 resulted in instantaneous increases in current above the imposed 1 mA safety limit. Similar sudden current increases were observed at times labeled '5' and '6' in between experiments III and IV. Manual re-engagement was sometimes attempted. Throughout all experiments a small

spatial drift of the indenter tip towards the sample stage of the ESEM was observed. It is therefore concluded that for intervals where manual re-engagement was not attempted, the small but continuous forward drifting of the indenter has led to electrical re-connection with the particle agglomerate during time intervals when no bias is applied and the absence of current does not cause any additional shrinkage of the agglomerate in the direction of the indenter axis. This conclusion also explains the sudden current increase at the onset of experiments III and IV. The gradual decline of experimentally observed currents during experiments III and IV reflects geometric changes of the shrinking particle agglomerate during current exposure, i.e., Joule heating. The continuous shrinkage of the agglomerate eventually led to repeating detachment from the indenter tip once the rate of shrinkage is larger than the rate of mechanical forward drifting of the indenter. Detachment of the particle agglomerate from the indenter tip was not directly observed during in-situ SEM imaging because the contact area was blocked from the electron beam due to the indenter geometry.

Experiment V and VI exhibit a different behavior. Electric current through particle agglomerate gradually increased up to around 400 μA during the application of +0.1 V. Upon further increase of the bias to +0.2 V the observed current increased above 1 mA. The gradual increase in current indicates electrical contact between the agglomerate and the indenter, while both unintentional forward drifting of the indenter and local Joule heating at the contact area causing neck growth and contribute to the current increase. Subsequent decreases in current are once again caused by sintering of the agglomerate.

7.4.2. Tip guided growth mechanism of nickel nanostructure

Experiments I through VI discussed above have demonstrated mass flow within the particle agglomerate. Once mass flow is activated Figures 7.10(b) and (c) show experimental evidence for the tip-guided growth of nanostructures with high aspect ratios. The relatively stable current around 650 -700 μA displayed in Figure 7.9 prior to intentional tip movement indicates a stable electrical contact between the indenter tip and the particle agglomerate. During initial retraction of the indenter during stage 1, indenter movement is very minor due to low retraction speed and no obvious nanostructure growth occurred. Relative positions measured in this stage are excluded from the growth speed calculation. During this stage, the observed current increased steadily.

Once the retraction rate of the indenter was increased (stage II in Figure 7.9) nanostructure growth is observed in the moving direction of indenter. During tip-induced nanostructure growth the current recorded during the experiment remains almost constant. Consistent with the study by Rufner et al.¹ a decreasing current was expected during nanostructure growth. However, the gradually increasing current during stage 1 due to sintering has likely compensated for the increased resistance due to directional growth in stage 2.

The growth rate observed in stage 2 is roughly 3.1 nm/s, which is approximately 5x smaller than that previously by Rufner and co-workers¹. However, the growing nanostructure in the previous study was constrained between a non-moving tip and a relatively flexible amorphous carbon film supporting a nickel nanoparticle agglomerate. In this study the growing nanostructure is constrained between a rigid substrate and the slowly receding indenter tip. Potential mechanisms for nanostructure growth, as previously discussed by Rufner and co-workers¹ include surface and volume diffusion in the presence of Joule heating, Ludwig-Soret

diffusion in a temperature gradient¹², and electromigration². The electron wind force determines that the mass transport direction is the same as electron flow direction, which coincides with the observation of this study. Indenter retraction then provided space needed for mass transport. The two factors together enabled the growth in the tip movement direction. The observation of small metal filaments with relatively high aspect ratios in Figures 7.10(b) and (c) indicate electro plasticity¹³⁻¹⁵ where enhanced plasticity is observed with the existence of an electric current. Based on this information, current densities at the contact area between the indenter tip and the particle agglomerate are estimated to be as high as 10^{10} A/m². Such current densities were previously reported to be sufficient to cause electro plasticity effects under the influence of electron wind force¹³⁻¹⁵.

Finite element modeling was used to assess the local temperature at the indenter/particle agglomerate contact area to derive suitable mass transport mechanisms. The true temperature of the nanostructure should fall in between 450 K (with boundary condition) and 1100 K (without boundary condition).

Nickel self-diffusion coefficient can be calculated from the growth rate and elongation. Diffusion flux of nickel can be expressed by the growth rate and density of nickel in the following equation:

$$J = \frac{m}{A \cdot t} = \frac{\rho \Delta V}{A \cdot t} = \frac{\rho A l}{A t} = v \cdot \rho \quad (7.7)$$

J is the flux of nickel, m is material mass, ρ is density of nickel, A is the cross-sectional area, t is diffusion time, l is the length of nickel nanostructure and v is growth rate. According to Fick's first law, flux can also be expressed as:

$$J = -D \frac{\partial C}{\partial x} = D \frac{\rho}{l} \quad (7.8)$$

D is the diffusion coefficient and $(\partial C/\partial x)$ is the concentration gradient. With an elongation $l=100$ nm, the diffusion coefficient calculated from flux equals 3.1×10^{-6} m²/s. Assuming nickel self-diffusion through the lattice, temperature deduced from literature^{16, 17} lands in the range of 1250 -1300 K. If assuming nickel surface diffusion, the deduced temperature then falls between 650 and 724 K. It is likely that various diffusion mechanisms are taking place simultaneously while one or few dominates. Therefore, the real temperature should land in between the 650 – 1300 K. This is consistent with the finite modeling results, suggesting that Joule heating is indeed responsible for the temperature increase and provided energy to active diffusion that leads to nanostructure growth.

7.5. Conclusion

The experimental results in this study report the tip-guided growth of nickel nanostructures due to electric current flow that results from an applied electric bias. While previous results by Rufner et al have demonstrated growth of nanostructures at the tip of an immobile scanning tunneling microscopy tip, this study has demonstrated directional nanostructure growth between a rigid substrate and a moving nanoindenter tip. Nickel nanostructure growth is accomplished by a combination of electro plasticity and Joule heating. Mass transport is facilitated by nickel self-diffusion. Joule heating provides the thermal energy needed to activated growth. Finite element modeling was used to verify that the nanostructure temperature during growth was in the range of 450- 1100 K due to Joule heating, which is the

temperature expected for nickel self-diffusion. Nanostructure growth direction is determined by the current and grows in the electron flow direction.

Acknowledgements:

The authors acknowledge funding from the National Science Foundation under award DMR-1836571. The ESEM instrument was acquired with NSF-MRI award DMR-1725618. The authors are grateful for the assistance of Dr. Yusha Bey in fabricating the nickel micropillars.

7.6 References:

1. Rufner JF, Bonifacio CS, Holland TB, Mukherjee AK, Castro RHR, Benthem K van. Local Current-Activated Growth of Individual Nanostructures with High Aspect Ratios. *Materials Research Letters*. 2014;2(1):10–15. <https://doi.org/10.1080/21663831.2013.855272>
2. Ho PS, Kwok T. Electromigration in metals. *Rep Prog Phys*. 1989;52(3):301–348. <https://doi.org/10.1088/0034-4885/52/3/002>
3. Lienig J, Thiele M. Fundamentals of Electromigration. *Fundamentals of Electromigration-Aware Integrated Circuit Design*. Cham: Springer International Publishing; 2018:13–60. https://doi.org/10.1007/978-3-319-73558-0_2
4. Qu B, van Benthem K. In situ anisotropic NiO nanostructure growth at high temperature and under water vapor. *Journal of the American Ceramic Society*. 2022;105(4):2454–2464. <https://doi.org/10.1111/jace.18260>
5. Bonifacio C, Holland T, van Benthem K. Time-dependent dielectric breakdown of surface oxides during electric-field-assisted sintering. *Acta Materialia*. 2014;63:140–149. <https://doi.org/10.1016/j.actamat.2013.10.018>
6. Railsback JG, Johnston-Peck AC, Wang J, Tracy JB. Size-Dependent Nanoscale Kirkendall Effect During the Oxidation of Nickel Nanoparticles. *ACS Nano*. 2010;4(4):1913–1920. <https://doi.org/10.1021/nn901736y>
7. Koga K, Hirasawa M. Anisotropic growth of NiO nanorods from Ni nanoparticles by rapid thermal oxidation. *Nanotechnology*. 2013;24(37):375602. <https://doi.org/10.1088/0957-4484/24/37/375602>

8. Holland TB, Thron AM, Bonifacio CS, Mukherjee AK, van Benthem K. Field assisted sintering of nickel nanoparticles during in situ transmission electron microscopy. *Appl Phys Lett*. 2010;96(24):243106. <https://doi.org/10.1063/1.3452327>
9. Bonifacio CS, Holland TB, van Benthem K. Evidence of surface cleaning during electric field assisted sintering. *Scripta Materialia*. 2013;69(11):769–772. <https://doi.org/10.1016/j.scriptamat.2013.08.018>
10. Nachman M, Cojocaru LN, Ribco LV. Electrical Properties of Non-Stoichiometric Nickel Oxide. *physica status solidi (b)*. 1965;8(3):773–783. <https://doi.org/10.1002/pssb.19650080316>
11. Zhao Y, Wang H, Wu C, *et al.* Structures, electrical and optical properties of nickel oxide films by radio frequency magnetron sputtering. *Vacuum*. 2014;103:14–16. <https://doi.org/10.1016/j.vacuum.2013.11.009>
12. Groot SRD, Mazur P. Non-Equilibrium Thermodynamics. Courier Corporation; 2013
13. Sprecher AF, Mannan SL, Conrad H. Overview no. 49: On the mechanisms for the electroplastic effect in metals. *Acta Metallurgica*. 1986;34(7):1145–1162. [https://doi.org/10.1016/0001-6160\(86\)90001-5](https://doi.org/10.1016/0001-6160(86)90001-5)
14. Conrad H. Electroplasticity in metals and ceramics. *Materials Science and Engineering: A*. 2000;287(2):276–287. [https://doi.org/10.1016/S0921-5093\(00\)00786-3](https://doi.org/10.1016/S0921-5093(00)00786-3)
15. Kim M-J, Yoon S, Park S, *et al.* Elucidating the origin of electroplasticity in metallic materials. *Applied Materials Today*. 2020;21:100874. <https://doi.org/10.1016/j.apmt.2020.100874>
16. Maier K, Mehrer H, Lessmann E, Schüle W. Self-diffusion in nickel at low temperatures. *physica status solidi (b)*. 1976;78(2):689–698. <https://doi.org/10.1002/pssb.2220780230>
17. Bakker H. A Curvature in the $\ln D$ versus $1/T$ Plot for Self-Diffusion in Nickel at Temperatures from 980 to 1400 C. *A Curvature in the $\ln D$ versus $1/T$ Plot for Self-Diffusion in Nickel at Temperatures from 980 to 1400 C*. De Gruyter; 2022:569–576. <https://doi.org/10.1515/9783112496244-013>

Chapter 8: Conclusions and future work

The conclusions section in this chapter provides short summaries of the results from each individual research study from Chapter 3 to 7 and an overarching conclusion for the dissertation. Potential future research directions that could extend the scope of the study are outlined in the future work section.

8.1 Conclusions

8.1.1 Stabilization of FeO wüstite phase at the nanoscale

Navrotsky and co-workers have predicted that the wüstite phase of iron oxide (FeO) is thermodynamically unstable with particle sizes below 100 nm¹. In-situ heating of individual γ -Fe₂O₃ nanoparticles of average diameter of 46 nm and 1D nanochains of interconnected particles with a similar size were conducted. EELS results revealed that for individual γ -Fe₂O₃ particles, γ -Fe₂O₃ transitioned to Fe₃O₄ at 250 °C and maintained Fe₃O₄ up to 700 °C. Afterwards, the transition to Fe took place at around 800 °C. No FeO phase was detected. For γ -Fe₂O₃ nanochains with lengths less than the critical value of 180 nm, a similar phase transition trajectory was observed. However, for γ -Fe₂O₃ nanochains above critical length, FeO phase was detected during the reduction process. The SAED pattern further confirmed the existence of FeO phase at 800 °C for longer nanochains, instead of the direct transition from Fe₃O₄ to Fe. It is concluded that the surface to volume ratio decreases when assembling the nanoparticles into 1D nanochains, while the greater surface energy in isolated nanoparticles hinders the phase transformation to FeO. The study has confirmed the instability of FeO at the nanoscale for single particles but at the same time proved that its phase stability can be achieved by arranging

particles in nanochains with a critical length of 180 nm. This finding provides a possible solution for stabilizing FeO at the nanoscale for future reliable applications.

8.1.2 Anisotropic growth of NiO nanostructures at high temperatures

Anisotropic growth of NiO nanostructures from nickel nanoparticles were observed during ESEM heating at 800 °C in water vapor atmospheres. Two growth modes were documented including particle elongation and high aspect ratio growth. Nanostructure growth takes place at specific areas on the particle surface instead of evenly distributed. For the nickel nanoparticles, lower surface energy configuration can be achieved by annealing the particles prior to ESEM heating at lower oxygen partial pressures and no nanostructure growth was observed during ESEM heating afterwards. Therefore, it is concluded that nickel oxide nanostructures only grow at specific locations where local surface energy densities are high enough and can be further lowered by the growth. Manipulation of surface energy prior to heating in water can be a new way of circumventing oxide nanostructure growth in water-containing atmospheres.

Similar anisotropic nickel oxide nanorod growth from nickel nanoparticles was observed at 650 °C at 4×10^{-4} Pa of oxygen partial pressure. HRTEM shows that layer by layer NiO growth takes place at the Ni/NiO interface by ledge movement accompanied by the consumption of the nickel particle. Oxidation reaction takes place at the Ni/NiO interface. This growth process resembles the terrace-ledge-kink mechanism^{2, 3}. The study has demonstrated that the TLK crystal growth mode is applicable at a buried solid reaction flat interface. The diffusion coefficient derived from the material flux needed for growth coincides with the effective diffusion coefficient of oxygen in NiO, indicating that the growth is facilitated by oxygen vacancy diffusion along the interface.

8.1.3 Electric field effect on defect redistribution along SrTiO₃ grain boundaries

External electric field was applied to SrTiO₃ diffusion bonded bicrystal with a (100) twist grain boundary during high temperature annealing. The applied electric fields were parallel to the grain boundary plane. A larger grain boundary expansion was observed near the positive electrode side than the negative electrode side. Both EELS and XPS results showed higher oxygen vacancy concentration near the negative electrode side. Higher electric field strength can cause decomposition of the grain boundary structure near the negative electrode side. It is concluded that electric fields can change the grain boundary structure by driving the oxygen vacancies towards the negative electrode side and cause defect redistribution along the boundary. Therefore, application of an external electric field during annealing may be a feasible route in grain boundary engineering. Desired grain boundary structure can then be obtained by altering the electric field direction or strength.

8.1.4 Tip-guided growth of nickel nanostructures with the application of electric current

Tip-guided one-directional growth of nickel nanostructures was observed with electric current flow due to application of a DC bias and upon retraction of the indenter tip. Dielectric breakdown of the nickel oxide surface layer was observed prior to structure growth. Sintering of the particle caused particle shrinkage that lead to intermittent loss of contact reflected by the measured current. Contact between the nanoparticle and tip was maintained during growth and growth is the direction of electron flow. It is concluded that mass transport during growth is facilitated by nickel self-diffusion and Joule heating provides the thermal energy needed for growth activation. The mass transport direction is determined by the electric current flow direction.

This dissertation has reported in detail how different parameters influences the redox behaviors of the example metal and ceramic materials on the nanoscale. The underlying mechanisms discussed provide valuable information on achieving controlled growth of metal and ceramic multi-dimensional nanostructures.

8.2 Future Work

8.2.1 Controlled anisotropic nickel oxide growth

Anisotropic nickel oxide growth from nickel nanoparticles was observed at 800 °C in water vapor atmospheres. The obtained oxide nanostructure exhibited various morphologies and dimensions. It is concluded that growth takes place at locations on particle surfaces that possess sufficiently high local surface energy densities. Controlled anisotropic growth of the nickel oxide with desired diameter and growth mode may be realized by selecting particles with a specific surface orientation and area. Then systematic heating experiments of nickel particles with different sizes and facet orientation need to be conducted to identify the preferred surface orientation for growth. Growth temperature and water vapor pressure can also be adjusted at the same time to achieve optimized growth.

8.2.2 In-situ controlled tip-guided growth of nickel nanostructures

In this study, nickel nanostructure growth was achieved when retracting the indenter tip with current flow. However, the growth process was initiated after many attempts and terminated shortly due to loss of contact between the tip and nanostructure. A number of optimizations can be considered for more controlled structure growth in future experiments.

Firstly, indenter retraction in the study was fully manual, which posed a challenge on retaining consistent retraction speed. A large indenter step movement was documented upon

growth termination. The loss of contact was likely caused by the indenter retraction speed exceeding the nanostructure growth speed. Automating indenter movement at a constant speed could potentially achieve continuous growth as long as contact is maintained. Secondly, improving indenter stability could help reduce mechanical drift, which would lead to more stable contact as well as more controlled growth. Additionally, mass transport caused by electromigration requires a high enough current density. Hence, reducing contact area such as utilizing a sharper indenter tip may lead to growth with a smaller overall current. Lastly, the nickel particles used in the study were exposed to air prior to experiment and a passive nickel oxide layer was present on the particle surface. One result demonstrated in this dissertation is that dielectric breakdown of the nickel oxide layer needed to be achieved for growth to take place. Therefore, more efficient surface cleaning of the nickel particle surface prior to growth experiment such as particle annealing in a reducing atmosphere should be considered. This may help avoid additional bias application processes to achieve dielectric breakdown of the surface oxide layers, which greatly shortens the time needed to initiate growth.

Theoretical calculation as well as finite element modeling were utilized to analyze the growth mechanism. However, utilizing a transmission electron microscope to further characterize the obtained nanostructure will allow the ability to gain more information on the nanostructure crystallography and atomic structure development during growth. Previous study conducted by Rufner and co-workers⁴ was carried out inside a TEM, however further characterization of the nanostructure was not accomplished due to the agglomerate. This study was able to successfully retain the grown nanostructure. Focused ion beam can be employed to prepare the sample for further characterization in the TEM.

To further extend the study, multi-directional movement of the indenter tip can be employed to potentially achieve 3D nanostructure growth.

8.2.3 In-situ electric field application during annealing of SrTiO₃ bicrystals

This study has clearly demonstrated that the application of an external electric field during SrTiO₃ annealing lead to oxygen vacancy redistribution along the grain boundary. However, the grain boundary characterizations were carried out ex-situ after annealing and electric field application was completed. For the bicrystal annealed with higher field strength near the negative electrode side, grain boundary decomposition was observed. It was proposed that oxygen backfilling took place from the XPS observation that Ti³⁺ and Ti²⁺ intensities have decreased compared to the lower field strength. In-situ annealing experiment with electric field application in STEM will be able to provide real-time development of the grain boundary structure, which could help further confirm the oxygen vacancy redistribution as well as the abnormality observed at higher field strength near the negative electrode side.

8.3 References

1. Navrotsky A, Ma C, Lilova K, Birkner N. Nanophase transition metal oxides show large thermodynamically driven shifts in oxidation-reduction equilibria. *Science*. 2010;330(6001):199–201. <https://doi.org/10.1126/science.1195875>
2. Kossel W. Extending the Law of Bravais. *Nachr Ges Wiss Göttingen*. 1927;143.
3. Stranski IN. Zur Theorie des Kristallwachstums. *Z Phys Chem*. 1928;136:259–278.
4. Rufner JF, Bonifacio CS, Holland TB, Mukherjee AK, Castro RHR, Benthem K van. Local Current-Activated Growth of Individual Nanostructures with High Aspect Ratios. *Mater Res Lett*. 2014;2(1):10–15. <https://doi.org/10.1080/21663831.2013.855272>

Appendix: Supplemental materials

Chapter 3 Stabilization of metal(II)oxides on the nanoscale:

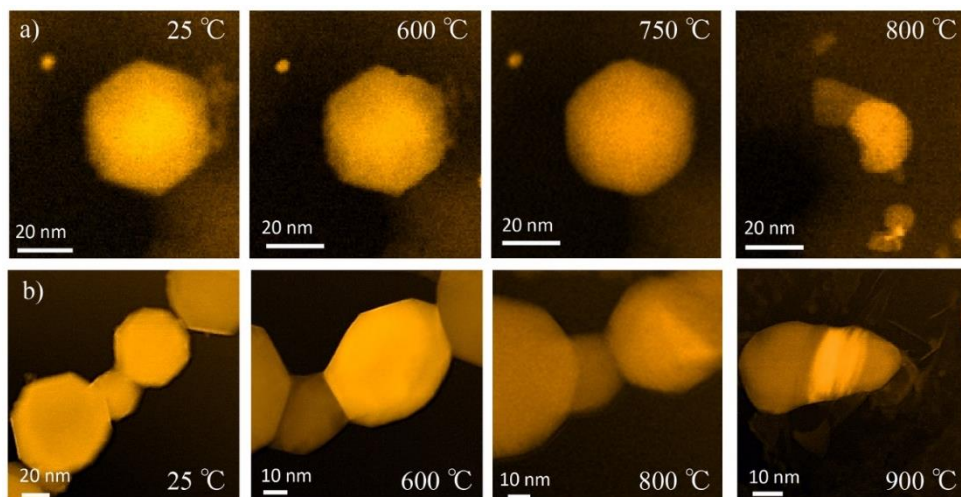


Figure S1. In-situ heating. (a) and (b) show series of annular dark field STEM images that were recorded during in situ annealing of (a) isolated iron oxide nanoparticles from 25°C to 800°C, and (b) nanochains from 25°C to 900°C. The amorphous carbon film supporting the individual nanoparticles appears as diffuse contrast in (a). The micrographs in a) and b) origin from two specific sample areas, respectively, but reveal morphological changes representative for 30 different areas across 6 different TEM samples.

Chapter 4 In situ anisotropic NiO nanostructure growth at high temperature and under water vapor:

- Video of ESEM heating of the growing nanostructures recorded at 400 Pa of water vapor

Chapter 5 In-situ anisotropic growth of nickel oxide nanostructures through layer-by-layer metal oxidation:

- Video recorded during nanostructure growth process

Chapter 7 Tip Guided Growth of Nickel Nanostructure with the Application of Electric Current:

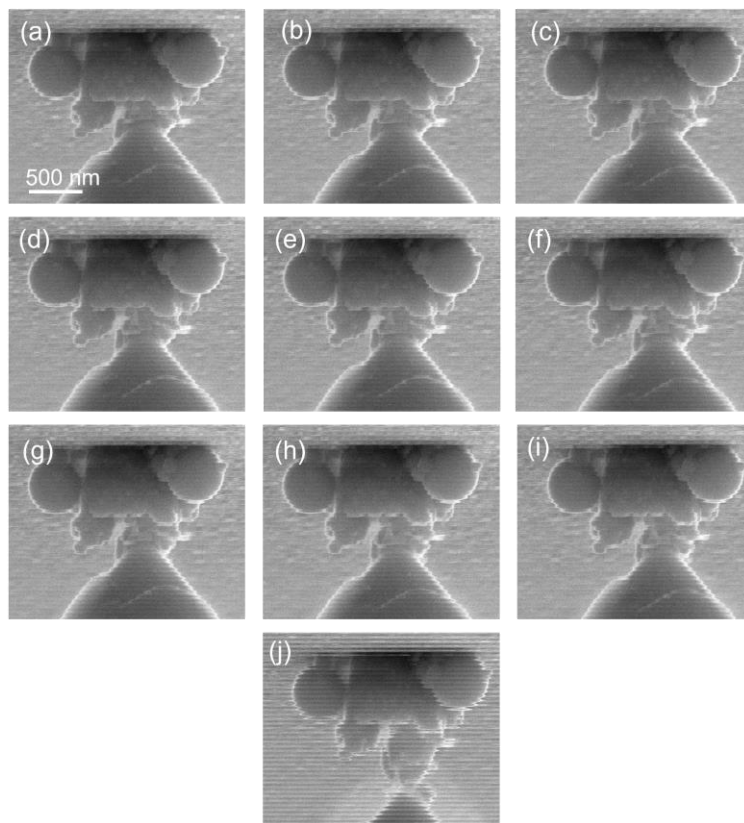


Figure S2. SEM micrographs extracted from the video recorded of nanostructure growth process with an applied bias of +0.1 V. Micrographs were extracted every 3 seconds until growth terminated.